APPLICATION OF ORBITAL SENSORS TO DETECT DEFORESTATION IN THE AMAZON RAINFOREST

CLÁUDIA ARANTES SILVA

TESE DE DOUTORADO N° 67

Advisor: Ph.D. Edson Eyji Sano – Embrapa Cerrados

Co-advisor: Ph.D. Fabio Del Frate – Tor Vergata University of Roma

Brasília – DF, 2021

APLICAÇÃO DE DADOS ORBAIS MULTI-SENSORES PARA IDENTIFICAÇÃO DO DESMATAMENTO NA FLORESTA AMAZÔNICA

Cláudia Arantes Silva

Tese de Doutorado apresentada ao Programa de Pós-Graduação em Geociências Aplicadas e Geodinâmica, na área de concentração Geoprocessamento e Análise Ambiental, do Instituto de Geociências da Universidade de Brasília (UnB), para obtenção do Título de Doutora.

Brasília – DF, 2021

UNIVERSIDADE DE BRASÍLIA – INSTITUTO DE GEOCIÊNCIAS

APPLICATION OF ORBITAL SENSORS TO DETECT DEFORESTATION IN THE AMAZON RAINFOREST

Cláudia Arantes Silva

Tese de Doutorado

Thesis Committee

_____

Ph.D. Edson Eyji Sano

Embrapa Cerrados - Brazil – Advisor

_____

Ph.D. Giovanni Laneve

Scuola di Ingegneria Aerospaziale, Sapienza University of Rome – Italy

_____

Ph.D. Hélcio Vieira Júnior

Centro Gestor e Operacional do Sistema de Proteção da Amazônia (Censipam) – Brazil

_____

Ph.D. Suzan Waleska Pequeno Rodrigues

Instituto de Geociências – Universidade de Brasília – Brazil

Brasília – DF, 2021

Somente a existência que transcende a si mesma, somente a vida humana que ultrapassa seus limites na direção do mundo é capaz de se realizar. Do contrário, ao visar diretamente a autorrealização, fracassa.

Viktor Frankl

Dedication

To God,

To my family,

To Paula and Pedro,

To Carlos.

ACKNOWLEDGEMENTS

APLICAÇÃO DE DADOS ORBITAIS MULTI-SENSORES PARA IDENTIFICAÇÃO DO DESMATAMENTO NA FLORESTA AMAZÔNICA

Autora: Cláudia Arantes Silva

Orientador: Ph.D. Edson Eyji Sano – Embrapa Cerrados

Co-orientador: Ph.D. Fabio Del Frate – Tor Vergata University of Roma

RESUMO

O avanço do agronegócio em terras amazônicas tem sido caracterizado por um ciclo preocupante de desmatamento, queimadas, exploração da terra e abertura de novas vias de escoamento que se retroalimenta. Em grande medida, essa exploração se dá de forma desordenada e em níveis superiores ao que preconiza a lei. Após 2012, com a aprovação do novo Código Florestal Brasileiro, verificou-se uma reversão na tendência de queda dos indices de desmatamento. A perda de floresta e a emissão dos gases de efeito estufa (GEE) voltaram a ser motivo de grande preocupação mundial. Em 2015, no Acordo de Paris, o Brasil se comprometeu em reduzir emissões de GEE. Considerando que uma parte significativa dessas emissões tem origem em queimadas na floresta, o monitoramento da mesma se torna especialmente importante. Parte considerável da ocupação da floresta ocorre dentro do arco do desmatamento, região em forma de arco que está localizada no extremo sul da Amazônia Brasileira. Historicamente, o acompanhamento desses efeitos antropogênicos tem sido realizado por imagens ópticas de sensores orbitais. No período de chuvas, que se estende de novembro a abril, o imageamento óptico da floresta Amazônica fica prejudicado por causa da cobertura persistente de nuvens, o que pode ser contornado por meio de uso de dados de radar de abertura sintética (SAR). Este trabalho teve por objetivo principal apresentar uma técnica de detecção do desmatamento em tempo quase real com a utilização de imagens de radar de acesso livre. Para alcançar esse objetivo, foram publicados três artigos com diferentes abordagens de detecção de efeitos antropogênicos. As áreas de estudo nos artigos se situam no município de Novo Progresso, região conhecida pelas elevadas taxas de ocupação humana dentro do arco do desmatamento, a sudoeste do estado do Pará. O objetivo do primeiro estudo foi analisar como as imagens de radar, ópticas e termais identificam os desmatamentos por corte raso na floresta Amazônica. O estudo correspondeu a uma área de 40 km x 40 km. Foram utilizadas imagens de radar em

bandas X (satélite COSMO-SkyMed) e C (satélite Sentinel-1A), e índices de vegetação por diferença normalizada (NDVI), índices de umidade por diferença normalizada (NDMI) e temperaturas da superfície terrestre (LST) derivadas do satélite Landsat 8. A análise qualitativa revelou informações importantes sobre os limites das áreas e o período de ocorrência dos desmatamentos com boa precisão relativa. Os índices calculados agregaram informações sobre atividades fotossintéticas e níveis de biomassa. A pesquisa mostrou o potencial do uso de índices ópticos e termais e, principalmente, de imagens de radar para identificação dos desmatamentos por corte raso em ambiente de floresta úmida. O segundo artigo foi conduzido para melhor compreender a dinâmica do desmatamento na região, incluindo a fase de queimadas e emissões intrínsecas de gases de efeito estufa. Este estudo foi realizado sobre uma área de 36.800 km^2. Foi identificada uma forte correlação entre ocorrência de incêndios na área recém desmatada seguindo as práticas locais de corte e queima. O terceiro artigo teve como objetivo desenvolver uma metodologia para identificação do desmatamento logo após a sua ocorrência. Esse estudo fez parte de doutorado sanduíche desenvolvido em Roma, Itália, na Universidade Tor Vergata. As imagens de radar na banda C foram processadas para servir de dado primário no desenvolvimento de redes neurais do tipo *MultiLayer Perceptron* (MLP) para identificar desmatamentos por corte raso em tempo quase real. A metodologia desenvolvida identificou áreas de desmatamento de 2 ha ou maiores com alta precisão e de forma automática.

APPLICATION OF ORBITAL SENSORS TO DETECT DEFORESTATION IN THE AMAZON RAINFOREST

Author: Cláudia Arantes Silva

Advisor: Ph.D. Edson Eyji Sano – Embrapa Cerrados

Co-advisor: Ph.D. Fabio Del Frate – Tor Vergata University of Roma

ABSTRACT

The advance of agribusiness in the Amazonian lands has been characterized by a worrying cycle of deforestation, fire, land exploitation, and the opening of new lands. To a large extent, this exploitation takes place in a disorderly manner and at levels much higher than what is allowed by the National Forest Conservation law. After 2012, following the approval of the new Brazilian Forest Code, there was a reversing in the decay of deforestation levels. Since then, the loss of the forest itself and the emission of greenhouse gases (GHG) have been of great concern worldwide. In 2015, during the Paris Agreement, Brazil committed to reduce its GHG emissions, in which deforestation has a great contribution. A great deal of forest claiming due to human occupation occurs within the arc of deforestation, a region that stretches along the extreme south of the Brazilian Amazon. Historically, the monitoring of these anthropogenic effects has been carried out by optical satellite images. During the rainy season, which extends from November to April, optical imaging of the Amazon forest is impaired because of persistent cloud cover, which can be circumvented through the use of synthetic aperture radar (SAR) data. This work aimed to present a technique for detecting near real-time deforestation using open access radar images. This thesis comprises three published articles which describe different approaches to detect anthropogenic effects. The study area is located in the municipality of Novo Progresso, a region known for its high rates of human occupation within the arc of deforestation, in the southwest of the Pará State. The objective of the first study was to analyse how radar, optical, and thermal images identify clear-cut deforestation in the Brazilian Amazon. The study focused on an area of 40 km x 40 km. X-band (COSMO-SkyMed satellite) and C-band (Sentinel-1A satellite) SAR data and Landsat-based normalized difference vegetation index (NDVI), normalized difference moisture index (NDMI), and the land surface temperatures (LST) were used. Qualitative analysis revealed important information about the boundaries of

the areas and the period of occurrence of deforestation with reasonable accuracy. The calculated indices aggregated information about photosynthetic activities and biomass levels. The research showed the potential of using optical and thermal indices and mainly radar images to identify clear-cut deforestation in a tropical forest environment. The second article allowed to better understand the dynamics of deforestation in the region, including the burning phase and intrinsic greenhouse gases emission. This study was carried out over an area of 36,800 km^2. A strong correlation was identified between the occurrences of fire after recent deforestation following local slash-and-burn practices. The third article aimed to present a methodology for identifying deforestation soon after its occurrence. This study was part of a sandwich doctorate developed in Rome, Italy, at the Tor Vergata University. Sentinel-1 C-band radar images were processed and a neural network methodology (MultiLayer Perceptron) was applied to identify clear-cut deforestation in near real-time. The proposed methodology identified, automatically, deforestation areas larger than 2 ha with good accuracy.

ACRONYMS AND ABBREVIATIONS

ABI   Advanced Baseline Imager

AT   Adaptive Thresholding

AVHRR   Advanced Very High Resolution Radiometer

AWIFS   Advanced Wide Field Sensor

CBERS   China-Brazil Earth Resources Satellite

Censipam   *Centro Gestor e Operacional do Sistema de Proteção da Amazônia*

CNNs   Convolutional Neural Networks

dB   Decibel

db   Dry biomass

ESA   European Space Agency

FD   Forested-Deforested

FF   Forested-Forested

FP   False positives

FN   False negatives

GHG   Greenhouse Gas

GLCM   Gray-Level Co-Occurrence Matrix

HU   Humidity

IASI   Infrared Atmospheric Sounder Interferometer

IBAMA   *Instituto Brasileiro do Meio Ambiente e dos Recursos Naturais Renováveis*

ICMBio   *Instituto Chico Mendes de Conservação da Biodiversidade*

INPE   *Instituto Nacional de Pesquisas Espaciais*

IW   Interferometric Wide

LAI   Leaf Area Index

LST   Land Surface Temperature

LULC   Land Use and Land Cover

MetOp   Meteorological Operational satellite

MIR   Middle Infrared

MLC   Maximum Likelihood Classification

MLP	MultiLayer Perceptron
MMD	Maximum-minimum difference
MODIS	Moderate Resolution Imaging Spectroradiometer
MSG	Meteosat Second Generation
NDMI	Normalized Difference Moisture Index
NDVI	Normalized Difference Vegetation Index
NIR	Near Infrared
NMHC	Non-methane hydrocarbon
NN	Neural Network
NOAA	National Oceanic and Atmospheric Administration
NPP	National Polar-orbiting Partnership
OLI	Operational Land Imager
PM	Particulate matter
PRODES	*Projeto de Monitoramento do Desmatamento na Amazônia por Satélites*
PY	PRODES Year
REDD+	Reducing Emissions from Deforestation and Forest Degradation
SAR	Synthetic Aperture Radar
SEVIRI	Spinning Enhanced Visible and Infrared Imager
SWIR	Short Wave Infrared
WFI	Wide Field Imager
TE	Total emission
TIR	Thermal Infrared band
TIRS	Thermal Infrared Sensor
TP	True positives
TN	True negatives
UNFCCC	United Nations Framework Convention on Climate Change
VIIRS	Visible Infrared Imaging Radiometer Suite sensor
VIS	Visible
σ^0	Backscatter signal (sigma naught)

SUMMARY

1. Introduction

Global efforts to mitigate climate change and preserve our unique ecosystems are directly related to reducing forest degradation and deforestation (Aragão et al., 2014). The Amazon contains the largest remaining tropical rainforest in the world. With about 5.2 million km^2, the Brazilian Amazon covers the states of Acre (AC), Amapá (AP), Amazonas (AM), Maranhão (MA), Mato Grosso (MT), Pará (PA), Rondônia (RO), Roraima (RR) and Tocantins (TO), and occupies about 60% of the Brazilian territory. Its importance lies not only in the value of its biodiversity but also in the existence of the original cultures that are part of this ecosystem (Fearnside, 2021).

Anthropogenic disturbances in the Brazilian Amazon occur through selective logging (degradation), corresponding to the removal of tree species of high economic value and mostly by slash and burning, causing the complete removal of original vegetation. Selective logging of long-standing trees affects significantly the structure and the floristic diversity of forests over time (Bezerra et al., 2021). The persistence of endemic bird species of high conservation value in the Amazon is threatened by human-induced deforestation (Anjos et al., 2021).

Fire-induced tree mortality, related to the slash and burn practices, causes losses in the functional and phylogenetic diversity of trees at higher rates than in taxonomic diversity (Nóbrega et al., 2019). Recurrent fires affect the forest structure, species richness, and composition and reduce the biomass of living trees, causing impacts on birds and vegetation (Silveira et al., 2016).

A deeper understanding of the forest dynamics helps mitigating the deforestation effects, carbon cycle estimates, and to characterize how the environment adapts to the microclimatic changes. Whenever possible, these studies should be based on multi-scale remote sensing tools (Bustamante et al., 2016).

Environmental damage to the Amazon forest has reached critical levels. Deforestation is increasing rapidly and conservation policies are insufficient. Remote sensing techniques allow the rapid detection of deforestation and forest degradation over large territorial extensions. While reducing field research, the interoperability of Earth observation technologies is essential for national forest monitoring systems. An area of the size of the Amazon rainforest demands continuous monitoring through satellite and, preferable, from freely accessible data, such as the China-Brazil Earth

Resources Satellite (CBERS), Landsat, and Sentinel-2 satellites. Brazil strongly relies on these missions to monitor such a large territory.

Through the partnership between the Brazilian and Chinese governments, CBERS program is the main provider of optical images of the Brazilian territory. Since March 2020, CBERS-4 and CBERS-4A satellites are providing most of the optical images that are employed by our remote sensing community. The Multispectral Camera (MUX) provides imagery in the blue, green, red, and near-infrared (NIR) spectral bands with the spatial resolutions of 20 m (CBERS-4) and 16 m (CBERS-4A). The Landsat 8 satellite from the National Aeronautics and Space Administration (NASA), launched in February 2013, carries two sensors, the Operational Land Imager (OLI), with a spatial resolution of 30 m, and the Thermal Infrared Sensor (TIRS) with a spatial resolution of 100 m (Barsi et al., 2014; Knight & Kvaran, 2014). The Sentinel-2 satellite, from the European Space Agency (ESA), was launched in June 2015 and produces images of 10 m spatial resolution. In February 2021, Brazil began to operate the Amazonia-1 satellite designed by the National Institute for Space Research (INPE). The satellite carries an advanced Wide Field Imager (WFI) sensor which acquires images in four spectral bands from blue to NIR, swath width of 850 km, and spatial resolution of 60 m.

Scientific studies from open-access optical sensors have been successfully applied to monitoring forest change, deforestation, and forest degradation (DeVries et al., 2016, Kranz et al., 2018; Crowson et al., 2019; Wang et al., 2019). However, the persistent presence of clouds makes monitoring by optical sensors difficult in tropical forest environments throughout the year. Such limitation does not occur with synthetic aperture radar (SAR) sensors (Meneses and Almeida, 2012; Woodhouse, 2015). SAR sensors use their own energy and utilize longer, centimeter to meter wavelenghts, allowing them to see terrain through clouds at any time of the day. For environmental applications, the X-band (~2.5 cm) has little penetration into the vegetation cover, interacting mostly with the leaves. The C-band (~5 cm) has low to moderate penetration, interacting with leaves and branches. The L-band (~27 cm) has high penetration, allowing interaction with trunks and branches and can be applied for biomass and vegetation mapping.

The C-band Sentinel-1 satellite provides open access satellite data. The Sentinel-1 mission is composed of a constellation of two satellites, the Sentinel-1A and the Sentinel-1B. They operate in the same orbit with an orbital phasing difference of 180° and produce images in almost any weather conditions, with a spatial resolution of 10 m

(Torres et al., 2012). The Sentinel mission encourages the development of new SAR data integration techniques that may assist operational monitoring of large forest areas.

2. Problem, justification, and contribution

The Brazilian Amazon covers about 60% of the Brazilian territory. Intense cloud cover lasts for more than half of the year. Currently, the methodologies based on optical sensors are applied to produce deforestation alerts for environmental law enforcement procedures and for long-time, clear-cut deforestation monitoring. The drawback is the monitoring during the raining season so that the country needs to develop new methods for near real-time forest surveillance based on SAR data.

In the Brazilian Amazon, the arc of deforestation is the region with the highest occurrence of deforestation and land occupation (Azevedo-Ramos et al., 2018; Souza et al., 2020). This region concentrates of total deforestation of the Brazilian Amazon, mostly for soybean plantation and cattle ranching (Nepstad 1999, Soares-Filho et al., 2006). Since 2006, Pará State presents the highest levels of deforestation in the Brazilian Amazon.

The main objective of this research is to propose and validate a set of methodologies to help monitor anthropogenic disturbances in the Brazilian rainforest, based on different orbital sensors from a broad range of spatial and temporal resolutions. Depending on the method, a combination of sensors was used. Most of illegal activities of forest disturbances take place in the raining season. Therefore, the research also deals with tropical forest monitoring based on radar sensor. An algorithm, created on SAR data automatic vegetation cover disturbance, is proposed.

For those, an extensive bibliographical review was carried out and the main objectives were attained in tree scientific papers. The study area was the Novo Progresso region, southwest of the Pará State, along the BR-163 highway, where high levels of deforestation and land occupation are taking place. First, the deforestation detection was carried out combining radar, optical and thermal sensors. Second, we showed the correlation between deforestation and fire occurrences and the greenhouse gas (GHG) estimates. Last, an automatic technique based on neural network was applied to radar images to identify near real-time deforestation.

Paper # 1

The research titled "Qualitative analysis of deforestation in the Amazon forest from SAR, optical and thermal sensors" aimed to analyze qualitatively the spectral responses of clear-cut deforested areas in the Brazilian Amazon using the X- and C-bands SAR images, combined with optical and thermal data. The research covered and area of 40 km x 40 km located in the municipality of Novo Progresso, Pará State, where high deforestation rates are observed. The study was based on a multi-temporal analysis of the SAR data acquired by the COSMO-SkyMed (X-band) and Sentinel-1A (C-band) satellites and by optical and thermal images acquired by the Landsat 8 satellite during the period from 2016 to 2018.

The SAR data were converted into backscattering coefficients of different polarizations and ratios. Covariance, gradient, minimum value, maximum value, and standard deviation from three periods (2016–2017, 2017–2018, and 2016–2018) were considered to highlight the boundaries of deforested. The results were presented in the RGB color composites. The optical and thermal data were analyzed after converting into the Normalized Difference Vegetation Index (NDVI), Normalized Difference Moisture Index (NDMI), and Land Surface Temperature (LST). In this case, deforested areas were highlighted based on contrast between primary forest and deforested areas in terms of these three attributes (green vegetation, moisture, and surface temperature).

The deforestation detection was validated based on deforestation polygons obtained by the 3−6 m spatial resolution COSMO-SkyMed SAR images from the year 2016 and on the data produced by the Near Real-Time Deforestation Detection System (DETER-B) from 2017 and 2018. The polygons were overlaid in the Landsat 8 RGB color composites (RGB/654) obtained during the dry seasons of 2015, 2016, 2017 and 2018. The SAR technology proved to be useful in identifying deforested areas during the rainy season in the Amazon forest. The RGB multitemporal combinations highlighted the deforested areas. The article is available for download in the following link: https://revistas.ufrj.br/index.php/aigeo/article/view/31314/17792.

Paper # 2

The second article titled "Fire occurrences and greenhouse gas emissions from deforestation in the Brazilian Amazon" addressed the relation between fire occurrence

in the forest caused by deforestation after slash-and-burn practices and the estimates of greenhouse gas (GHG) emissions in the surroundings of the Novo Progresso municipality, Pará State.

The investigation was based on deforestation and fire data from 2007 to 2019 reported by INPE. The study area is fully inserted in the arch of deforestation which concentrates 77% of the total deforestation in the Brazilian Amazon. Fires occurrences within the primary forest were investigated to assess ecosystem degradation. The work also presents the amount of GHG emitted from the first deforestation process along the Brazilian rainforest in 2019.

It is important to highlight that the intact forest does not sustain large fires in the Brazilian Amazon, due to the high levels of moisture, even during the dry season. Fire occurrences in the humid tropical forest are observed in dead trees and along the duff layer. The understory vegetation may propagate flame in the surroundings of large cleared areas (edges of degraded forests) in combination with an intense dry season. Flame propagation through the understory vegetation is too weak to be captured by satellite sensors. Therefore, the fire hotspots inside the intact forest may be due to the flaming of large naturally dead trees or along open forest trails where small slashed trees sustain the fire. Selective logging also degrades the area around the large fallen trees, making the vicinity prone to propagate flame. Fire occurrences inside the standing forest are restricted to degraded forest caused by the previously discussed events or their combined effects.

Deforestation data was also used to assess GHG emissions from slash-and-burn practices. Total GHG emission for the Amazon was limited to the burning of the newly deforested area corrected by the average regrowth of secondary forest. The research showed a good correlation between the occurrences of fire in the newly deforested area in the municipality of Novo Progresso following the local slash-and-burn practices. The same trends were also observed for the Pará State, suggesting a common practice within the arch of deforestation. For PY2018–2019 (PY = PRODES-Year), the emissions after deforestation practices in the Novo Progresso region were about 8.81 Mton of CO_2.

The incidence of fire outbreaks in forest areas nearby new cleared and burned areas confirm the strong impact of deforestation on ecosystem degradation due to the occurrence of fires in the Brazilian Amazon. The article also discussed the increase in deforestation and degradation in the Brazilian Amazon with the approval of the new

Brazilian Forest Code in 2012 (Law 12,651 of 25 May 2012). The article is available for download in the following link: https://www.mdpi.com/2072-4292/13/3/376.

Paper # 3

After understanding the dynamics of deforestation in the Amazon rainforest and considering its dimension, a third article was written where a methodology to identify near real-time deforested areas using climate-independent and open-access satellite imagery was proposed. The paper titled "Near-real time deforestation detection in the Brazilian Amazon with Sentinel-1 and Neural Networks" proposed a methodology based on neural network and C-band, VV- and VH-polarized Sentinel-1A data for rapid deforestation detection.

The research was conducted in an area that covers part of the municipalities of Altamira, Itaituba, and Novo Progresso, located in the southwest of the Pará State. This region shows the highest deforestation rates in this state. A set of 30 Sentinel-1 images from 2019 was used for training the neural network algorithm. Another set of 30 Sentinel-1 images from 2018 were used for the algorithm validation and automatic identification of near real-time deforestation. During the algorithm training step, statistical parameters (mean backscattering coefficients and their corresponding standard deviation and maximum-minimum difference) were calculated from Forested-Forested (forested areas) and Forested-Deforested (forested areas that were deforested) areas. Statistical data were used as input parameters for the NN classifier. The Multi-Layer Perceptron (MLP) structure was used to map deforestation considering a minimum area of 2 ha. Four different case studies were analyzed for both polarizations:

(1) mean $\sigma°$ values;

(2) mean $\sigma°$ values and corresponding standard deviation;

(3) mean $\sigma°$ values and corresponding maximum-minimum difference values; and

(4) mean $\sigma°$ values and corresponding standard deviation and maximum-minimum difference values.

In the algorithm training phase, the data set was divided into training (75%), validation (15%), and testing (10%) sets. The training and validation sets were used during the algorithm training process, while the test set was used to assess the

performance achieved in the two previous phases. Network training is achieved whenever the error in the validation dataset reaches its minimum. After the training phase, the algorithm was applied to a new data set. The trained model was then applied to radar images from 2018 for automatic recognition of deforested areas. The neural network results from the 2018 data set were validated using data published by the MapBiomas and PRODES projects. Differences in results between the two projects were discussed and presented in the article. The manuscript was submitted to the European Journal of Remote Sensing on July 2021 and currently is under the second round of review.

Análise Qualitativa do Desmatamento na Floresta Amazônica a partir de Sensores SAR, Óptico e Termal
Qualitative Analysis of Deforestation in the Amazonian Rainforest from SAR, Optical and Thermal Sensors

Claudia Arantes Silva[1]; Giancarlo Santilli[2]; Edson Eyji Sano[3] & Suzan Waleska Pequeno Rodrigues[1]

[1]Universidade de Brasília (UnB), Instituto de Geociências,
Departamento de Geologia Geral, Campus Universitário Darcy Ribeiro, 70.910-900, Brasília, DF, Brasil
[2]Universidade de Brasília (UnB), Faculdade do Gama, Engenharia Aeroespacial,
St. Leste Projeção A, Gama Leste, 72.444-240, Brasília, DF, Brasil
[3]Instituto Brasileiro do Meio Ambiente e dos Recursos Naturais Renováveis (IBAMA),
SCEN L4 Norte, 70818-900, Brasília, DF, Brasil
E-mails: arantes.claudia16@gmail.com; santilli@aerospace.unb.br; edson.sano@ibama.gov.br; suzanpequeno@unb.br

Resumo

A mitigação de mudanças climáticas e preservação de ecossistemas depende da redução do desmatamento e degradação de florestas tropicais. O objetivo deste estudo foi analisar imagens de radar, ópticas e termais para identificar desmatamentos por corte raso no período de 2016 a 2018 em uma área localizada no arco de desmatamento da Amazônia. Foram utilizadas imagens de radar em bandas X (satélite COSMO-SkyMed) e C (satélite SENTINEL-1A), índices de vegetação por diferença normalizada (NDVI), índices de umidade por diferença normalizada (NDMI) e temperaturas da superfície terrestre (LST) (satélite Landsat-8). As áreas com evidências de antropismo mapeadas com base nas imagens do satélite COSMO-SkyMed no município de Novo Progresso (PA), período de 2016 a 2018, foram utilizadas como máscara inicial. Imagens de radar identificaram, com boa precisão relativa, as épocas e as áreas de desmatamento. NDVI e NDMI evidenciaram, respectivamente, quedas nas atividades fotossintéticas e nos níveis de biomassa nas áreas de desmatamento identificadas. Já a LST foi mais elevada nas áreas de rebrota em relação à vegetação densa. A análise do potencial de imagens de radar, ópticos e termais mostrou elevada relevância na detecção de desmatamento por corte raso em ambiente florestal úmido.
Palavras-chave: Floresta tropical; Degradação; Análise temporal

Abstract

The mitigation of climate change and the preservation of ecosystems depends on the reduction of deforestation and degradation of tropical forests. The objective of this study is to analyze radar, optical, and thermal images to identify clear cut deforestation from 2016 to 2018 in an area located in the arch of deforestation of the Amazon forest. We used X-(COSMO-SkyMed satellite) and C-bands (SENTINEL-1A satellite) radar data, normalized difference vegetation index (NDVI), normalized difference moisture index (NDMI), and land surface temperature (LST) (Landsat-8 satellite). We considered, as an initial mask, the areas with evidence of anthropogenic actions in the municipality of Novo Progresso (PA), from 2016 to 2018. Radar features were able to be identified, with relative accuracy, the time and the area of deforestation. NDVI and NDMI indices showed, respectively, decrease in the photosynthetic activities and the biomass levels in deforested areas. On the other hand, the LST was higher in regrowth areas than in dense vegetation. The analysis of potential of radar, optical, and thermal data showed to be relevant in the identification of clear cut deforestation in tropical rainforest environment.
Keywords: Tropical forest; Degradation; Temporal analysis

1 Introdução

As ações para reduzir o desmatamento e a degradação das florestas estão diretamente relacionadas aos esforços globais para preservar os ecossistemas únicos de nosso planeta e mitigar as mudanças climáticas (Aragão *et al*., 2014). Para mitigação e adaptação decorrente de mudanças climáticas e estimativas do ciclo do carbono, é fundamental um monitoramento integrado para obter um entendimento mais assertivo da dinâmica dos processos na floresta. A floresta tropical da Amazônia possui uma extensão territorial de 5,5 milhões de km^2. O desmatamento da floresta Amazônica por ações antropogênicas ocorre principalmente por meio de corte seletivo e corte raso. O corte seletivo é a retirada de espécies de árvores com valor econômico elevado. No processo de extração, ocorre a derrubada de árvores vizinhas que se encontram na trajetória de queda da árvore derrubada. Esse processo é realizado principalmente por madeireiros e antecede o corte raso, que corresponde à retirada completa da vegetação. Nas práticas de manejo da terra, realizadas principalmente por pecuaristas e fazendeiros, clareiras são abertas, a floresta então é derrubada e queimada (Morton *et*

al., 2006; Matricardi *et al*., 2010; Domingues & Bermann, 2012; Souza *et al*., 2017).

A dinâmica do desmatamento nas florestas tropicais se inicia pelas bordas florestais (Nepstad *et al*., 1999, 2001; Cochrane, 2003) (Figura 1). As aberturas de caminhos e estradas dentro da floresta permitem o acesso de colonos em áreas antes inacessíveis, fragmentam a floresta, a umidade diminui e o microclima local é alterado e a floresta torna-se mais vulnerável ao fogo. Os incêndios florestais e as emissões de fumaças acarretam diminuição das chuvas; as áreas previamente queimadas são mais propensas às reincidências. A resiliência do ecossistema diminui, tornando a floresta mais susceptível a incêndios e outros danos. O aumento no nível de degradação da floresta e mudanças no estoque de carbono foram reportados por diversos autores como Arima *et al*. (2005), Soares-Filho *et al*. (2006), Broadbent *et al*. (2008), Butt *et al*. (2011), Knox *et al*. (2011), Davidson *et al*. (2012), Barros & Fearnside (2016) e Jusys (2016). Durante o manejo da terra, incêndios podem penetrar em florestas degradadas ou intactas na forma de fogo de superfície (Guenther *et al*., 2017), cujos danos são mais difíceis de serem documentados (Asner *et al*., 2005).

Figura 1 Dinâmica de desmatamento e degradação da floresta Amazônica (modificado de Cochrane 2003).

O monitoramento de desmatamento baseado em satélites é uma ferramenta essencial nos estudos de efeitos antropogênicos em florestas tropicais, pois permite a identificação das diferentes formas de exploração das florestas e manejo da terra em grandes extensões territoriais, com tempo de revisita adequado e um custo razoável (Hosonuma *et al*., 2012; Hansen *et al*., 2013; Thompson *et al*., 2013; Aragão *et al*., 2014; Bustamante *et al*., 2016; Mitchell *et al*., 2017). Historicamente, técnicas de sensoriamento remoto têm desempenhado um papel fundamental no monitoramento da cobertura vegetal dos biomas brasileiros, conforme relatado por Ferrreira *et al*. (2008), Souza *et al*. (2013) e Carreiras *et al*. (2017). Porém, durante os meses de chuva, a cobertura persistente de nuvens cria uma forte limitação para o uso de sensores ópticos. É durante o período chuvoso que ocorre a intensificação de cortes raso e seletivo de árvores na Amazônia. Nos meses de seca, a baixa umidade relativa do ar favorece a queima de árvores derrubadas e posterior transformação em áreas de pastagens. A despeito da limitação do emprego de sensores ópticos pela presença de nuvens, os mesmos ainda são amplamente utilizados no monitoramento da floresta Amazônica (INPE, 2013; Shimabukuro *et al*., 2015; Grecchi *et al*., 2017).

Os sensores de radar de abertura sintética (SAR) praticamente não sofrem interferência atmosférica, pois conseguem atravessar as nuvens e, portanto, permitem a aquisição de dados independentemente da estação climática, permitindo o monitoramento contínuo do desmatamento, focos de incêndios e rebrota (Bernhard *et al*., 2011; Reiche *et al*., 2015; Martone *et al*., 2018). Dados SAR permitem, por meio da análise de retroespalhamento volumétrico da vegetação, a produção de informações sobre cobertura vegetal, copa, galhos e troncos (Henderson & Lewis, 1998; Aboud Neta *et al*., 2010; Ernhard *et al*., 2011; Lardeux *et al*., 2011; Capodici *et al*., 2013; Lei *et al*., 2018).

O objetivo dessa pesquisa é apresentar uma análise qualitativa de imagens SAR nas bandas X e C, ópticas e termal para identificar desmatamento por corte raso em uma área localizada no arco de desmatamento na floresta Amazônica. A metodologia testada acrescenta informações sobre como os diferentes comprimentos de onda em que os sensores de radar operam respondem ao desmatamento em um ambiente de floresta tropical úmido. Espera-se que esse estudo possa acrescentar informações que auxiliem em metodologias futuras de controle de desmatamento em larga escala.

2 Métodos
2.1 Área de Estudo

A área de estudo localiza-se na região sudeste da Amazônia Legal, a norte do município de Novo Progresso, estado do Pará (PA) (Figura 2). A porção leste da área é cortada pela rodovia BR-163. A maioria dos desmatamentos na região são convertidos em áreas de pastagem e em áreas de cultivo agrícola. O clima é marcado por um período úmido e um período seco mais prolongado (Figura 3).

2.2 Dados de Sensoriamento Remoto

Para esse estudo, foram utilizadas imagens de radar em banda X do satélite COSMO-SkyMed, banda C do satélite Sentinel-1A, imagens ópticas e termais do satélite Landsat-8, sensor *Operational Land Imager* (OLI) nas bandas 4 (vermelho, 0,64 – 0,67 µm), 5 (infravermelho próximo, 0,85 – 0,88 µm) e 6 (infravermelho de ondas curtas, 1,57 – 1,65 µm) e sensor *Thermal Infrared Sensor* (TIRS) na banda 10 (infravermelho termal, 10,6 – 11,19 µm) do período de 2016 a 2018. Imagens ópticas de 2015 foram utilizadas para realçar a presença de floresta intacta (antes dos desmatamentos ocorridos a partir de 2016).

O sistema italiano COSMO-SkyMed consiste em uma constelação de quatro satélites de médio porte, de baixa órbita terrestre e no mesmo plano orbital, cada um equipado com um sensor em banda X (Covello *et al*., 2010). As imagens do COSMO-SkyMed foram adquiridas pelo Centro Gestor e Operacional do Sistema de Proteção da Amazônia (Censipam) no período de 2016 a 2018 e no modo de imageamento *StripMap*, *HighImage*, faixa de imageamento de 40 km e polarização HH. Foram selecionadas imagens de abril de cada ano (Tabela 1).

As imagens do Sentinel-1A são obtidas pela Agência Espacial Europeia (ESA), composta por uma constelação de dois satélites A e B que compartilham o mesmo plano orbital (Torres *et al*., 2012). As imagens são de acesso livre e foram selecionadas de acordo com as datas próximas às imagens do COSMO-SkyMed. Na área de estudo, haviam dis-
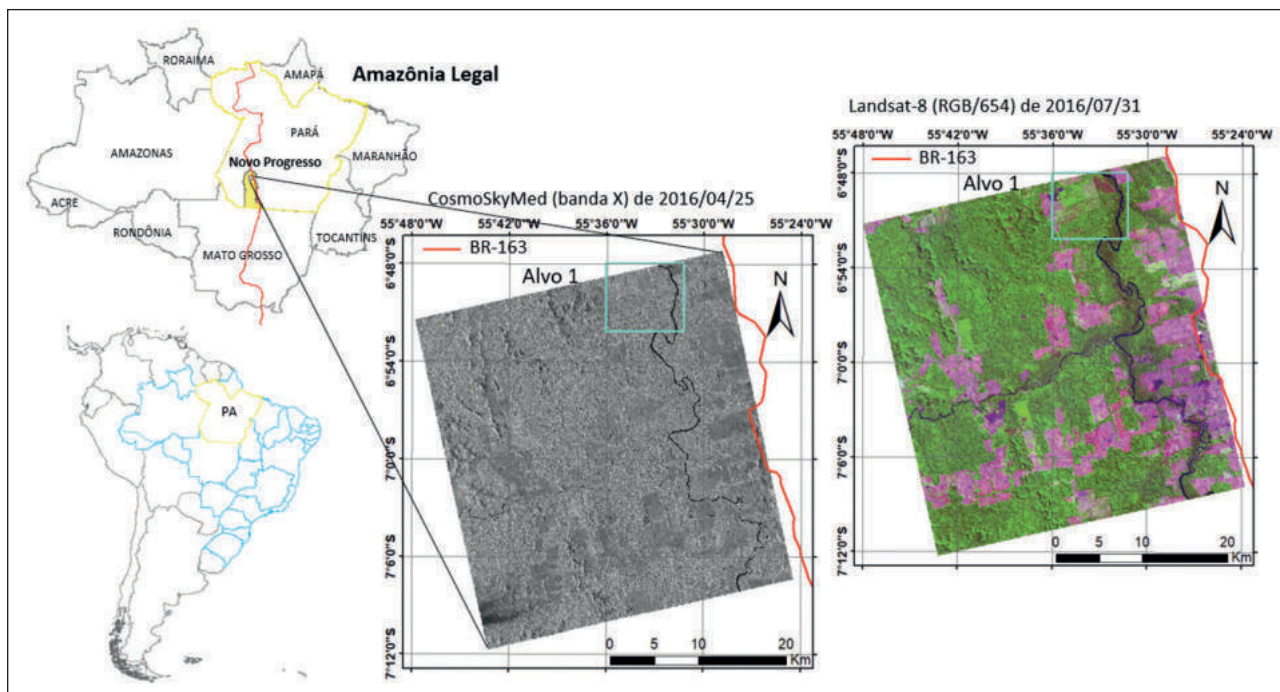
Figura 2 Mapa de localização da área de estudo em imagens dos satélites COSMO-SkyMed e Landsat-8 de 2016. Alvo 1 corresponde a um maior detalhamento da imagem apresentado nas Figuras 5 e 6.
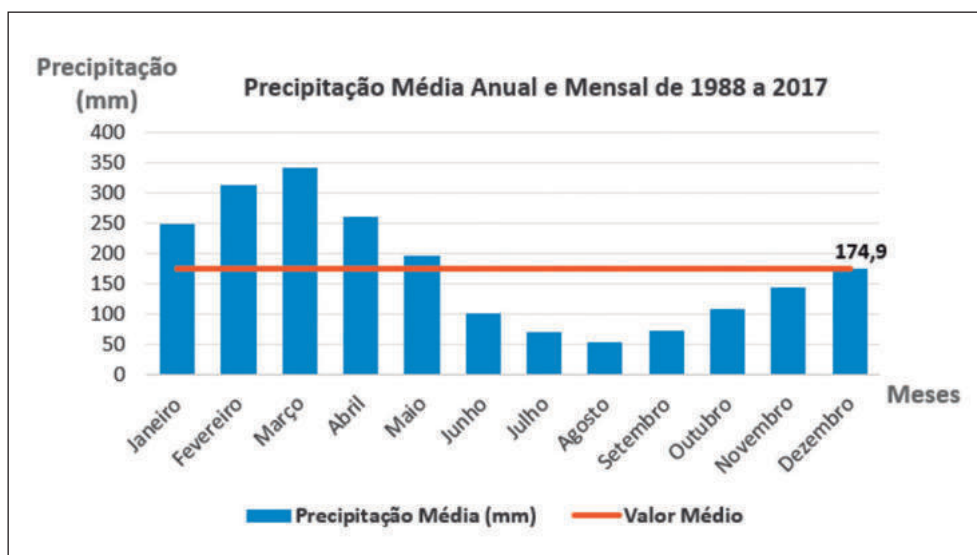
Figura 3 Precipitação média anual e mensal da série temporal de 1988 a 2017 da região de Novo Progresso (retirado de INMET, 2019).

Tabela 1 Datas de aquisição das imagens utilizadas: COSMO-Sky-Med (banda X), Sentinel-1 (banda C) e Landsat-8 (bandas: vermelho, infravermelho próximo, infravermelho de ondas curtas e infravermelho termal).

Ano	Satélite		
	COSMO-SkyMed	Sentinel-1A	Landsat-8
2015	-	-	14 de agosto
2016	25 de abril	19 de janeiro	31 de julho
2017	07 de abril	19 de abril	03 de agosto
2018	08 de abril	08 de maio	05 de julho

poníveis imagens no modo de aquisição *Interferometric Wide* (IW), faixa de imageamento de 250 km e polarizações VV e VH.

As imagens ópticas foram obtidas pelo satélite norte-americano Landsat-8 que opera com dois sensores denominados de OLI e TIRS (Barsi *et al.*, 2014; Knight & Kvaran, 2014). Os dois sensores proporcionam imagens coincidentes da superfície terrestre, porém, em diferentes regiões espectrais. Foram selecionadas imagens ópticas da cena 227/65 dos sensores OLI e TIRS, com presença mínima de cobertura de nuvens. Todos os dados foram projetados para o sistema de coordenadas geográficas, *datum* WGS84.

2.3 Processamento das Imagens

A Figura 4 apresenta a metodologia de processamento aplicada para as imagens SAR, ópticas e termal. As imagens SAR (bandas X e C) foram utilizadas a partir do nível de processamento *Single Look Complex* (SLC). As imagens do COSMO-SkyMed seguiram o procedimento padrão de processamento sugerido pela Agência Espacial Italiana por meio do programa *SARscape* (ISA, 2009). A análise multi-temporal (*change detection*) foram aplicadas para detectar as mudanças ocorridas entre as imagens no período de 2016 a 2018. A técnica de detecção de mudança multi-temporal (Lu *et al.*, 2004) faz uma análise de imagens na mesma posição geográfica em diferentes datas para identificar quaisquer mudanças ocorridas entre as duas datas. Foram calculados os seguintes parâmetros estatísticos: covariância, gradiente, valor mínimo, valor máximo, média, mediana e desvio-padrão para investigar as alterações de retroespalhamento de múltiplas imagens ao longo do tempo.

As imagens SAR do Sentinel-1A foram processadas utilizando o *software SNAP* da ESA. Depois de processados, esses dados foram analisados por meio de divisão de bandas e combinação das diferentes polarizações. Os valores digitais das imagens do Landsat-8 foram convertidos para reflectância na superfície terrestre, aplicando-se a técnica de remoção de nuvens por meio do *plug-in* RS & GIS, disponível no programa QGIS. Posteriormente, foram calculados o NDVI, o NDMI e a LST por meio das seguintes equações:
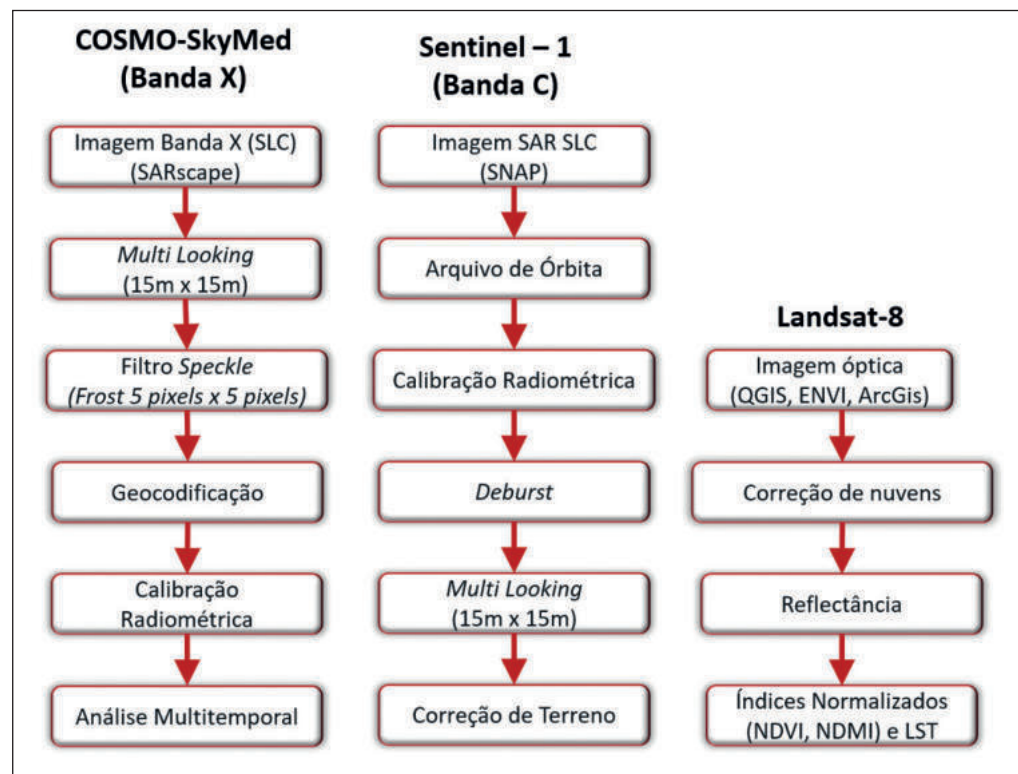

Figura 4 Fluxo de processamento digital das imagens SAR (bandas X e C), ópticas e termal.

$$NDVI = \frac{Red - NIR}{Red + NIR} \qquad (1)$$

$$NDMI = \frac{SWIR - NIR}{SWIR + NIR} \qquad (2)$$

$$LST = \frac{k_1}{\ln\left(\frac{k_2}{L_i+1}\right)} \qquad (3)$$

onde Red, NIR e SWIR correspondem às reflectâncias nas faixas espectrais do vermelho, infravermelho próximo e infravermelho de ondas curtas, respectivamente; k_1 e k_2 correspondem a constantes de conversão das bandas termais; e L_i refere-se à radiância no topo da atmosfera.

2.4 Dados de Referência

Foram utilizados, como dados de referência de áreas desmatadas, as composições coloridas de imagens ópticas entre 2015 e 2018; os polígonos de desmatamento do sistema de detecção de indicativos de desmatamento em tempo quase real (DETER-B) do Instituto Nacional de Pesquisas Espaciais (INPE) para os anos de 2017 e 2018; e os polígonos de desmatamento (T0) mapeados pelo Censipam em 2016. As composições coloridas RGB das imagens ópticas foram formadas com as bandas espectrais 6 (SWIR), 5 (NIR) e 4 (RED), respectivamente.

O INPE, por meio do Projeto de Monitoramento do Desmatamento na Amazônia por Satélites (PRODES), tem calculado as taxas anuais de desmatamento por corte raso em áreas maiores que 6,25 hectares na Amazônia Legal brasileira (INPE, 2013). O sistema faz uso de dados ópticos de resolução espacial moderada provenientes principalmente dos satélites Landsat (30 m de resolução espacial e revisita de 16 dias) e CBERS (20 metros de resolução espacial e revisita de 26 dias). Esse monitoramento é possível de ser realizado apenas de seis a oito meses no ano, correspondente ao período seco, o que é insuficiente para ações de prevenção, fiscalização e controle do desmatamento em curto prazo (Escada *et al.*, 2010).

Com o objetivo de apoiar a vigilância e o controle do desmatamento, o INPE vem desenvolvendo sistemas complementares de monitoramento.

Esse é o caso do DETER-B, baseado em imagens do sensor *Wide Field Imager* (WFI) a bordo do satélite CBERS-4 (resolução espacial de 64 m) e principalmente em imagens do *Advanced Wide Field Sensor* (AWIFS) do satélite indiano Resourcesat-1, com resolução espacial de 56 m e resolução temporal de 5 dias (Diniz *et al.*, 2015). O DETER-B demonstrou ser capaz de indicar alterações florestais em diferentes estágios de degradação, contribuindo para o combate de desmatamento no arco de desflorestamento localizado na Amazônia Legal.

Durante o período de chuvas, em que o monitoramento por meio de satélites ópticos do INPE fica prejudicado, o Censipam colabora com os órgãos federais de fiscalização (IBAMA e ICMBio). Com base nos dados do PRODES, o IBAMA define os *hotspots* de desmatamento para que o Censipam, por meio de imagens radar, possa mapear os polígonos menores, mais difíceis de serem identificados por sensores de resolução moderada, gerando alertas de desmatamento na Amazônia em tempo próximo ao real. O Censipam faz uso de imagens em banda X do satélite italiano COSMO-SkyMed e mapeia as áreas desmatadas, com resolução espacial de 3 a 6 m, chamada base T0. Desde 2016, a área monitorada tem sido de 300.000 km² mensais, no período compreendido entre outubro a abril nos estados da Amazônia.

3 Resultados

Foi realizada uma análise temporal calculando-se, sobre pares de imagens, a covariância, o gradiente, o valor mínimo, o valor máximo e o desvio-padrão para três períodos: 2016 a 2017; 2017 a 2018; e 2016 a 2018. Os resultados são apresentados em composições coloridas RGB que melhor evidenciaram os limites das áreas de desmatamento e os períodos aproximados de ocorrência. A Figura 5 apresenta as combinações temporais RGB das imagens do COSMO-SkyMed dos parâmetros calculados na análise temporal. Em todas as composições coloridas, no canal vermelho (R) foram inseridas as imagens do período de 2016 a 2017, no canal verde (G), as imagens de 2016 a 2018 e no canal azul (B), as imagens de 2017 a 2018. Imagens do Landsat-8 foram selecionadas durante os períodos secos dos anos de 2015, 2016, 2017 e 2018 para comparação e validação visual das mudanças ocorridas na área.

Nas imagens de covariância (A) e gradiente (B), as áreas desmatadas durante o período de 2016 a 2017 foram evidenciadas pela coloração amarela. As colorações em ciano e magenta mostram mudanças ocorridas entre 2017 e 2018. Porções da área de coloração escura a preta mostram áreas desmatadas mais antigas. A imagem de valores máximos (C) não se mostrou adequada para definir as áreas de desmatamento. A imagem de valores mínimos (D) apresentou uma textura mais lisa das áreas desmatadas mais antigas. Dos parâmetros temporais calculados, o gradiente (B) e o valor mínimo (D) mostraram-se mais eficientes em diferenciar as áreas que sofreram alteração e as áreas de desmatamento mais antigas. A combinação de desvio-padrão não foi mostrada na figura por apresentar as mesmas características do gradiente (B).

Uma segunda avalição foi realizada para o período total de 2016 a 2018, combinando-se os melhores resultados da análise dos parâmetros temporais calculados (covariância, gradiente e valor mínimo), imagens de retroespalhamento (σ^0, unidade em dB) e diferenças de bandas (Figura 6). Na imagem cov-min-grad (A) (composição RGB: R = covariância;

G = valor mínimo; e B = gradiente), as áreas que sofreram alteração entre 2016 e 2018 foram evidenciadas pela cor magenta e as áreas desmatadas mais antigas apresentaram-se com padrão verde escuro. Na imagem dif-min-grad (B) (composição RGB: R = diferença de σ^0 de 2016-σ^0 de 2018; G = valor mínimo; e B = gradiente), o padrão azulado permitiu definir melhor os limites das áreas que sofreram alteração, quando comparada com a imagem cov-min-grad (A). As áreas desmatadas mais antigas puderam ser observadas na cor marrom. Na imagem dif- σ^0_16-σ^0_18 (C) (composição RGB: R = diferença entre σ^0 de 2016 e σ^0 de 2018; G = σ^0 de 2016; e B = σ^0 de 2018), as áreas em coloração verde claro corresponderam às áreas alteradas em 2016. Porções em verde escuro mostraram áreas desmatadas mais antigas e, nas porções mais azuladas, áreas que foram desmatadas em 2018. Na imagem σ^0_16- σ^0_17- σ^0_18 (D) (composição RGB: R = σ^0 de 2016; G = σ^0 de 2017; e B = σ^0 de 2018), a coloração RGB correlacionou-se com os períodos aproximados de desmatamento. Tons amarelos evidenciaram os desmatamentos ocorridos entre 2016 e 2017, tons azulados, os desmatamentos mais recentes (ocorridos entre 2017 e 2018) e os tons mais escuros, as áreas desmatadas
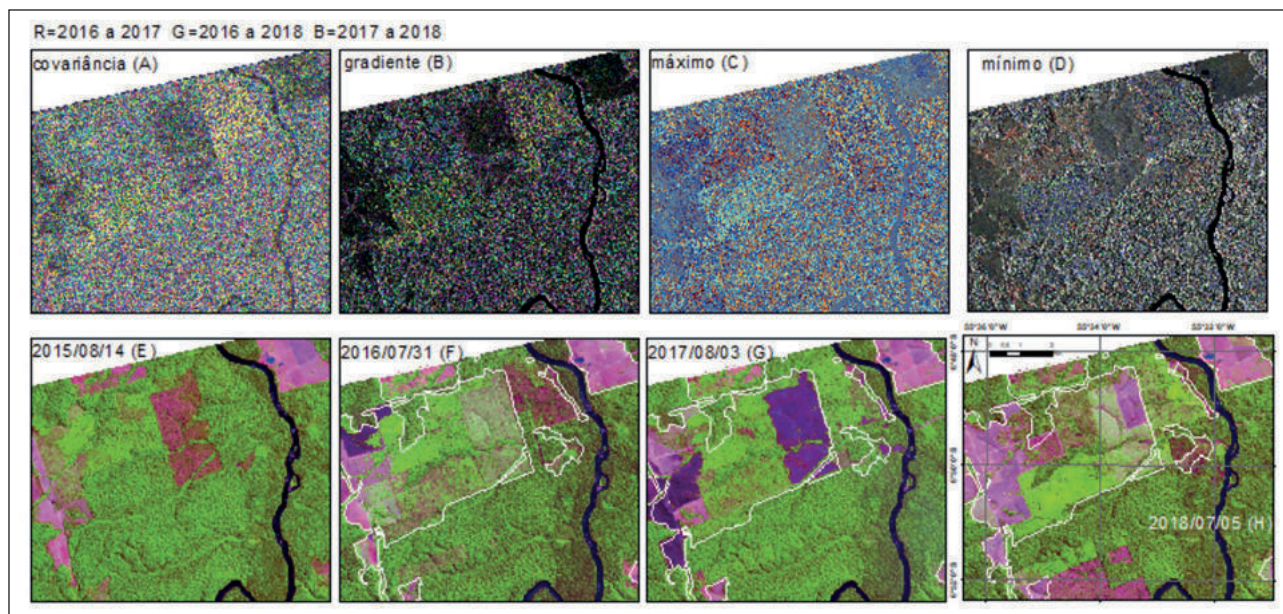
Figura 5 Composições coloridas RGB bitemporais (R = 2016 a 2017; G = 2016 a 2018; e B = 2017 a 2018) derivados dos parâmetros covariância (A), gradiente (B), valor máximo (C) e valor mínimo (D) do satélite COSMO-SkyMed. Na parte inferior da figura, são mostradas as composições coloridas RGB/654 do satélite Landsat-8 obtidas em 2015/08/14 (E), 2016/07/31 (F) (com polígonos de desmatamento T0), 2017/08/03 (G) (com polígonos de desmatamento T0 e DETER-B de 2017) e 2018/07/05 (H) (com polígonos de desmatamento T0 e DETER-B de 2018).

já bem consolidadas. Todas as composições RGB das imagens do COSMO-SkyMed apresentaram bons resultados para detecção e discriminação das áreas desmatadas.

Na parte inferior da Figura 6, a primeira imagem à esquerda (I) é composta por imagens do satélite Sentinel-1A (composição RGB: R = σ^0_VH de 2016; G = σ^0_VH de 2017; e B = σ^0_VH de 2018). As áreas que sofreram alteração apresentaram tons amarelos e verdes e áreas desmatadas bem consolidadas em coloração marrom, porém, os limites dessas áreas ficaram pouco definidos. Nas imagens de retroespalhamento dos anos de 2016 (J), 2017 (K) e 2018 (L) (composição RGB: R = σ^0_VV; G = σ^0_VH; e B = diferença VV-VH), não foi possível diferenciar

novas áreas de desmatamento. Os tons escuros nas imagens corresponderam às áreas de desmatamentos bem estabelecidos.

A expansão do desmatamento no arco de desflorestamento da Amazônia ocorre seguindo uma dinâmica de corte seletivo e derrubada da floresta, implantação da pecuária e transformação posterior da área em agricultura mecanizada (Domingues & Bermann, 2012). Com o objetivo de observar o comportamento da vegetação, umidade e temperatura nas áreas de desmatamento, foram calculados os índices NDVI e NDMI e a temperatura superficial terrestre a partir das imagens ópticas. O índice NDVI é aplicado para identificar a presença de vegetação e visualizar o seu nível de vigor (Ponzoni *et al.*, 2015). O
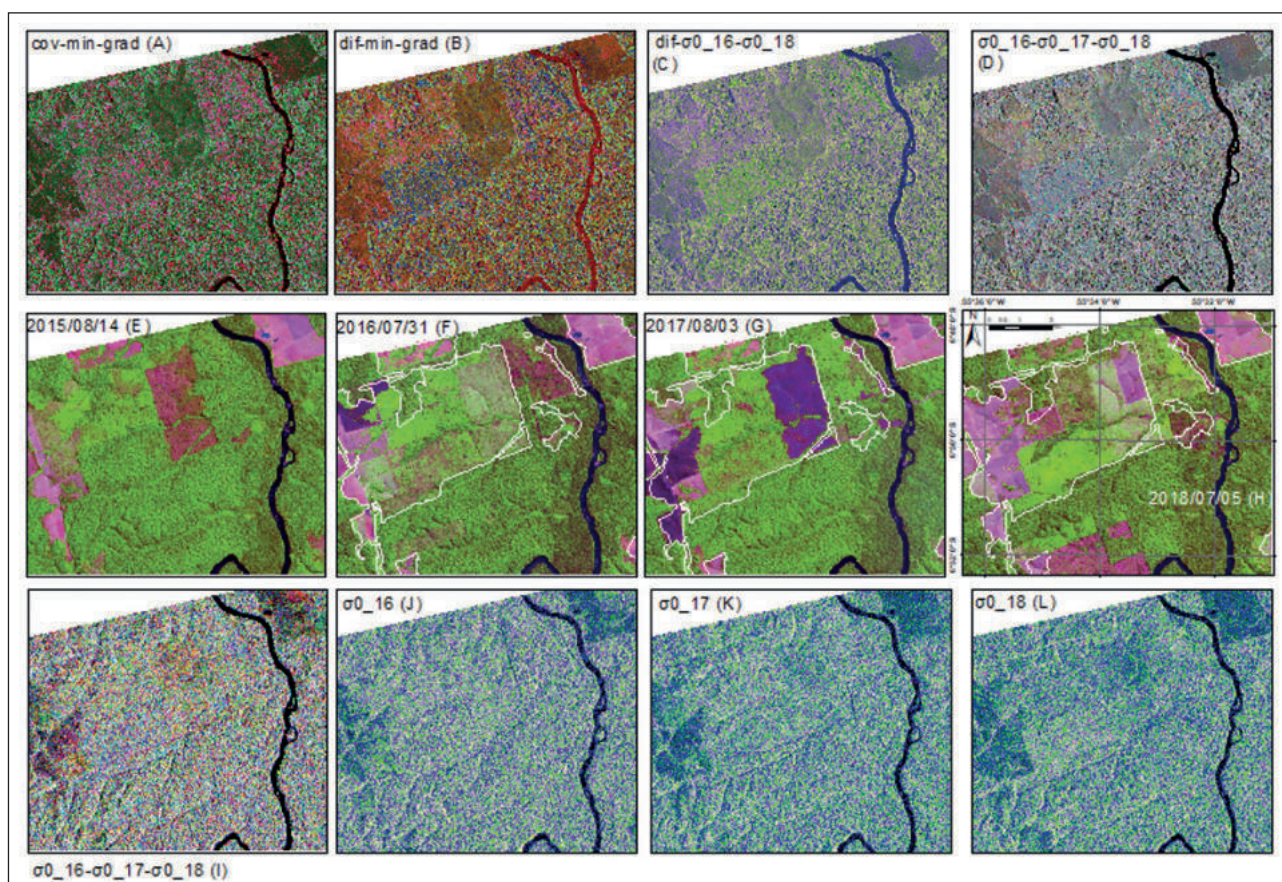

Figura 6 Imagens do COSMO-SkyMed: covariância-mínimo-gradiente (A), diferença σ^0 (2016-2018)-mínimo-gradiente (B), diferença σ^0_(2016-2018)- σ^0_2016 - σ^0_2018 (C) e σ^0_2016- σ^0_2017- σ^0_2018 (D). Composições coloridas RGB/654 do satélite Landsat-8 obtidas em 2015/08/14 (E), 2016/07/31 (F) (com polígonos de desmatamento T0), 2017/08/03 (G) (com polígonos de desmatamento T0 e DETER-B de 2017) e 2018/07/05 (H) (com polígonos de desmatamento T0 e DETER-B de 2018). Imagens do Sentinel-1A: σ^0_2016-σ^0_2017- σ^0_2018 (I) (composição RGB: R = σ^0 VH de 2016; G = σ^0 VH de 2017; e B = σ^0 VH de 2018); σ^0_16 (J) (composição R = σ^0_VV; G = σ^0_VH; e B = diferença VV-VH) para os anos de 2016-01-19, 2017-04-19 (K) e 2018-05-08 (L).

índice NDMI é aplicado com o objetivo de observar a diferença de umidade nas áreas desmatadas e nas áreas de floresta. Esse último também pode auxiliar na identificação da presença de vegetação (Wilson & Sader, 2002).

Após o cálculo do NDVI, foi realizada uma classificação no programa ENVI. Foi utilizada a ferramenta SPEAR, que faz uma delineação da vegetação para permitir identificar a presença de vegetação e visualizar seu nível de vigor. O NDVI gera uma imagem com valores que variam de -1 a +1. Os pixels sem vegetação tendem a -1 enquanto os pixels com vegetação vigorosa tendem a 1. Os valores NDVI foram divididos em quatro classes: áreas não vegetadas (entre -1 a 0,50), vegetação esparsa (acima de 0,50 e abaixo de 0,62), vegetação moderada (acima de 0,62 e abaixo de 0,68) e vegetação densa (entre 0,68 a 1). Os valores foram ajustados visualmente de modo que representassem bem as quatro classes. Para o ano de 2015, os limiares booleanos mínimo e máximo foram de -0,57 e 0,84; em 2016, mínimo de -0,41 e máximo de 0,84; em 2017, mínimo de -0,94 e máximo de 0,86; e em 2018, mínimo de -0,98 e máximo de 0,87. A Figura 7 mostra, em detalhe, para as datas de 2015/08/14, 2016/07/31, 2017/08/03 e 2018/07/05, a classificação do NDVI [(A) a (D)]; imagens RGB-654 usadas como referência [(E) a (H)]; imagens do índice de umidade NDMI [(I) a (L)]; e imagens de temperatura superficial terrestre [(M) a (P)]. Os valores de NDVI variam de -1 a +1, onde os valores mais elevados correspondem a áreas de vegetação fotossinteticamente mais ativas e os valores inferiores representam áreas com baixa vegetação. O NDVI individualizou bem as áreas sem vegetação e vegetação esparsa, porém, as áreas de rebrota e vegetação densa apresentaram o mesmo nível de vigor.

O NDMI também possui valores que variam de -1 a +1, onde os valores mais elevados correspondem às áreas mais úmidas (com presença de vegetação) e os valores menores, às áreas de baixa umidade ou pouca vegetação. Observou-se uma queda da umidade nas áreas desmatadas ou de pouca vegetação. Porém, áreas de rebrota e áreas de vegetação densa apresentaram valores similares e impossibilitaram a individualização dessas

duas classes. A LST foi calculada para observar o comportamento da temperatura nas áreas desmatadas e nas áreas de floresta. Os mapas de temperatura mostraram coerência relativamente alta com os índices de umidade. As regiões com mais alta temperatura apresentaram baixa umidade. Entretanto, as temperaturas nas áreas de rebrota foram levemente mais elevadas que as áreas de floresta densa, permitindo diferenciar visualmente essas duas classes. As áreas de solo exposto alcançaram valores de temperatura de superfície acima de 50 °C.

4 Conclusões

Os dados SAR, em banda X, forneceram informações importantes sobre os atributos temporais e combinações RGB que melhor evidenciaram as áreas de desmatamentos na região. Covariância, gradiente e mínimo foram os parâmetros temporais que melhor evidenciaram os desmatamentos como também o período aproximado de sua ocorrência. Esses parâmetros, quando combinados com dados de retroespalhamento, por exemplo, diferença de σ^0, mínimo e gradiente, permitiram delinear os limites de desmatamento com maior definição quando comparados à combinação pura de parâmetros da análise temporal. As composições de diferenças entre bandas de σ^0 também podem ser usadas para extrair informações de alteração como o período aproximado de ocorrência dos desmatamentos.

Os dados SAR, em banda C, não apresentaram resultados capazes de definir inequivocamente áreas de desmatamento. Esses resultados deram-se, provavelmente, à soma de alguns fatores como o modo de aquisição dos dados em banda C ser *Interferometric Wide*, menos detalhado quando comparado ao modo *StripMap*, das imagens em banda X.

Os índices calculados a partir de imagens ópticas forneceram informações importantes sobre a presença e vitalidade da vegetação nas áreas de desmatamento e de sua relação com as condições de umidade e de temperatura nessas áreas. Os índices NDVI e NDMI mostraram-se correlatos, áreas com vegetação densa a moderada apresentaram umidade elevada e áreas sem vegetação ou vegetação esparsa apresentaram baixa umidade. Porém, pôde-se obser-
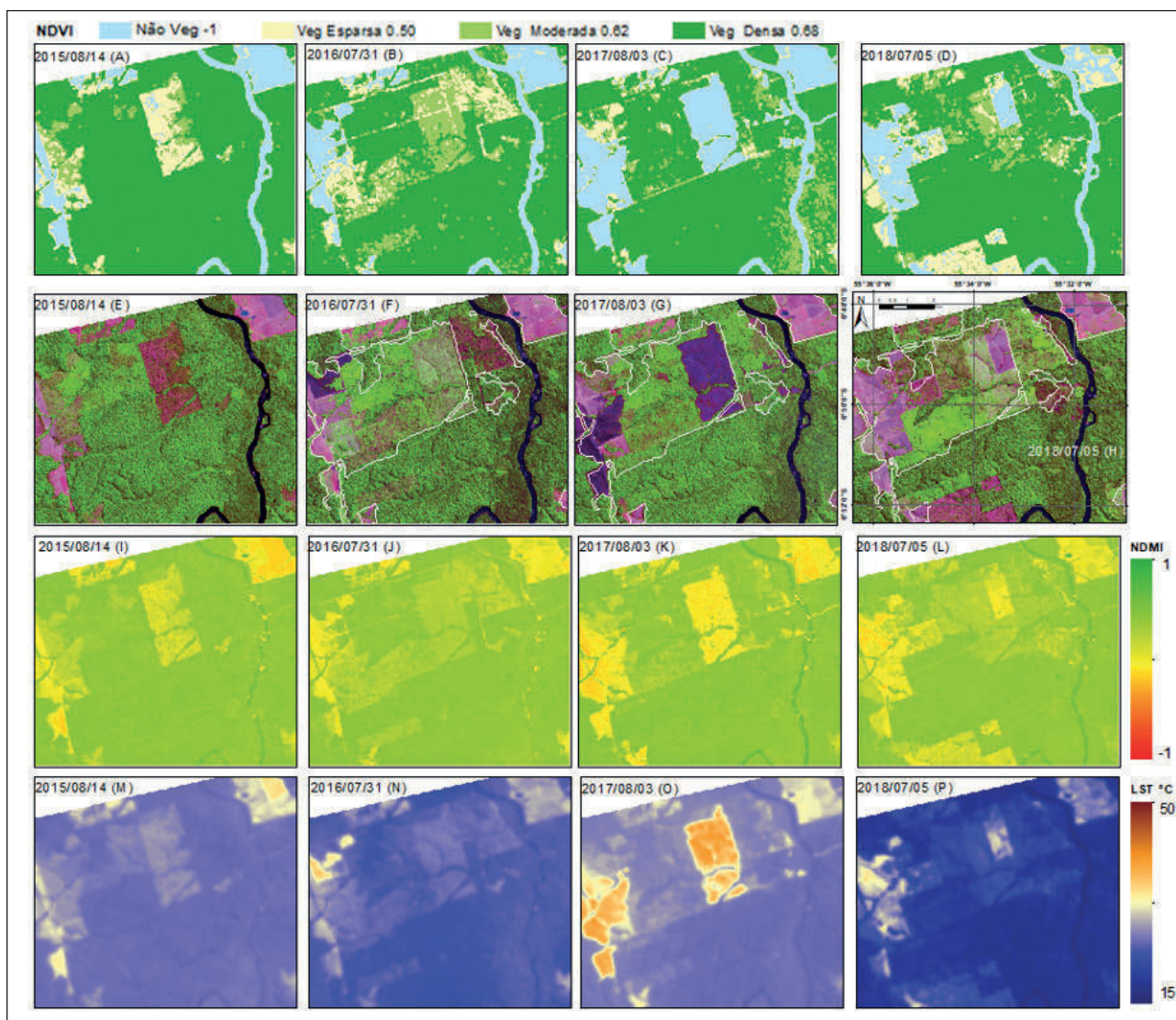
Figura 7 Mapas de classificação do NDVI para 2015-08-14 (A), 2016-07-31 (B), 2017-08-03 (C) e 2018-07-05 (D). Composições coloridas RGB/654 do satélite Landsat-8 obtidas em 2015/08/14 (E), 2016/07/31 (F) (com polígonos de desmatamento T0), 2017/08/03 (G) (com polígonos de desmatamento T0 e DETER-B de 2017) e 2018/07/05 (H) (com polígonos de desmatamento T0 e DETER-B de 2018). Mapas de índices de umidade (NDMI) para 2015-08-14 (I), 2016-07-31 (J), 2017-08-03 (K) e 2018-07-05 (L). Mapas de temperatura superficial terrestre (LST) para 2015-08-14 (M), 2016-07-31 (N), 2017-08-03 (O) e 2018-07-05 (P).

var, pelas imagens ópticas, que, nas áreas que foram desmatadas e posteriormente houve uma rebrota da vegetação, esses dois índices apresentaram valores similares em relação às áreas de vegetação densa, não permitindo uma diferenciação entre essas duas classes. A temperatura superficial terrestre mostrou-se mais sensível que os índices normalizados pela diferença onde foi possível observar uma temperatura levemente maior nas áreas de rebrota e uma

temperatura mais baixa nas áreas de vegetação densa, sendo possível fazer uma separação visual entre essas duas áreas.

A tecnologia SAR mostrou-se útil na identificação dos desmatamentos durante o período de chuvas na Amazônia Legal. Neste estudo, foi relevante avaliar os parâmetros temporais e combinações RGB que melhor ressaltaram as áreas de desmatamentos e seus limites na área de estudo. Em pesquisas futu-

ras, pretende-se realizar análises de textura de dados SAR para uma melhor definição e discriminação das classes vegetais como também análises quantitativas das informações SAR e ópticas.

5 Agradecimentos

Ao Censipam, por ceder as imagens do COS-MO-SkyMed e uma máquina de processamento para a realização do trabalho.

6 Referências

Aboud Neta, S.R.; Freitas, C.C. & Dutra, L.V. 2010. Uso de imagens ALOS/PALSAR multipolarizadas para detecção de incremento de desflorestamento na Amazônia. *Revista Brasileira de Cartografia, 62*(2): 417-431.

Aragão, L.E.O.C.; Poulter, B.; Barlow, J.B.; Anderson, L.O.; Malhi, Y.; Saatchi, S.; Phillips, O.L. & Gloor, E. 2014. Environmental change and the carbon balance of Amazonian forests. *Biological Reviews*, 89(4): 913-931.

Arima, E.Y.; Walker, R.T.; Perz, S.G. & Caldas, M. 2005. Loggers and forest fragmentation: behavioral models of road building in the Amazon basin. *Annals of the Association of American Geographers*, 95(3): 525-541.

Asner, G.P.; Knapp, D.E.; Broadbent, E.N.; Oliveira, P.J.C.; Keller, M. & Silva, J.N. 2005. Selective logging in the Brazilian Amazon. *Science*, 310: 480-482.

Barros, H.S. & Fearnside, P.M. 2016. Soil carbon stock changes due to edge effects in Central Amazon Forest fragments. *Forest Ecology and Management*, 379:30-36.

Barsi, J.; Schott, J.R.; Hook, S.J.; Raqueno, N.G.; Markham, B.L. & Radocinski, R.G. 2014. Landsat-8 Thermal Infrared Sensor (TIRS) vicarious radiometric calibration. *Remote Sensing, 6*: 11607-11626.

Bernhard, G.E.M.; Stein, E.; Twele, A. & Gaehler, M. 2011. Synergistic use of optical and radar data for rapid mapping of forest fires in the European Mediterranean. *In*: ISPRS WORKSHOP, 38(4). Hannover, Germany. 2011. *Proceedings*, p. 14–17.

Broadbent, E.N.; Asner, G.P.; Keller, M.; Knapp, D.E.; Oliveira, P.J.C. & Silva, J.N. 2008. Forest fragmentation and edge effects from deforestation and selective logging in the Brazilian Amazon. *Biological Conservation*, 141(7): 1745-1757.

Bustamante, M.M.C.; Roitman, I.; Aide, T.M.; Alencar, A.; Anderson, L.O.; Aragão, L.; Asner, G.P.; Barlow, J.; Berenguer, E.; Chambers, J.; Costa, M.H.; Fanin, T.; Ferreira, L.G.; Ferreira, J.; Keller, M.; Magnusson, W.E.; Morales-Barquero, L.; Morton, D.; Ometto, J.P.H.B.; Palace, M.; Peres, C.A.; Silvério, D.; Trumbore, S. & Vieira, I.C.G. 2016. Toward an integrated monitoring framework to assess the effects of tropical forest degradation and recovery on carbon stocks and biodiversity. *Global Change Biology*, 22(1): 92-109.

Butt, N.; Oliveira, P.A. & Costa, M.H. 2011. Evidence that deforestation affects the onset of the rainy season in Ron-

dônia, Brazil. *Journal of Geophysical Research Atmospheres*, *116*(11): 2-9.

Capodici, F.; D'Urso, G. & Maltese, A. 2013. Investigating the relationship between X-band SAR data from COSMO-SkyMed satellite and NDVI for LAI detection. *Remote Sensing, 5*(3): 1389–1404.

Carreiras, J.M.B.; Jones, J.; Lucas, R.M. & Shimabukuro, Y.E. 2017. Mapping major land cover types and retrieving the age of secondary forests in the Brazilian Amazon by combining single-date optical and radar remote sensing data. *Remote Sensing of Environment, 194*: 16–32.

Cochrane, M.A. 2003. Fire science for rainforests. *Nature*, *421*(6926): 913-919.

Covello, F.; Battazza, F.; Coletta, A.; Fiorentino, C.; Pietranera, L.; Valentine, G. & Zoffoli, S. 2010. COSMO-SkyMed an existing opportunity for observing the Earth. *Journal of Geodynamics*, *49*(3-4): 171-180.

Davidson, E.A.; Araújo, A.C.; Artaxo, P.; Balch, J.K.; Brown, I.F.; Bustamante, M.M.C.; Coe, M.T.; DeFries, R.S.; Keller, M.; Longo, M.; Munger, W.; Schroeder, W.; Soares-Filho, B.S.; Souza Jr, C.M. & Wofsy, S.C. 2012. The Amazon Basin in transition. *Nature*, *481*(7381): 321-328.

Diniz, C.G.; Souza, A.A.A.; Santos, D.C.; Dias, M.C.; Luz, N.C.; Moraes, D.R.V.; Maia, J.S.; Gomes, A.R.; Narvaes, I.S.; Valeriano, D.M.; Maurano, L.E.P. & Adami, M. 2015. DETER-B: the new Amazon near real-time deforestation detection system. *IEEE Journal of Selected Topics in Applied Earth Observations and Remote Sensing*, *8*(7): 3619-3628.

Domingues, M.S. & Bermann, C. 2012. O arco de desflorestamento na Amazônia: da pecuária à soja. *Ambiente & Sociedade*, *15*(2): 1-22.

Ernhard, E.M.; Twele, A.; Gahler, M. 2011. Rapid mapping of forest fires in the European Mediterranean region – a change detection approach using X-band SAR-data. *Photogrammetrie-Fernerkundung-Geoinformation, 2011*(4): 261-270.

ESA. 2018. *Sentinel online. Missions. Sentinel-1.* Disponível em: <https://sentinels.copernicus.eu/web/sentinel/missions/sentinel-1>. Acesso em: 10 jan. 2018.

Escada, M.I.S.; Maurano, L.E.; Rennó, C.D.; Amaral, S. & Valeriano, D.M. 2011. Avaliação de dados dos sistemas de alerta da Amazônia: DETER e SAD. *In*: SIMPÓSIO BRASILEIRO DE SENSORIAMENTO REMOTO, 15. Curitiba, PR. 2011. *Anais*, São José dos Campos: INPE, p. 2934-2943.

Ferreira, L.G.; Ferreira, N.C. & Ferreira, M.E. 2008. Sensoriamento remoto da vegetação: evolução e estado-da-arte. *Acta Scientiarum. Biological Sciences*, *30*(4): 379-390.

Grecchi, R.C.; Beuchle, R.; Shimabukuro, Y.E.; Aragão, L.E.O.C.; Arai, E.; Simonetti, D. & Achard, F. 2017. An integrated remote sensing and GIS approach for monitoring areas affected by selective logging: A case study in northern Mato Grosso, Brazilian Amazon. *International Journal of Applied Earth Observation and Geoinformation*, *61*: 70-80.

Guenther, C.K.F.; Bufacchi, P.; Santos, J.C.; Veras, C.A.G.; Alvarado, E.C.; Mell, W. & Carvalho Jr, J.A. 2017. Probability of surface fire spread in Brazilian rainforest fuels from outdoor experimental measurements. *European Journal of Forest Research*, *136*(2): 217-232.

Hansen, M.C.; Potapov, P.V.; Moore, R.; Hancher, M.; Turubanova, S.A.; Tyukavina, A.; Thau, D.; Stehman, S.V.; Goetz, S.J.; Loveland, T.R.; Kommareddy, A.; Egorov, A.; Chini, L.; Justice, C.O. & Twnshend, J.R.G. 2013. High-resolution global maps of 21st-century forest cover change. *Science, 342*(6160): 850–853.

Henderson, F.M. & Lewis, A.J. 1998. *Principles of Application of Imaging Radar*. Manual of remote sensing (3ª ed., v. 2). United States.

Hosonuma, N.; Herold, M.; Sy, V.; DeFries, R.S.; Brockhaus, M.; Verchot, L.; Angelsen, A. & Romijn, E. 2012. An assessment of deforestation and forest degradation drivers in developing countries. *Environmental Research Letters,7*(4): 1-12.

INMET. 2019. *BDMEP - Banco de Dados Meteorológicos para Ensino e Pesquisa.* Disponível em: http://www.inmet. gov.br/portal/index.php?r=bdmep/bdmep. Acesso em: 24 de janeiro de 2019.

INPE. 2013. *Metodologia para o cálculo da taxa anual de desmatamento na Amazônia Legal.* São José dos Campos: INPE, p. 1-37.

ISA. 2009. *COSMO-SkyMed SAR Products Handbook*. 105 p.

Jusys, T. 2016. Fundamental causes and spatial heterogeneity of deforestation in Legal Amazon. *Applied Geography*, *75*: 188-199.

Knight, E.J. & Kvaran, G. 2014. Landsat-8 Operational Land Imager: design, characterization and performance. *Remote Sensing*, *6*: 10286-10305.

Knox, R.; Wang, J. & Bras, R. 2011. Precipitation variability over the forest-to-non forest transition in Southwestern Amazonia. *Journal of Climate*, *24*(9): 2368-2377.

Lardeux, C.; Frison, P.L; Tison, C.; Souyris, J.C.; Stoll, B.; Fruneau, B. & Rudant, J.P. 2011. Classification of tropical vegetation using multifrequency partial SAR polarimetry. *IEEE Geoscience and Remote Sensing Letters, 8*(1): 133–137.

Lei, Y.; Treuhaft, R.; Keller, M.; Santos, M.; Gonçalves, F. & Neumann, M. 2018. Quantification of selective logging in tropical forest with spaceborne SAR interferometry. *Remote Sensing of Environment, 211*: 167–183.

Lu, D.; Mausel, P.; Brondizio, E. & Moran, E. 2004. Change detection techniques. *International Journal of Remote Sensing*, *25*(12): 2365-2401.

Martone, M.; Rizzoli, P.; Wecklich, C.; González, C.; Bueso-Bello, J.L.; Valdo, P.; Schulze, D.; Zink, M.; Krieger, G. & Moreira, A. 2018. The global forest/non-forest map from TanDEM-X interferometric SAR data. *Remote Sensing of Environment, 205*: 352–373.

Matricardi, E.A.T.; Skole, D.L.; Pedlowski, M.A.; Chomentowski, W. & Fernandes, L.C. 2010. Assessment of tropical forest degradation by selective logging and fire using Landsat imagery. *Remote Sensing of Environment*, *114*(5): 1117-1129.

Mitchell, A.L.; Rosenqvist, A. & Mora, B. 2017. Current remote sensing approaches to monitoring forest degradation in support of countries: measurement, reporting and verification (MRV) systems for REDD+. *Carbon Balance and Management*, *12*(9): 1-22.

Morton, D.C.; DeFries, R.S.; Shimabukuro, Y.E.; Anderson, L.O.; Arai, E.; Espírito-Santo, F.B.; Freitas, R. & Morisette, J. 2006. Cropland expansion changes deforestation dynamics in the southern Brazilian Amazon. *Proceedings of the National Academy of Sciences*, *103*(39): 14637-14641.

Nepstad, D.; Veríssimo, A.; Alencar, A.; Nobre, C.; Lima, E.; Lefebvre, P.; Schlesinger, P.; Potter, C.; Moutinho, P.; Mendoza, E.; Cochrane, M. & Brooks, V. 1999. Large-scale impoverishment of Amazonian forests by logging and fire. *Nature*, *398*(6727): 505-508.

Nepstad, D.; Carvalho, G.; Barros, A.C.; Alencar, A.; Capobianco, J.P.; Bishop, J.; Moutinho, P.; Lefebvre, P.; Silva Jr., U.L. & Prins, E. 2001. Road paving, fire regime feedbacks, and the future of Amazon forests. *Forest Ecology and Management*, *154*(3): 395-407.

Ponzoni, F.J.; Shimabukuro, Y.E. & Kuplich, T.M. 2015. A imagem como fonte de dados radiométricos (abordagem quantitativa). *In*: SENSORIAMENTO REMOTO DA VEGETAÇÃO. (2ª ed.). Editora Parêntese, p. 78-115.

Reiche, J.; Verbesselt, J.; Hoekman, D. & Herold, M. 2015. Fusing Landsat and SAR time series to detect deforestation in the tropics. *Remote Sensing of Environment, 156*: 276–293.

Shimabukuro, Y.E.; Miettinen, J.; Beuchle, R.; Grecchi, R.C.; Simonetti, D. & Achard, F. 2015. Estimating burned area in Mato Grosso, Brazil, using an object-based classification method on a systematic sample of medium resolution satellite images. *IEEE Journal of Selected Topics in Applied Earth Observations and Remote Sensing*, *8*(9): 4502–4508.

Soares-Filho, B.S.; Nepstad, D.C.; Curran, L.M.; Cerqueira, G.C.; Garcia, R.A.; Ramos, C.A.; Voll, E.; McDonald, A.; Lefebvre, P. & Schlesinger, P. 2006. Modelling conservation in the Amazon basin. *Nature*, *440*(7083): 520-523.

Souza, C.M.; Siqueira, J.V.; Sales, M.H.; Fonseca, A.V.; Ribeiro, J.G.; Numata, I.; Cochrane, M.A.; Barber, C.P.; Roberts, D.A. & Barlow, J. 2013. Ten-year Landsat classification of deforestation and forest degradation in the Brazilian Amazon. *Remote Sensing*, *5*(11): 5493-5513.

Souza, G.M.G.; Escada, M.I.S. & Capanema, V.P. 2017. Cicatrizes de queimadas e padrões de mudanças de uso e cobertura da terra no sudoeste do estado do Pará, Brasil. *In*: SIMPÓSIO BRASILEIRO DE SENSORIAMENTO REMOTO, 8. Santos, SP. 2017. *Anais*. São José dos Campos: INPE, p. 5760-5767.

Thompson, G.; Thompson, I.D.; Guariguata, M.R.; Okabe, K.; Bahamondez, C.; Nasi, R.; Heymell, V. & Sabogal, C. 2013. An operational framework for defining and monitoring forest degradation. *Ecology and Society, 18*(2): 20.

Torres, R.; Snoeij, P.; Geudtner, D.; Bibby, D.; Davidson, M.; Attema, E.; Potin, P.; Rommen, B.; Floury, N.; Brown, M.; Traver, I.N.; Deghaye, P.; Duesmann, B.; Rosich, B.; Miranda, N.; Bruno, C.; L'Abbate, M.; Croci, R.; Pietropaolo, A.; Huchler, M. & Rostan, F. 2012. GMES Sentinel-1 mission. *Remote Sensing of Environment*, *120*: 9-24.

Wilson, E.H. & Sader, S.A. 2002. Detection of forest harvest type using multiple dates of Landsat TM imagery. *Remote Sensing of Environment*, *80*(3): 385-396.

Article

Fire Occurrences and Greenhouse Gas Emissions from Deforestation in the Brazilian Amazon

Claudia Arantes Silva [1,*] **, Giancarlo Santilli** [2] **, Edson Eyji Sano** [3] **and Giovanni Laneve** [4]

1   Departamento de Geologia Geral, Instituto de Geociências, Universidade de Brasília (UnB),
    Brasília 70297-400, Brazil
2   Faculdade do Gama, Universidade de Brasília (UnB), Brasília 72444-240, Brazil; santilli@aerospace.unb.br
3   Embrapa Cerrados, Planaltina 73301-970, Brazil; edson.sano@embrapa.br
4   Scuola di Ingegneria Aerospaziale, Sapienza University of Rome, 00138 Roma, Italy;
    giovanni.laneve@uniroma1.it
*   Correspondence: claudia.arantes@aluno.unb.br

Abstract: This work presents the dynamics of fire occurrences, greenhouse gas (GHG) emissions, forest clearing, and degradation in the Brazilian Amazon during the period 2006–2019, which includes the approval of the new Brazilian Forest Code in 2012. The study was carried out in the Brazilian Amazon, Pará State, and the municipality of Novo Progresso (Pará State). The analysis was based on deforestation and fire hotspot datasets issued by the Brazilian Institute for Space Research (INPE), which is produced based on optical and thermal sensors onboard different satellites. Deforestation data was also used to assess GHG emissions from the slash-and-burn practices. The work showed a good correlation between the occurrence of fires in the newly deforested area in the municipality of Novo Progresso and the slash-and-burn practices. The same trend was observed in the Pará State, suggesting a common practice along the deforestation arch. The study indicated positive coefficients of determination of 0.72 and 0.66 between deforestation and fire occurrences for the municipality of Novo Progresso and Pará State, respectively. The increased number of fire occurrences in the primary forest suggests possible ecosystem degradation. Deforestation reported for 2019 surpassed 10,000 km^2, which is 48% higher than the previous ten years, with an average of 6760 km^2. The steady increase of deforestation in the Brazilian Amazon after 2012 has been a worldwide concern because of the forest loss itself as well as the massive GHG emitted in the Brazilian Amazon. We estimated 295 million tons of net CO_2, which is equivalent to 16.4% of the combined emissions of CO_2 and CH_4 emitted by Brazil in 2019. The correlation of deforestation and fire occurrences reported from satellite images confirmed the slash-and-burn practice and the secondary effect of deforestation, i.e., degradation of primary forest surrounding the deforested areas. Hotspots' location was deemed to be an important tool to verify forest degradation. The incidence of hotspots in forest area is from 5% to 20% of newly slashed-and-burned areas, which confirms the strong impact of deforestation on ecosystem degradation due to fire occurrences over the Brazilian Amazon.

Keywords: Amazon rainforest; forestry degradation; greenhouse gas emission; remote sensing application

1. Introduction

Global efforts have been made to preserve Earth's ecosystems and to mitigate climate changes, including reductions of deforestation and forest degradation [1,2]. The Brazilian Amazon is one of the most endangered ecosystems. A deep understanding of this ecosystem, including its carbon cycle, is essential to know the adaptability of the environment to climate changes [3]. The Brazilian Amazon, with about 5.2 million km^2, covers the states of Acre (AC), Amapá (AP), Amazonas (AM), Maranhão (MA), Mato Grosso (MT), Pará (PA), Rondônia (RO), Roraima (RR), and Tocantins (TO), and occupies about 60% of the Brazilian territory (Figure 1A). Human occupation in this region has claimed large areas of the original forest for settlement, beef production, crop plantation, and hydropower

generation [4–12], especially in a region known as the deforestation arch. This arch-shaped region is located in the southernmost part of the Brazilian Amazon and shows the highest occurrence of forest clearings [13] and occupation [14,15]. It covers about 1.71 million km^2, i.e., 33% of the Brazilian Amazon. This region stretches from the southeast of Pará State to the east of Acre State, concentrating 77% of total deforestation of the Brazilian Amazon, mostly for soybean plantation and cattle ranching [5,15,16]. Figure 1B shows the annual deforestation over the Pará State and the Brazilian Amazon, as estimated by the National Institute for Space Research (INPE), from 1988 to 2019. This institution defines deforestation as the clear-cut conversion of the primary forest by human activities, detected by the Earth Observation satellite optical sensors [13].
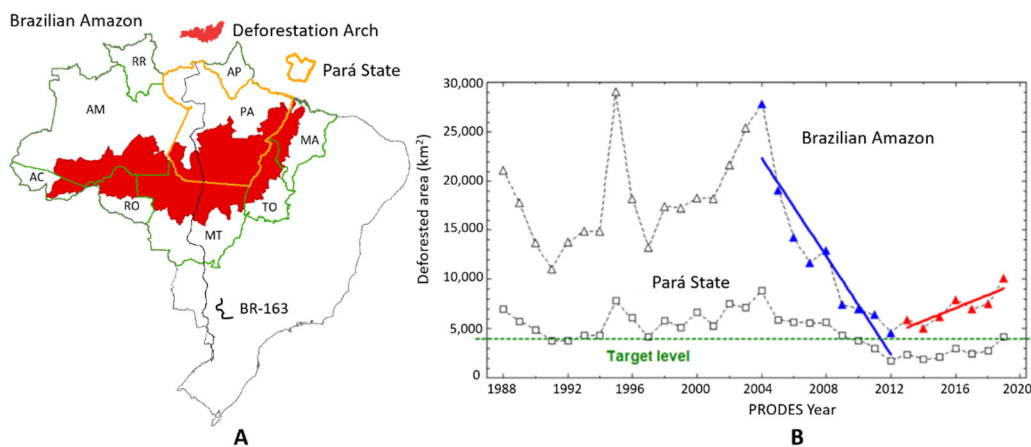

Figure 1. (**A**) Location of the deforestation arch in the Brazilian Amazon. (**B**) Annual deforestation area in the Brazilian Amazon (triangle) and in the Pará State (square), according to the Monitoring Deforestation of the Brazilian Amazon Forest by Satellite (PRODES) project, coordinated by the National Institute for Space Research (INPE). State identification: AC = Acre; AM = Amazonas; AP = Amapá; MA = Maranhão; MT = Mato Grosso; PA = Pará; RO = Rondônia; RR = Roraima; TO = Tocantins.

Since 2006, the highest levels of deforestation in the Brazilian Amazon are found in the Pará State, reaching about 5000 km^2 in 2019. It can also be seen in Figure 1B that the deforestation trend in the Pará is similar to that of the entire Brazilian Amazon. In this state, forest disturbances are located mainly in the south, southwest, and east borders, covering approximately 550,000 km^2. The largest annual deforestation in the Brazilian Amazon occurred in 1995, surpassing 29,000 km^2. A second peak occurred in the period 2002–2004, with an average of 24,939 km^2. From 2004 to 2012, there was a sharp decrease in annual deforestation rates, as indicated by the blue line in Figure 1B (correlation higher than 80%). Voluntary "Reducing Emission from deforestation and forest Degradation in Developing countries" (REDD+) projects for the region started in 2008 [17]. By this time, Brazil was close to reaching the goal of reducing deforestation by 80% until 2020 (green, dashed line in Figure 1B) compared to the 1996–2005 period. This goal was set in 2009 during the United Nations Framework Convention on Climate Change (UNFCCC) held in Copenhagen, Denmark [18]. The trend, however, inverted, as indicated by the steady growth of the red line in Figure 1B. The inflexion is linked to the Federal Law n. 12.727/2012 [19] that, to some extent, relaxed forest conservation. As of 2019, deforestation in Pará State alone was higher than the target value set in 2009 for the whole Brazilian Amazon.

Figure 2 shows the relationship between land use and land cover changes, and forest fire in the Brazilian Amazon, as proposed in References [5,6]. Road construction facilitates forest access, accelerating deforestation and selective logging, and lowering the resilience of surrounding forests to fire [20–23]. Deforestation raises the number of forest edges, increasing the susceptibility of forests to fires [24–27]. Selective logging degrades forest, reduces canopy and soil moisture, and increases canopy temperature and tree mortality, intensifying fire outbreaks [22,28,29]. The cycle grows in a spiral configuration: forest fires and smoke emissions reduce rainfall, particularly in the dry season [24,30–35], previously burned areas are more

prone to recurrence, changes in the global and local climate, along with land use intensification, contribute to increasing the level of forest degradation [28,35–41], most significant changes in forest canopy density take place in regions close to the forest edges [16,22,35,42], and land management fires can penetrate the standing degraded forests, as demonstrated by others studies [21,43,44].
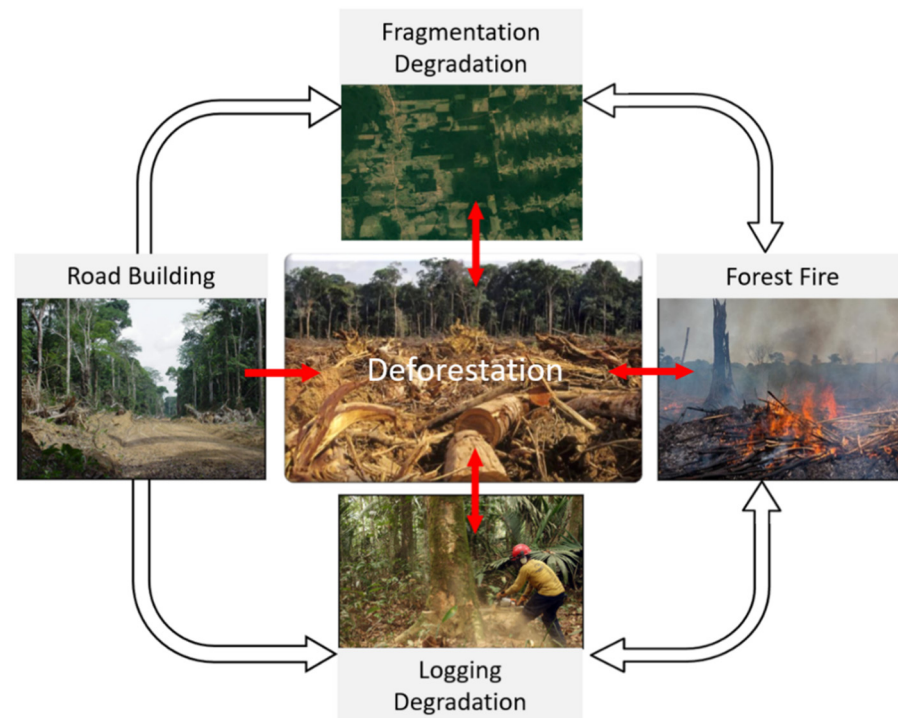

Figure 2. Relationship between land use and land cover changes and fire occurrences. Sources: References [5,6].

Several in-situ measurements of the slash-and-burn forest clearing practices have been conducted to infer greenhouse gas (GHG) emission [45–49]. Figure 3 shows the main steps of the slash-and-burn practices observed in the Brazilian Amazon. By the end of the rainy season, the forest is clear-cut (Figure 3A) and left in the terrain to dry until the peak of the dry season (Figure 3B), after which the fire is set. The burning period typically extends from July to October. The initial fire consumes the duff-layer, small branches, and leaves, while most of the massive trunks remain in the terrain (Figure 3C). Finally, the remaining scorched logs are stockpiled and burned along the coming years until the terrain becomes dominantly bare soil (Figure 3D). Fire may penetrate the standing forest if moisture favors flame propagation through the understory vegetation [42–44]. Forest degradation increases after successive fires, observed by the combustion of growing small trees in dry seasons. The less resilient forest also favors significant fire recurrences over the years. Fire is used mainly for land management, mostly for clearing the terrain after the slash-and-burn deforestation for subsequent maintenance of deforested areas [50,51].

GHG emissions from deforestation in the Brazilian Amazon are also of great concern, considering that it generally accounts for more than 200 t ha^{-1} of CO_2 after the clear-cut occupation [44,49,52]. These authors also observed that other gases such as CO, CH_4, and non-methane hydrocarbons and particulates are also emitted in large quantities.
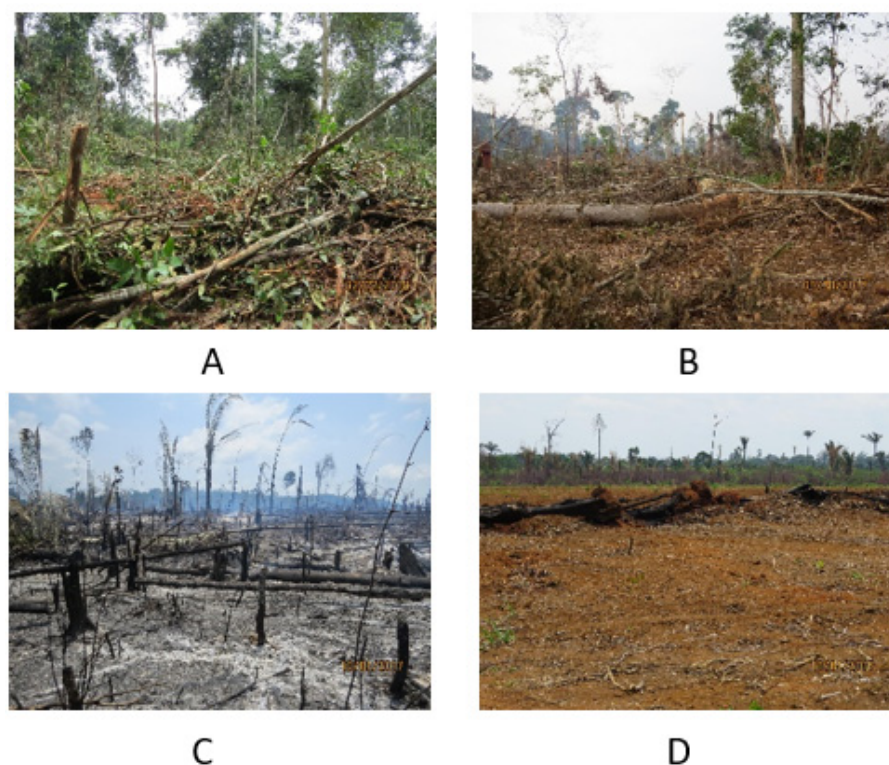
Figure 3. Main stages of the clear-cut processes of forest clearing in the Brazilian Amazon. (**A**) Clear-cut during the wet season or end of the wet season, (**B**) trunks and branches left in the terrain for drying, (**C**) burning activity during the dry season, and (**D**) bare soil prepared for pasture or crop plantation (Photos: E. Sano).

This paper addresses the relationship between forest loss, fire occurrence, forest degradation, and primary GHG emissions over the Brazilian Amazon and downscaling to the Pará State and Novo Progresso municipality. Several authors studied carbon emissions from fires in the Brazilian Amazon, emphasizing specific topics such as drought-related fires rather than forest-clearing-related fires [35] or in specific regions such as the states of Rondônia and Mato Grosso [53]. Aragão and Shimabukuro [37] reported an increase of fire occurrences in areas experiencing reduced deforestation. The literature review showed that there is no previous study relating the amount of fire occurrences in standing forest (degradation) due to deforestation following the slash-and-burn practices over the region. We relied on annual reports published by INPE, for the period 2006–2019. The data were used to correlate fire events in a specific area (Novo Progresso municipality) and in a regional area (Pará State), both located in the deforestation arch. Fire outbreaks inside the primary forest were also investigated to assess ecosystem degradation. The work also presents the amount of GHG originated by the first forest clearing process along the Brazilian rainforest in 2019. The period of 2007–2019 was selected for this study, as it has sharp decay on deforestation rates followed by the steady growth of human occupation after 2012, as depicted in Figure 1.

2. Materials and Methods

2.1. Novo Progresso Region

Pará State encompasses an area of 1,246,000 km^2, equivalent to the total area occupied by Germany, France, the United Kingdom, and Italy, altogether. The Novo Progresso region, located in the southwest of the Pará State (Figure 4), covers 36,800 km^2 and is one of the areas in this state facing long-time, largest clear-cutting deforestation. Most of the deforestation in the Novo Progresso region is found along the BR-163 highway, crossing the region in the North–South direction. Land cover change mapping and monitoring of

this municipality has been a big concern in the literature [54–56]. Within this context, we analyzed our data by considering them in three different scales: municipality, state, and region levels, in order to check the consistency among these scales.
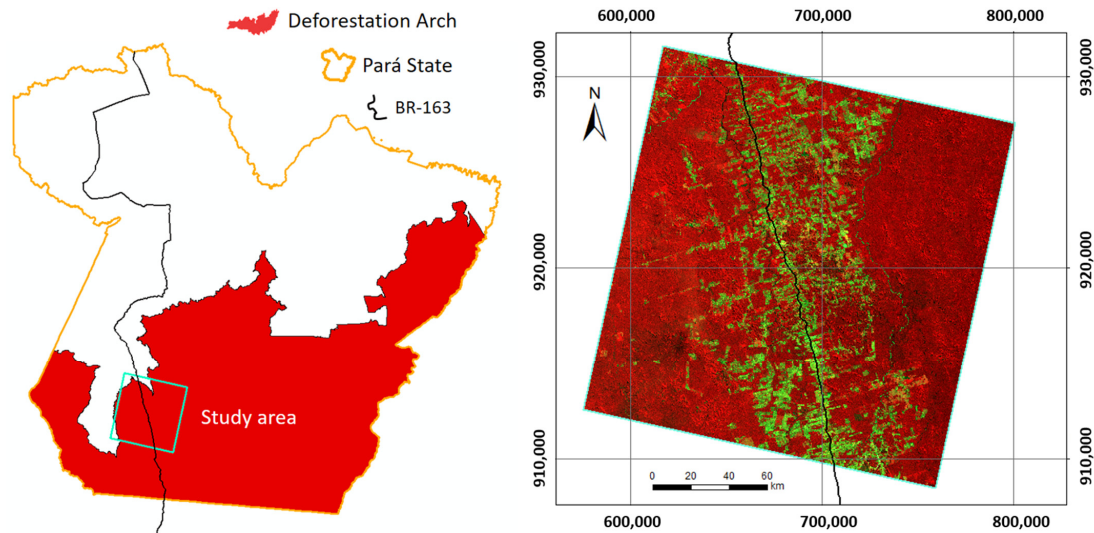

Figure 4. Location of the Novo Progresso region, southwest of the Pará State. Red-Green-Blue (RGB) false-color composite of bands 5, 4, and 3 of Landsat 8 satellite images [57].

2.2. Datasets

The datasets of deforestation and fire hotspots were produced by the INPE's Amazon Deforestation Satellite Monitoring Program (PRODES) and the Forest Fire Program (*Programa Queimadas*), respectively. PRODES provides the annual rates of clear-cut deforested areas larger than 6.25 hectares over the Brazilian Amazon [58]. The system makes use of moderate spatial resolution (10–100 m) optical data, mostly from the dry season, obtained by Landsat 8 (30 m spatial resolution and 16-day revisit time), China–Brazil Earth Resources Satellite (CBERS-4) (20 m spatial resolution and 26-day revisit time), and Sentinel-2 (10 m spatial resolution and 5-day revisit time) satellites. The near real-time fire detection data, provided by the Forest Fire Program [59], are based on thermal sensors onboard several sun-synchronous and geostationary satellites, namely:

- MODerate Resolution Imaging Spectroradiometer (MODIS) sensor onboard Aqua and Terra platforms.
- Advanced Very High-Resolution Radiometer (AVHRR) sensor onboard National Oceanic and Atmospheric Administration (NOAA) satellite.
- AVHRR-3 and Infrared Atmospheric Sounder Interferometer (IASI) sensors onboard Meteorological Operational (MetOp) satellite.
- Visible Infrared Imaging Radiometer Suite (VIIRS) sensor onboard Suomi National Polar-orbiting Partnership (NPP) satellite.
- Advanced Baseline Imager (ABI) sensor, onboard GOES-R satellite.
- Spinning Enhanced Visible and Infrared Imager (SEVIRI) sensor onboard Meteosat Second Generation (MSG) satellite.

Daily fire hotspot monitoring is performed by the MODIS sensor (Collection 6) [59–61]. The detection of fire hotspots by INPE through satellite images is carried out using well-known techniques [62–64], basically by subtracting brightness temperatures measured in the middle infrared (MIR) band (around 4 μm) with that of the measured thermal infrared (TIR) band (around 11 μm). Thermal anomalies are identified when the difference in the brightness temperature measured in these two spectral bands is higher than a given threshold, i.e., when the temperature from MIR is much higher than that of TIR. Hantson et al. [65] investigated the strengths and weaknesses of hotspots detected by MODIS to characterize

fire occurrence in many different ecosystems. For the Brazilian Amazon, they reported less than 2.1% of commissioning error, and 80% confidence interval between hotspot detection (MODIS) and burned area (Landsat). The coefficient of determination between the annual number of hotspots and burned areas for the Amazon was $R^2 = 0.95$.

2.3. Methodology

2.3.1. Deforestation and Fire Hotspots

In the southwest region of Pará State, the typical rainy season is from November to May and the typical dry season is from June to October [66]. INPE´s deforestation mapping starts on 1 August of the previous year until 31 July of the current year. In this paper, this period is referred to as PY (PRODES Year). In PRODES, the processing time is quite long to account for the required level of confidence (>90%) and the size of the region (deforestation arch). Deforestation reports are generally published about four months after the end of the mapping period.

Fire occurrences within the forest and deforested areas were covered for the same reference period (2007–2019) to evaluate their strength of relationship with deforestation. To avoid misinterpretations, the reference year for the hotspots follows that of deforestation. Most planned fires, however, take place in the mid/end of the dry season (August–September) for higher combustion efficiency. The first fires consume about 50% of the recently slashed biomass. The scorched biomass is then stockpiled and burnt in the following years to complete the land clearing process. The newly deforested areas reported for a given PY show intense fire activities in the first months of PY+1 (August–September), but fire hotspots are likely to appear at that pre-burnt area for the next PRODES years (PY+2, PY+3, PY+4, and so on), though at lesser intensity when compared to the first burn. Throughout the work, fire scars, hotspots, and fire outbreaks are mentioned indiscriminately and are considered as indicative of the spatial and temporal burned areas.

Figure 5 illustrates, for a given year, the accumulative location of detected fire hotspots inside the forest shown as red dots, and in the deforested areas, indicated by blue dots. Hotspots' location accuracy is ±500 m. Due to positioning uncertainty, the fire hotspots reported at a distance higher than 500 meters (buffer zone) from the edge of deforested areas were considered to take place at the standing forest. The boundaries of deforested areas were updated annually. Therefore, the buffer zone of 500 m was updated accordingly. Figure 5 shows the consolidated data of forest and non-forest areas as reported by INPE, corresponding to the actual status of the region by 31 July 2019 (PY2018–2019). The hotspots in Figure 5 give the location of their incidences at any time during the period of 1 August 2018 to 31 July 2019. Most of the fire hotspots would appear in the dry season of 2018, from July to October, for which clear-cut had occurred at the first quarter of 2018 (PY2017–2018).
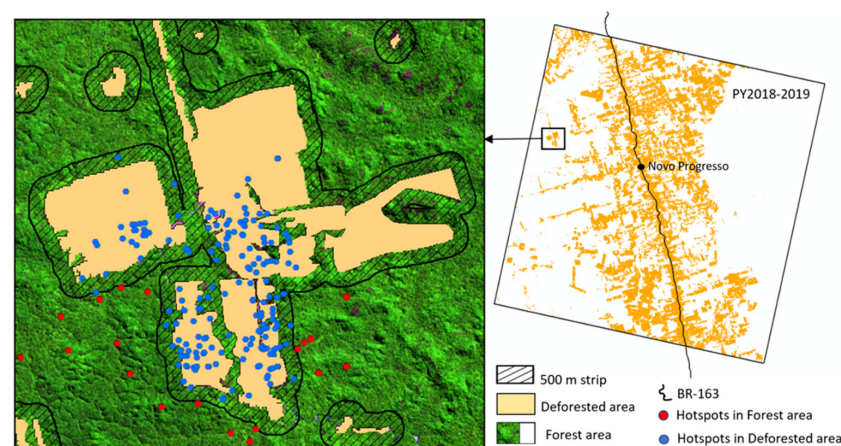

Figure 5. Examples of deforested areas (yellow and striped polygons), forest (green and white areas), fire hotspots in the forest areas (red dots), fire hotspots in the deforested areas (blue dots), and deforestation dynamics example (dotted square) in the Novo Progresso region.

It is important to highlight that the healthy undisturbed forest does not sustain large fires in the Brazilian Amazon, due to the high levels of humidity, even in the dry season. Fire occurrences in the humid tropical forest are observed in dead trees and along the duff-layer. The understory vegetation may propagate flame in the surroundings of large cleared areas (degraded edges of forests) in combination with an intense dry season. Flame propagation through the understory vegetation is too weak to be captured by satellite sensors. Therefore, the fire hotspots inside the intact forest may be due to the flaming of large naturally dead trees or along an open forest trail where small slashed trees have the ability to sustain the fire. Selective logging also degrades the area around the large falling trees, thus making the vicinity prone to propagate flame. Fire occurrences inside the standing forest are restricted to degraded forest caused by any of the previously discussed events or their combined effects.

This study deals with deforestation and the use of fire for land clearing. Fire hotspots may also occur in nearby degraded areas, such as dead trees, near extracted logs and trails. Total GHG emission for the Amazon was limited to the burning of the newly deforested area corrected by the average regrowth of secondary forest throughout.

2.3.2. Greenhouse Gas Emissions

Amazon GHG emissions from slash-and-burn practices can be estimated based on in-situ measurements of forest clearing fire experiments [50,52]. Figure 6 explains the GHG estimation model. Emissions are calculated based on the amount of burned dry biomass, combustion efficiency, and the emission factors for each gas. The dry weight of biomass (ton) is estimated from the local fresh biomass (ton ha^{-1}), its humidity (%), and the amount of deforested area (ha). For the Novo Progresso region, we used the data obtained [52] from two different sites in the Alta Floresta municipality, which is less than 500 km from the Novo Progresso region. For the Pará State, the fresh biomass was calculated by averaging the estimates from Alta Floresta, Mato Grosso State, and Manaus, Amazonas State [46,50,52]. For the Brazilian Amazon, the average fresh biomass included the values from the Pará State and from the municipalities of Cruzeiro do Sul and Rio Branco, both in Acre State. More detailed information about the methodology of the GHG emissions and estimates can be found in Carvalho Jr. et al. [50] and Soares Neto et al. [52].
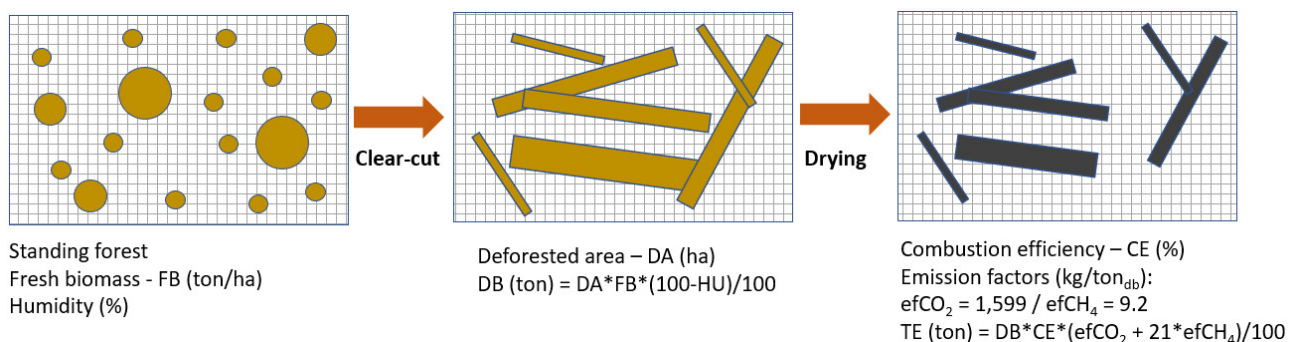

Figure 6. Procedure of the estimation of the greenhouse gas (GHG) emission. HU = humidity; DB = dry biomass, TE = total emission.

Soares Neto et al. [52] reported combustion efficiencies of about 50% and fresh biomass humidity of 42%, prior to clear-cut. Table 1 summarizes the relevant data for emission estimates from slash-and-burn activities in the Brazilian Amazon rainforest.

Table 1. Basic data for gas emissions estimate. Source: References [50,52].

Parameter	Reference Value	Reference Area
Fresh biomass (ton ha^{-1})	512	Novo Progresso
Fresh biomass (ton ha^{-1})	570	Pará State
Fresh biomass (ton ha^{-1})	580	Brazilian Amazon
Emission factor CH_4 (kg ton^{-1} (db)) *	9.2	Brazilian Amazon
Emission factor CO (kg ton^{-1} (db))	111.3	Brazilian Amazon
Emission factor CO_2 (kg ton^{-1} (db))	1599	Brazilian Amazon
Emission factor NMHC (kg ton^{-1} (db))	5.57	Brazilian Amazon
Emission factor $PM_{2.5}$ (kg ton^{-1} (db))	4.84	Brazilian Amazon
Fresh biomass humidity (%)	42	Brazilian Amazon
Combustion efficiency (%)	50	Brazilian Amazon

* db refers to mass of dry biomass burned. NMHC = non-methane hydrocarbon; PM = particulate matter.

3. Results and Discussion

3.1. Fire Hotspots in the Novo Progresso Region

Table 2 reports the statistics about the fire hotspot occurrences inside the deforested and forest areas in the Novo Progresso region. We found a total of 11,769 fire hotspots in PY2006–2007, with 9702 located in deforested areas (corresponding to 5230.90 km^2) and 2067 in forest areas (corresponding to an area of 31,574.50 km^2). In PY2018–2019, the total fire outbreaks detected from 1 August 2018 to 31 July 2019 was 39,384, from which 37,236 over 8481.80 km^2 of deforested area, and 2148 over 28,323.70 km^2 of intact forest.

Table 2. Total annual fire hotspots distribution in the Novo Progresso region. Deforested and forest areas and fire hotspots are reported from PY2006–2007 until PY2018–2019 in the Novo Progresso region. PY = PRODES year.

PY	Forest Area (km^2)	Accumulated Deforested Area (km^2)	Annual Deforested Area (km^2)	Fire Hotspots in Forest	Fire Hotspots in Deforested Area
2006–2007	31,574.5	5230.9		2067	9702
2007–2008	31,153.6	5651.9	421.0	2012	9870
2008–2009	30,543.9	6261.5	609.6	1345	7753
2009–2010	30,406.7	6398.7	137.2	1035	5060
2010–2011	30,281.5	6524.0	125.3	1675	9573
2011–2012	30,096.5	6708.9	184.9	572	3621
2012–2013	29,704.1	7101.3	392.4	4536	36,350
2013–2014	29,437.9	7367.6	266.3	457	10,186
2014–2015	29,200.6	7604.8	237.3	3243	34,817
2015–2016	29,021.9	7783.5	178.7	2085	32,196
2016–2017	28,938.4	7867.1	83.6	1212	19,572
2017–2018	28,655.2	8150.3	283.2	4338	42,723
2018–2019	28,323.7	8481.8	331.5	2148	37,236

Figure 7 shows the variation of total fire outbreaks relative to PY2006–2007 and accumulated deforestation in the Novo Progresso region. From PY2006–2007 to PY2018–2019, deforested areas increased by 8.8%, with a positive correlation of 0.72 with total detected fire hotspots for the same area. The variation of hotspots was stable from PY2006–2007 to PY2011–2012 and increased from PY2012–2013 to PY2018–2019. Deforested areas increased from 4.0% of the period PY2006–2007 to PY2011–2012 to 4.8% of the period PY2012–2013 to PY2018–2019. The average of fire outbreaks was 9047 against 33,014 from PY2012–2013 to PY2018–2019, a three-fold increase.

In this study, deforestation, fire hotspot, and GHG emission data for the period 2007–2019 were analyzed at the levels of municipality, state, and region. In the Novo Progresso municipality, both deforestation and fire hotspots increased over time, though fire hotspots' increase was not so consistent as deforestation over the period considered. Several

studies indicate that, in tropical forests, deforestation and land management practices by using fire are strongly linked [4–12]. In the research conducted in Reference [67] in the Novo Progresso region, more than 70% of fire events detected from MODIS time series for the period 2000–2014 occurred over deforested areas. The sharp increase of fire hotspots found in the period from PY2012–2013 to PY2018–2019 may be related to the current Brazilian Forest Code [19]. This law states that farmers located in the Brazilian Amazon need to maintain 80% of their land with native vegetation if located in forestlands or 30% if located in non-forestlands. However, the law amnestied 58% of the required restoration areas deforested illegally before 2008 [68]. Therefore, the increase in total fire hotspots from 2013 may be associated with the relaxation from the prevailing law.
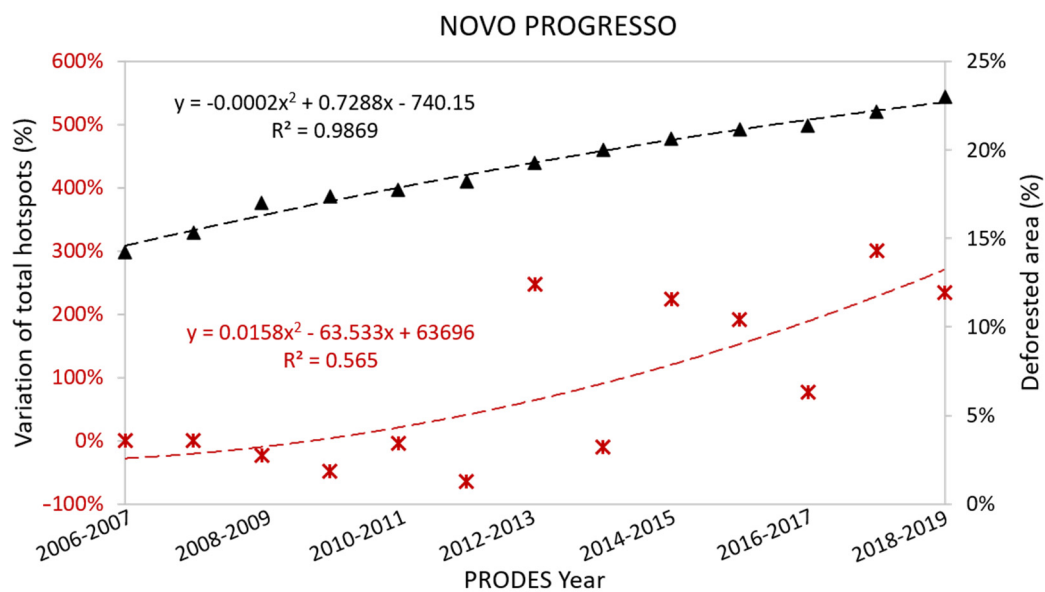

NOVO PROGRESSO

$y = -0.0002x^2 + 0.7288x - 740.15$
$R^2 = 0.9869$

$y = 0.0158x^2 - 63.533x + 63696$
$R^2 = 0.565$

Figure 7. Variation of the total fire hotspots (red) relative to the year PY2006–2007 and accumulated deforestation area (black) in the Novo Progresso region.

Figure 8 exemplifies the dynamics of deforestation occurred in the Novo Progresso region. The deforestation dynamics over the period under investigation are shown in yellow. We can see that the deforested area shown in the bottom and right corner in the PY2012–2013 (area A, Figure 8) was subjected to intense fire activity. The clear-cut process and fire occurred in the same PRODES year of 2012–2013. A significant number of fire outbreaks were detected in PY2012–2013, PY2013–2014, and PY2014–2015. Conversely, fewer hotspots were detected in PY2016–2017 and PY2018–2019, indicating that the area was almost free of original forest residues after PY2016–2017.

The fire hotspots over recently deforested areas (clear-cut) are man-induced, as a rapid and cheap means to clear the area (slash-and-burn) that can be observed by comparing Figure 3B,C. Eventually, the fire set to clean a given deforested area may propagate fire on a nearby pasture, or on some crop area or even through the understory of a standing forest, by accident. Fire occurrences inside consolidated occupied areas may suggest land management, as shown in the large-deforested area in PY2012–2013 (area B, Figure 8). For this area, the high density of hotspots was detected in PY2015–2016 and decayed in the following two years. The high concentration of fire outbreaks in deforested areas is caused by either the combustion of old pre-carbonized trunks that were not burned in the previous years or due to the burning of pasture, caused by an advance of the fire front from the deforested area or even land management.

Fire intensity increased sharply thereafter, as it can be seen in PY2017–2018 (area C, Figure 8). Burning activities were also observed in PY2018–2019, though with less intensity. The slash-and-burn approach for clearing the forest is even more evident by observing PY2018–2019 in Figure 8. The strong overlapping of deforestation and fire occurrences,

shown by the large concentration of hotspots, indicates that the clear-cut took place after 31 July 2018, and the slashed biomass was most likely burnt during the dry season of the same year (2018). The method seemed different from the previous years since forest clearing usually takes place in the rainy season, i.e., in the first quarter of PY, and the fire activity starts in the third quarter of the same year but is reported as PY+1. Such forest clearing processes, also reported by different researchers [5,6,8,11,12,27], confirm the cycle depicted in Figure 2. It begins with the extraction of high commercial value trees (selective logging), followed by the removal of smaller trees and by the clear-cutting of remaining trees and shrubs, producing deforestation in the middle of the forest. Regarding the large-scorched trunks, the clearing process may extend for about five to six years until the remaining logs that were stockpiled had been combusted to completion.
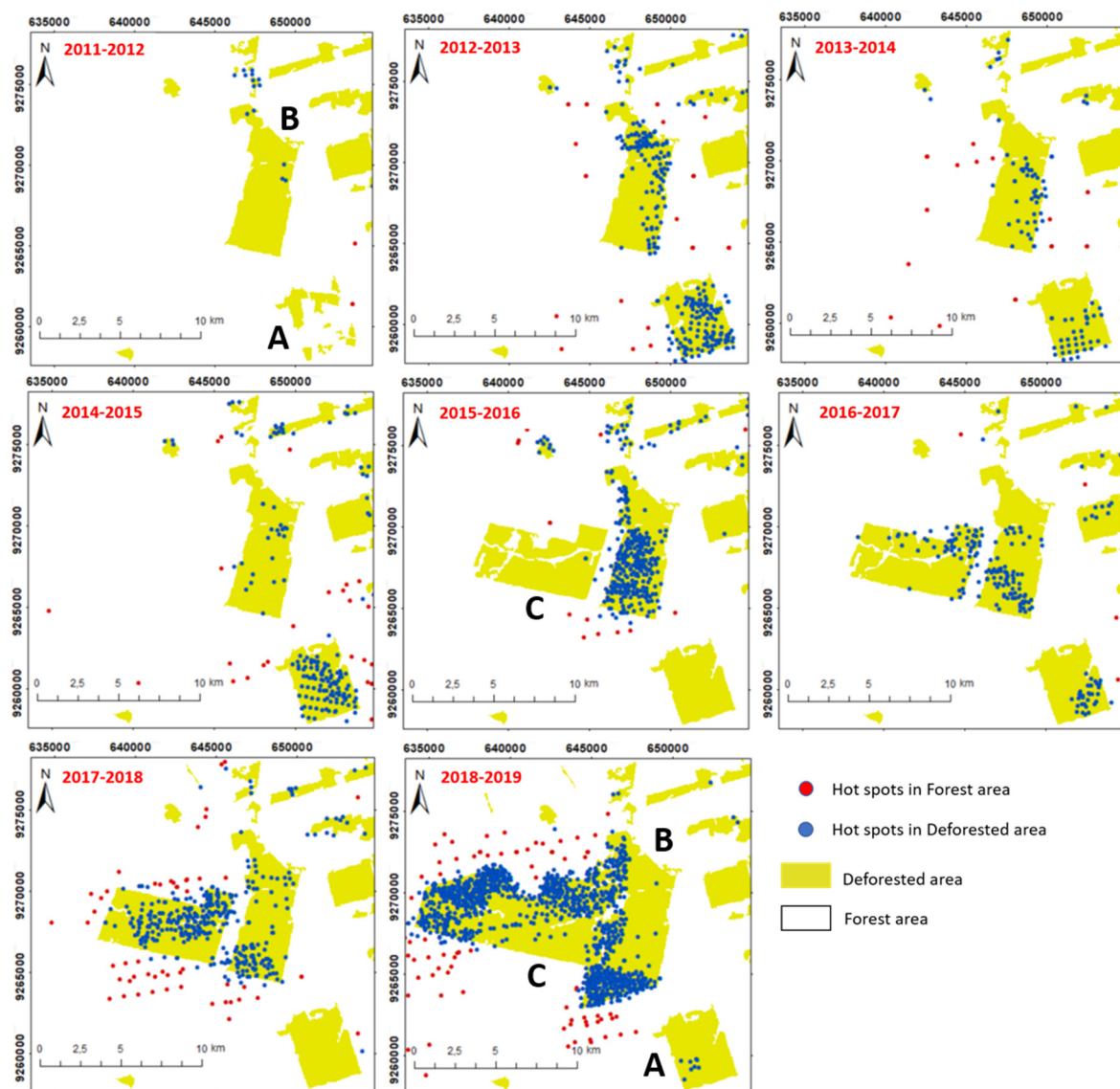

Figure 8. Deforestation dynamics from PY2011–2012 to PY2018–2019 in a portion of the Novo Progresso region. The figure, from upper-left to low-right, shows the yearly evolution of hotspots related to deforestation in deforested (blue dots) and forested (red dots) areas.

The occurrence of fire inside deforested areas can be observed in Figure 9. In PY2006–2007, the deforested area corresponded to 14.2% of the total Novo Progresso region. For the considered period, there was a steady increase in deforestation. By PY2018–2019, the deforested area accounted for 23.0%, an increase of 8.8% in land cleaning, which corresponds to

an area of 3250 km^2. In PY2006–2007, there were 11,769 occurrences of total fire hotspots in the Novo Progresso region, of which 82.4% were in deforested areas. In PY2018–2019, the hotspots in deforested area reached 94.5%, an increase of 12.1%. Fire outbreaks in deforested areas indicate the systematic use of fire as a means for new land clearing and land management practices.

The highest annual rate of deforestation occurred in PY2008–2009 (609.6 km^2) and the lowest in PY2016–2017 (83.5 km^2) (Table 2). After PY2008–2009, a deforestation peak occurred in PY2012–2013 (392.4 km^2), followed by the periods of PY2017–2018 and PY2018–2019 when deforestation rates rose again. Fire hotspots, though, increased at higher rates than deforestation, the curve fitting of fire outbreaks indicates a somehow steady increase of fire occurrences for the studied period. The average number of hotspots was 7597 from PY2006–2007 to PY2011–2012 and 30,440 from PY2012–2013 to PY2018–2019, four times higher than the previous period.
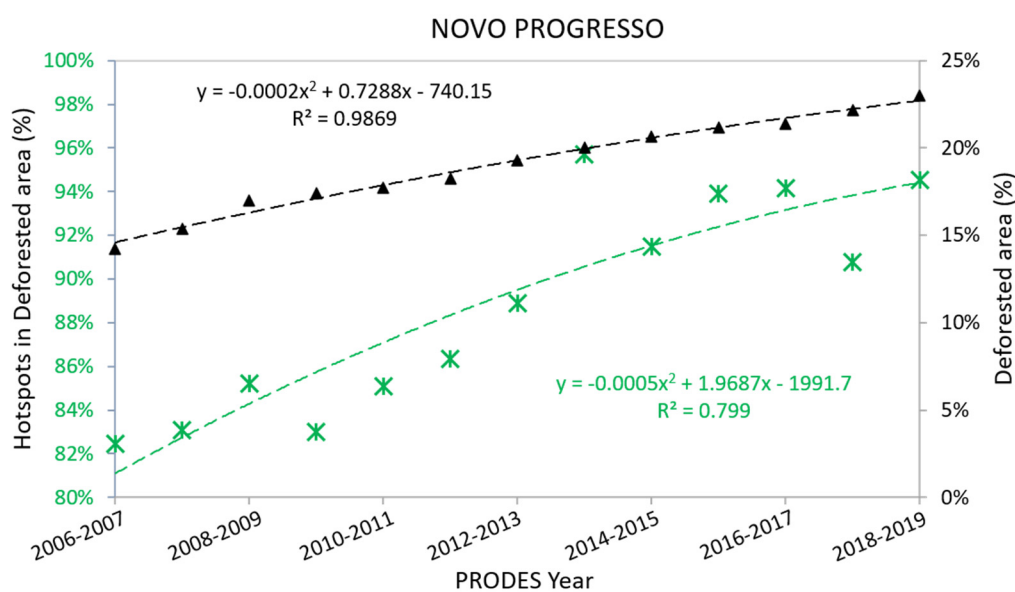

Figure 9. Temporal analysis of fire hotspots occurrence in the deforested areas (green) and the relative increase of deforestation (black) in the Novo Progresso region.

Figure 10 shows the number of fire hotspots detected inside the forest for PY2018–2019 as a function of distance from the edge of the deforested area. As can be seen, a significant incidence of fire outbreaks occurred in the first 800 m from the margins and extended up to 1200 m. The same behavior was also observed for the previous years. Other researchers had already recognized a more significant frequency of fires within forest areas and near the deforested areas [4–6,16,43,44,50]. The behavior of hotspot occurrences agrees with the data reported in References [40,44]. The increase of fires around the edges of deforested areas enhances the forest degradation along the edges. The decrease in forest resilience to fire makes it more susceptible to sustain biomass combustion due to the reduction in near-the-edge forest humidity. Periods of severe drought combined with an intense slash-and-burn activity favor the outbreaks of fires in standing degraded forests [69].

The research carried out by Matricardi et al. [70], during the period 1992 to 2014, revealed that forest degradation in the Brazilian Amazon had surpassed deforestation. They attributed 40% of the whole Amazon forest was degraded by intensive logging and understory fires, and the remaining 60% through edges and isolated forest fragmentation.

The influence of slash-and-burn practices near to forest degraded areas is evident, as shown by the plots in Figure 11. There is a direct correlation between forest clearing and forest degradation due to the use of fire on newly slashed areas. In that sense, forest clearing is a direct cause of primary forest degradation, as shown in Figure 8. A close look at the plots from PY2017–2018 and PY2018–2019 reveals the intense occurrences of fire

in forest areas, which was not observed in previous years, thus indicating the damage of a healthy ecosystem. For the time span of this study, the number of fire occurrences in healthy forest is from 5% to 20% of deforested areas. Then, the degraded area could be estimated, to some extent, based on the size of the pixel that characterizes a hotspot.
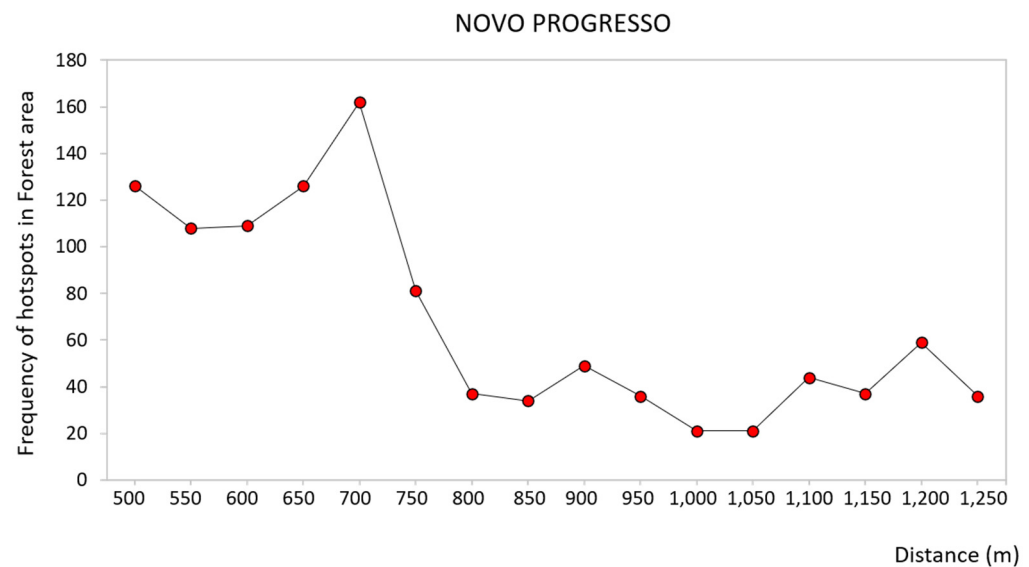

Figure 10. Number of fire hotspots in the forest area, for the PY2018–2019, identified according to their distance from the borders of the deforested areas in the Novo Progresso region.
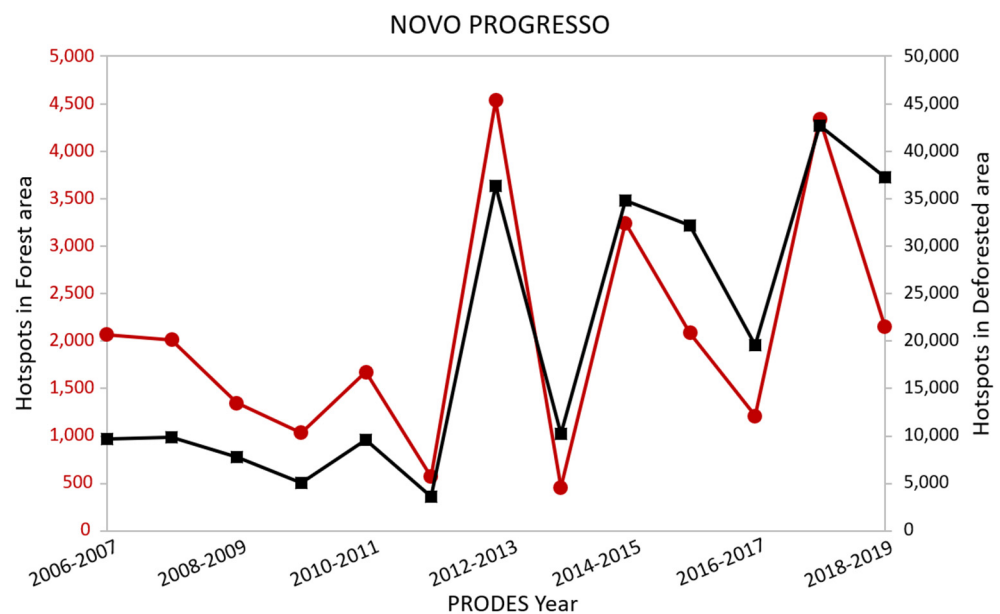

Figure 11. Fire hotspots inside the forest and in deforested area over time for the Novo Progresso region.

3.2. Fire Hotspots and Deforestation in the Pará State

In recent years, Pará State has faced high deforestation rates in the Brazilian Amazon. Table 3 shows the total occurrence of annual fire hotspots, the accumulated deforested areas, and the annual deforested area in this state. A total of 146,863 fire hotspots were detected in PY2006–2007 and 351,001 fire hotspots in PY2018–2019. In PY2006–2007, there was an accumulated deforested area equivalent to 9.35%. From PY2006–2007 to PY2018–2019, the deforested area reached 12.30%, a 2.95% increase in deforestation for the specified

period and area of 42,350 km². Fire occurrences, however, increased at a rate higher than deforestation, which also indicates forest degradation [4–6,29,69,70].

Figure 12 shows the variation of total fire hotspots from PY2007 to PY2019 along with the accumulated deforestation area in the Pará State. There was a positive correlation of 0.66 between total hotspots and deforested areas. It can be observed that the variation of total hotspots was stable from PY2006–2007 to PY2011–2012 and increased from PY2012–2013 to PY2018–2019. Similar trends were observed for the smaller area (Figure 9). There is an expectation that the local and regional deforestation practices also apply for the entire deforestation arch.

Table 3. Distribution of the total annual fire hotspots, accumulated deforested area (%), and annual deforested area (km²) in the Pará State, analyzed from July 2007 to December 2019.

PY	Total Annual Fire Hotspots	Accumulated Deforested Area (%)	Annual Deforested Area (km²)
2006–2007	146,863	9.35	5526
2007–2008	202,922	9.80	5607
2008–2009	119,234	10.14	4281
2009–2010	113,174	10.44	3770
2010–2011	174,394	10.69	3008
2011–2012	80,401	10.83	1741
2012–2013	372,391	11.01	2346
2013–2014	181,458	11.17	1887
2014–2015	324,024	11.34	2153
2015–2016	560,591	11.58	2992
2016–2017	276,283	11.77	2433
2017–2018	692,498	11.99	2744
2018–2019	351,001	12.30	3862

Source: Fire hotspots from the Forest Fire Program and deforestation from the Monitoring Deforestation of the Brazilian Amazon Forest by Satellite (PRODES) project produced by the National Institute for Space Research (INPE).
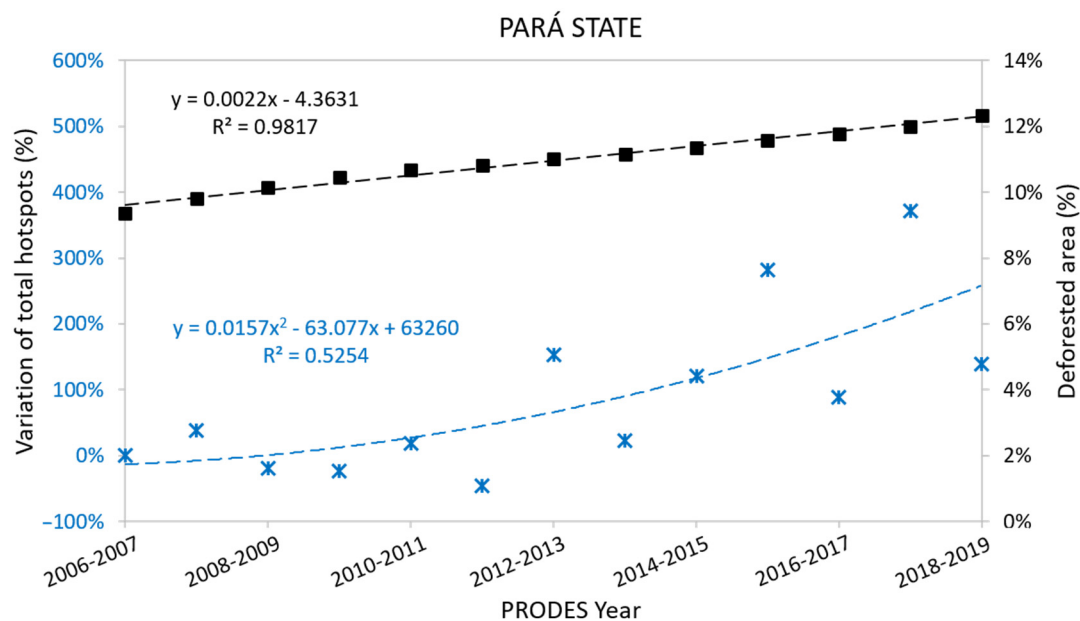

Figure 12. Variation of the total fire hotspots (blue) relative to the year PY2006–2007 and accumulated deforestation area (black) in the Pará State.

3.3. Gas and Particulate Emissions

Total gas and particulate emissions as a function of the burned area were calculated and summarized in Table 4. These data represent the emissions exclusively with the combustion of biomass from slash-and-burn activities. The efficiency of the first fire was about 50%. It did not include small fires that may take place in the degraded standing forest, pasture, or crop remaining over the bare soil. Also, the emissions are solely from the first fire of the newly slashed area. Over the years, after the initial large fire, stockpiled scorched biomass, i.e., the remaining 50%, is subjected to successive burns, ultimately approaching 100% combustion efficiency for that newly deforested area. Total CO_2 emissions accounted for the methane that is converted into an equivalent amount of CO_2, considering its relative radiative forcing, plus the emissions of the CO_2 itself, as shown in Figure 6.

Table 4. Gas emission estimates as for PY2019 slash-and-burn activities in the Brazilian Amazon.

Parameter (Units)	Novo Progresso Region	Pará State	Brazilian Amazon
Deforested area (ha)	33.15×10^3	446.30×10^3	1.09×10^6
Fresh biomass (Mton ha^{-1})	5.12×10^{-4}	5.70×10^{-4}	5.80×10^{-4}
Total Biomass (Mton)	16.97	254.2	632.4
CH_4 emitted (Mton)	0.047	0.67	1.7
CO_2 emitted (Mton)	7.86	109.2	293.3
Total CO_2 (Mton)	8.81	132.1	328.7
CO emitted (Mton)	0.55	8.3	20.41
NMHC emitted (Mton)	0.027	0.41	1.02
PM$_{2.5}$ emitted (Mton)	0.024	0.36	0.89

NMHC = non-methane hydrocarbon; PM = particulate matter.

A small region such as Novo Progresso emitted about 8.81 Mton of CO_2 over 331 km^2 of land approximately for the year PY2018–2019. For comparison, the carbon emission of Abruzzo region (Italy), with 1.30 million inhabitants, was 11.1 Mton for the year 2006 [71]. These data are even more alarming when we consider the emissions after deforestation practices in the Pará State, and the Brazilian Amazon, accounting for 132.1 and 328.7 Mton of CO_2 released to the atmosphere respectively, in the PY2018–2019. Other emissions are also of great concern in local and regional scales, notably, particulates of diameter less than 2.5 mm. Local, regional, and total emissions were about 0.027, 0.41, and 0.89 Mton, respectively. The same applies to CO emissions, accounting for 0.55, 8.3, and 20.41 Mton in Novo Progresso, Pará State, and Brazilian Amazon, respectively.

After the year 2000, high deforestation rates were observed in the period of 2002 to 2004, with an average of 24,939 km^2. In this time span, the lowest deforestation occurred in 2012, equivalent to 4561 km^2 following the voluntary REDD+ project's starting year [17]. Applying the same emission factors and other relevant data from Table 1, the total CO_2 emissions for the period 2002–2004 and in 2012 were 752.3 Mton and 137.6 Mton on average, respectively. The CO_2 emissions from 2019 are, therefore, 2.38 times higher than the minimum (2012) and 2.29 times smaller than the maximum (2002–2004). Emissions were estimated based on the deforested area. The results were not corrected for a possible offset from forest regrowth. According to Smith et al. [72], the yearly increase in secondary forest extent in the Brazilian Amazon was about 8.61% ± 10.96%, offsetting GHG emissions from newly slash-and-burned areas by 10.29% ± 6.8%. Taking this scenario into consideration, the net emissions from fires, for the year 2019, was 295 Mton of CO_2 for the Brazilian Amazon, which is 16.4% of the whole emissions from Brazil [73], that consumes about 50% of the recently slashed biomass.

In Brazil, the total CO_2 emissions related to deforestation practices of newly slashed areas in the Brazilian Amazon are higher than those from transport, electricity and heat, manufacturing, industry, buildings, aviation, and shipping sectors of the Brazilian economy. The emissions from deforestation of the Amazon rainforest in Brazil is next to the agricultural sector.

A rough estimate of burned biomass on wide areas can be carried out using geostationary satellite sensor data starting from the computation of the fire radiative power, which is the power radiated by the fire. By integrating this quantity over time, it is possible to estimate the radiative fire energy and the burned biomass, and then the emissions in the atmosphere if the coefficients providing the burning efficiency of vegetation affected by the fire are available [74]. This will be the subject of a forthcoming paper.

4. Conclusions

This work showed a strong correlation between the occurrence of fire in the newly deforested area in the municipality of Novo Progresso following the local slash-and-burn practices. The same trends were also observed for the Pará State, suggesting a common practice along with the deforestation arch. The study indicated positive correlations of 0.72 and 0.66 between deforestation and fire occurrences in local and regional scales, respectively. The use of fire as a rapid means for forest clearing was evident for the PY2018–2019, which showed a strong overlapping of slash-and-burn activities in a brief period. Many fire occurrences inside the forest in the near recent deforested areas result in ecosystem degradation, turning it more prone to future fire events. The area of old-growth forest, negatively influenced by nearby slash-and-burn practices, is a fraction of the deforested area, thus enlarging forest degradation. The occurrences of hotspots in the healthy forest are from 5% to 20% of newly deforested areas. This is a strong indication of the primary cause of forest degradation due to slash-and-burn practices. The steady increase in deforestation after the PY2011–2012 is a worldwide concern because of the loss of intact forest and the massive greenhouse gases emissions, from the slash-and-burn practices, accounting for about 295 million tons of CO_2 for the PY2018–2019 alone.

Author Contributions: Conceptualization, methodology, formal analysis, data curation, writing—original draft preparation, funding acquisition, C.A.S.; writing—review and editing, C.A.S., G.S., E.E.S. and G.L. All authors have read and agreed to the published version of the manuscript.

Data Availability Statement: The data presented in this study are available upon request for the corresponding author.

Conflicts of Interest: We declare no conflict of interest.

References

1. Aragão, L.E.O.C.; Poulter, B.; Barlow, J.B.; Anderson, L.O.; Malhi, Y.; Saatchi, S.; Phillips, O.L.; Gloor, E. Environmental change and the carbon balance of Amazonian forests. *Biol. Rev.* **2014**, *89*, 913–931. [CrossRef] [PubMed]
2. FAO. UM-REDD Programme. Available online: http://www.un-redd.org/how-we-work (accessed on 31 August 2020).
3. Bustamante, M.M.; Roitman, I.; Aide, T.M.; Alencar, A.; Anderson, L.O.; Aragão, L.; Asner, G.P.; Barlow, J.; Berenguer, E.; Chambers, J.; et al. Toward an integrated monitoring framework to assess the effects of tropical forest degradation and recovery on carbon stocks and biodiversity. *Glob. Chang. Biol.* **2016**, *22*, 92–109. [CrossRef] [PubMed]
4. Nepstad, D.C.; Veríssimo, A.; Alencar, A.; Nobre, C.; Lima, E.; Lefebvre, P.; Schlesinger, P.; Potter, C.; Moutinho, P.; Mendoza, E.; et al. Large-scale impoverishment of Amazonian forests by logging and fire. *Nature* **1999**, *398*, 505–508. [CrossRef]
5. Nepstad, D.; Carvalho, G.; Barros, A.C.; Alencar, A.; Capobianco, J.P.; Bishop, J.; Moutinho, P.; Lefebvre, P.; Silva, U.L., Jr.; Prins, E. Road paving, fire regime feedbacks, and the future of Amazon forests. *For. Ecol. Manag.* **2001**, *154*, 395–407. [CrossRef]
6. Cochrane, M.A. Fire science for rainforests. *Nature* **2003**, *421*, 913–919. [CrossRef] [PubMed]
7. Bowman, M.S.; Soares-Filho, B.S.; Merry, F.D.; Nepstad, D.C.; Rodrigues, H.; Almeida, O.T. Persistence of cattle ranching in the Brazilian Amazon: A spatial analysis of the rationale for beef production. *Land Use Policy* **2012**, *29*, 558–568. [CrossRef]

8.   Domingues, M.S.; Bermann, C. O arco de desflorestamento na Amazônia: Da pecuária à soja. *Ambient. Soc.* **2012**, *15*, 1–22. [CrossRef]

9.   Kastens, J.H.; Brown, J.C.; Coutinho, A.C.; Bishop, C.R.; Esquerdo, J.C.D.M. Soy moratorium impacts on soybean and deforestation dynamics in Mato Grosso, Brazil. *PLoS ONE* **2017**, *12*, e0176168. [CrossRef]

10.   Yanai, A.M.; Nogueira, E.M.; Graça, P.M.L.A.; Fearnside, P.M. Deforestation and carbon stock loss in Brazil's Amazonian settlements. *Environ. Manag.* **2017**, *59*, 393–409. [CrossRef]

11.   Farias, M.H.C.S.; Beltrão, N.E.S.; Cordeiro, Y.E.M.; Santos, C.A. Impact of rural settlements on the deforestation of the Amazon. *Mercator* **2018**, *17*, e17009. [CrossRef]

12.   Yanai, A.M.; Graça, P.M.L.A.; Escada, M.I.S.; Ziccardi, L.G.; Fearnside, P.M. Deforestation dynamics in Brazil´s Amazonian settlements: Effects of land-tenure concentration. *J. Environ. Manag.* **2020**, *268*, 110555. [CrossRef] [PubMed]

13.   INPE. Terrabrasilis. Available online: http://terrabrasilis.dpi.inpe.br/en/home-page/ (accessed on 30 August 2020).

14.   Azevedo-Ramos, C.; Moutinho, P. No man's land in the Brazilian Amazon: Could undesignated public forests slow Amazon deforestation? *Land Use Policy* **2018**, *73*, 125–127. [CrossRef]

15.   Souza, C.M., Jr.; Shimbo, J.Z.; Rosa, M.R.; Parente, L.L.; Alencar, A.A.; Rudorff, B.F.T.; Hasenack, H.; Matsumoto, M.; Ferreira, L.G.; Souza-Filho, P.W.M.; et al. Reconstructing three decades of land use and land cover changes in Brazilian biomes with Landsat archive and Earth Engine. *Remote Sens.* **2020**, *12*, 2735. [CrossRef]

16.   Soares-Filho, B.S.; Nepstad, D.C.; Curran, L.M.; Cerqueira, G.C.; Garcia, R.A.; Ramos, C.A.; Voll, E.; McDonald, A.; Lefebvre, P.; Schlesinger, P. Modelling conservation in the Amazon basin. *Nature* **2006**, *440*, 520–523. [CrossRef]

17.   West, T.A.; Börner, J.; Sills, E.O.; Kontoleon, A. Overstated carbon emission reductions from voluntary REDD+ projects in the Brazilian Amazon. *Proc. Natl. Acad. Sci. USA* **2020**, *117*, 24188–24194. [CrossRef]

18.   United Nations Climate Change. Copenhagen Climate Change Conference. Available online: https://unfccc.int/process-and-meetings/conferences/past-conferences/copenhagen-climate-change-conference-december-2009/copenhagen-climate-change-conference-december-2009 (accessed on 19 November 2020).

19.   Law No. 12.727, 17 October 2012. Available online: http://www.planalto.gov.br/ccivil_03/_ato2011-2014/2012/lei/l12727.htm (accessed on 19 November 2020).

20.   Sorrensen, C.L. Linking small holder land use and fire activity: Examining biomass burning in the Brazilian Lower Amazon. *For. Ecol. Manag.* **2000**, *128*, 11–25. [CrossRef]

21.   Asner, G.P.; Knapp, D.E.; Broadbent, E.N.; Oliveira, P.J.C.; Keller, M.; Silva, J.N. Selective logging in the Brazilian Amazon. *Sci.* **2005**, *310*, 480–482. [CrossRef]

22.   Broadbent, E.N.; Asner, G.P.; Keller, M.; Knapp, D.E.; Oliveira, P.J.C.; Silva, J.N. Forest fragmentation and edge effects from deforestation and selective logging in the Brazilian Amazon. *Biol. Conserv.* **2008**, *141*, 1745–1757. [CrossRef]

23.   Barber, C.P.; Cochrane, M.A.; Souza, C.M., Jr.; Laurance, W.F. Roads, deforestation, and the mitigating effect of protected areas in the Amazon. *Biol. Conserv.* **2014**, *177*, 203–209. [CrossRef]

24.   Alencar, A.; Nepstad, D.; Diaz, M.C.V. Forest understory fire in the Brazilian Amazon in ENSO and non-ENSO years: Area burned and committed carbon emissions. *Earth Interact.* **2006**, *10*, 1–17. [CrossRef]

25.   Matricardi, E.A.T.; Skole, D.; Pedlowski, M.A.; Chomentowski, W.; Fernandes, L.C. Assessment of tropical forest degradation by selective logging and fire using Landsat imagery. *Remote Sens. Environ.* **2010**, *114*, 1117–1129. [CrossRef]

26.   Barni, P.E.; Pereira, V.B.; Manzi, A.O.; Barbosa, E.I. Deforestation and forest fires in Roraima and their relationship with phytoclimatic regions in the northern Brazilian Amazon. *Environ. Manag.* **2015**, *55*, 1124–1138. [CrossRef] [PubMed]

27.   Pinheiro, T.F.; Escada, M.I.S.; Valeriano, D.M.; Hostert, P.; Gollnow, F.; Müller, H. Forest degradation associated with logging frontier expansion in the Amazon: The BR-163 region in southwestern Pará, Brazil. *Earth Interact.* **2016**, *20*, 1–26. [CrossRef]

28.   Arima, E.Y.; Walker, R.T.; Perz, S.G.; Caldas, M. Loggers and forest fragmentation: Behavioral models of road building in the Amazon basin. *Ann. Am. Assoc. Geogr.* **2005**, *95*, 525–541. [CrossRef]

29.   Souza, G.M.; Escada, M.I.S.; Capanema, V.P. Cicatrizes de queimadas e padrões de mudanças de uso e cobertura da terra no sudoeste do estado do Pará, Brasil. In Proceedings of the XVIII Simpósio Brasileiro de Sensoriamento Remoto (SBSR), Santos, Brazil, 28–31 May 2017; pp. 5760–5767.

30.   Butt, N.; Oliveira, P.A.; Costa, M.H. Evidence that deforestation affects the onset of the rainy season in Rondônia, Brazil. *J. Geophys. Res.* **2011**, *116*, 2–9. [CrossRef]

31.   Knox, R.; Bisht, G.; Wang, J.; Bras, R.L. Precipitation variability over the forest-to-nonforest transition in Southwestern Amazonia. *J. Clim.* **2011**, *24*, 2368–2377. [CrossRef]

32.   Davidson, E.A.; Araújo, A.C.; Artaxo, P.; Balch, J.K.; Brown, I.F.; Bustamante, M.M.C.; Coe, M.T.; DeFRIES, R.S.; Keller, M.; Longo, M.; et al. The Amazon basin in transition. *Nature* **2012**, *481*, 321–328. [CrossRef]

33.   Jiménez-Muñoz, J.C.; Mattar, C.; Barichivich, J.; Santamaría-Artigas, A.; Takahashi, K.; Malhi, Y.; Sobrino, A.J.; Van Der Schrier, G. Record-breaking warming and extreme drought in the Amazon rainforest during the course of El Niño 2015–2016. *Sci. Rep.* **2016**, *6*, 33130. [CrossRef]

34.   Zemp, D.C.; Schleussner, C.F.; Barbosa, H.; Rammig, A. Deforestation effects on Amazon forest resilience. *Geophys. Res. Lett.* **2017**, *44*, 6182–6190. [CrossRef]

35. Aragão, L.E.; Anderson, L.O.; Fonseca, M.G.; Rosan, T.M.; Vedovato, L.B.; Wagner, F.H.; Silva, C.V.J.; Junior, C.H.S.; Arai, E.; Aguiar, A.P.; et al. 21st Century drought-related fires counteract the decline of Amazon deforestation carbon emissions. *Nat. Commun.* **2018**, *9*, 536. [CrossRef]

36. Fearnside, P.M.; Graça, P.M.L.D.A.; Keizer, E.W.H.; Maldonado, F.D.; Barbosa, R.I.; Nogueira, E.M. Modelagem de desmatamento e emissões de gases de efeito estufa na região sob influência da rodovia Manaus-Porto Velho (BR-319). *Rev. Bras. Meteorol.* **2009**, *24*, 208–233. [CrossRef]

37. Aragão, L.E.O.C.; Shimabukuro, Y.E. The incidence of fire in Amazonian forests with implications for REDD. *Science* **2010**, *328*, 1275–1278. [CrossRef] [PubMed]

38. Hosonuma, N.; Herold, M.; Sy, V.; de Fries, R.S.; Brockhaus, M.; Verchot, L.; Angelsen, A.; Romijn, E. An assessment of deforestation and forest degradation drivers in developing countries. *Environ. Res. Lett.* **2012**, *7*, 044009. [CrossRef]

39. Spracklen, D.V.; Garcia-Carreras, L. The impact of Amazonian deforestation on Amazon basin rainfall. *Geophys. Res. Lett.* **2015**, *42*, 9546–9552. [CrossRef]

40. Jusys, T. Fundamental causes and spatial heterogeneity of deforestation in Legal Amazon. *Appl. Geogr.* **2016**, *75*, 188–199. [CrossRef]

41. Ruiz-Vásquez, M.; Arias, P.A.; Martínez, J.A.; Espinoza, J.C. Effects of Amazon basin deforestation on regional atmospheric circulation and water vapor transport towards tropical South America. *Clim. Dyn.* **2020**, *54*, 4169–4189. [CrossRef]

42. Krieger-Filho, G.C.; Bufacchi, P.; Santos, J.C.; Veras, C.A.G.; Alvarado, E.C.; Mell, W.; Carvalho, J.A., Jr. Probability of surface fire spread in Brazilian rainforest fuels from outdoor experimental measurements. *Eur. J. Forest Res.* **2017**, *136*, 217–232. [CrossRef]

43. Carvalho, J.A., Jr.; Veras, C.A.G.; Alvarado, E.C.; Sandberg, D.V.; Leite, S.J.; Gielow, R.; Rabelo, E.R.C.; Santos, J.C. Understory fire propagation and tree mortality on adjacent areas to an Amazonian deforestation fire. *Int. J. Wildland Fire* **2010**, *19*, 795–799. [CrossRef]

44. Silva Júnior, C.H.L.; Aragão, L.E.O.; Fonseca, M.G.; Almeida, C.T.; Vedovato, L.B.; Anderson, L.O. Deforestation-induced fragmentation increases forest fire occurrence in central Brazilian Amazonia. *Forests* **2018**, *9*, 305. [CrossRef]

45. Carvalho, J.A., Jr.; Higuchi, N.; Araújo, T.M.; Santos, J.C. Combustion completeness in a rainforest clearing experiment in Manaus, Brazil. *J. Geophys. Res.* **1998**, *103*, 13195–13199. [CrossRef]

46. Carvalho, J.A., Jr.; Costa, F.S.; Veras, C.A.G.; Sandberg, D.V.; Alvarado, E.C.; Gielow, R.; Serra, A.M.; Santos, J.C. Biomass fire consumption and carbon release rates of rainforest-clearing experiments conducted in northern Mato Grosso, Brazil. *J. Geophys. Res.* **2001**, *106*, 17877–17887. [CrossRef]

47. Carvalho, E.R.; Veras, C.A.G.; Carvalho, J.A., Jr. Experimental investigation of smouldering in biomass. *Biomass Bioenerg.* **2002**, *22*, 283–294. [CrossRef]

48. Rabelo, E.R.C.; Veras, C.A.G.; Carvalho, J.A., Jr.; Alvarado, E.C.; Sandberg, D.V.; Santos, J.C. Log smoldering after an Amazonian deforestation fire. *Atmos. Environ.* **2004**, *38*, 203–211. [CrossRef]

49. Christian, T.J.; Yokelson, R.J.; Carvalho, J.A., Jr.; Griffith, D.W.T.; Alvarado, E.C.; Santos, J.C.; Soares Neto, T.G.; Veras, C.A.G.; Hao, W.M. The tropical forest and fire emissions experiment: Trace gases emitted by smoldering logs and dung from deforestation and pasture fires in Brazil. *J. Geophys. Res. Atmos.* **2007**, *112*, 2156–2202. [CrossRef]

50. Amaral, C.S.S., Jr.; Amaral, S.S.; Costa, M.A.M.; Soares Neto, T.G.; Veras, C.A.G.; Costa, F.S.; van Leeuwen, T.T.; Krieger Filho, G.C.; Tourigny, E.; Forti, M.C.; et al. CO_2 and CO emission rates from three forest fire controlled experiments in Western Amazonia. *Atmos. Environ.* **2016**, *135*, 73–83. [CrossRef]

51. Van Marle, M.J.E.; Field, R.D.; van der Werf, G.R.; Wagt, I.A.E.; Houghton, R.A.; Rizzo, L.V.; Artaxo, P.; Tsigaridis, K. Fire and deforestation dynamics in Amazonia (1973–2014). *Glob. Biogeochem. Cycles* **2017**, *31*, 24–38. [CrossRef]

52. Soares Neto, T.G.; Carvalho, J.A., Jr.; Veras, C.A.G.; Alvarado, E.C.; Gielow, R.; Lincoln, E.N.; Cristian, T.J.; Yokelson, R.J.; Santos, J.C. Biomass consumption, CO_2, CO and main hydrocarbon gas emissions in an Amazonian forest clearing fire. *Atmos. Environ.* **2009**, *43*, 438–446. [CrossRef]

53. Lima, A.; Silva, T.S.F.; de Feitas, R.M.; Adami, M.; Formaggio, A.R.; Shimabukuro, Y.E. Land use and land cover changes determine the spatial relationship between fire and deforestation in the Brazilian Amazon. *Appl. Geogr.* **2012**, *34*, 239–246. [CrossRef]

54. Crowson, M.; Ron, H.; Björn, W. Mapping land cover change in northern Brazil with limited training data. *Int. J. Appl. Earth Obs. Geoinf.* **2019**, *78*, 202–214. [CrossRef]

55. Jakimow, B.; Griffiths, P.; van der Linden, S.; Hostert, P. Mapping pasture management in the Brazilian Amazon from dense Landsat time series. *Remote Sens. Environ.* **2018**, *205*, 453–468. [CrossRef]

56. Müller, H.; Griffiths, P.; Hostert, P. Long-term deforestation dynamics in the Brazilian Amazon—Uncovering historic frontier development along the Cuiabá–Santarém highway. *Int. J. Appl. Earth Obs. Geoinf.* **2016**, *44*, 61–69. [CrossRef]

57. ESA. EO Browser. Available online: https://apps.sentinel-hub.com/eo-browser/ (accessed on 20 November 2020).

58. Assis, L.F.F.G.; Ferreira, K.R.; Vinhas, L.; Maurano, L.; Almeida, C.; Carvalho, A.; Rodrigues, J.; Maciel, A.; Camargo, C. TerraBrasilis: A spatial data analytics infrastructure for large-scale thematic mapping. *ISPRS Int. J. GeoInf.* **2019**, *8*, 513. [CrossRef]

59. INPE. Monitoramento de Queimadas e Incêndios por Satélite em Tempo Quase-Real. Available online: http://queimadas.dgi.inpe.br/queimadas/portal (accessed on 31 August 2020).

60. Giglio, L.; Descloitres, J.; Justice, C.O.; Kaufman, Y.J. An enhanced contextual fire detection algorithm for MODIS. *Remote Sens. Environ.* **2003**, *87*, 273–282. [CrossRef]

61. Giglio, L.; Schroeder, W.; Justice, C.O. The collection 6 MODIS active fire detection algorithm and fire products. *Remote Sens. Environ.* **2016**, *178*, 31–41. [CrossRef] [PubMed]

62. Di Biase, V.; Laneve, G. Geostationary sensor based forest fire detection and monitoring: An improved version of the SFIDE algorithm. *Remote Sens.* **2018**, *10*, 741. [CrossRef]

63. Kaufman, Y.J.; Justice, C.O.; Flynn, L.P.; Kendall, J.D.; Prins, E.M.; Giglio, L.; Ward, D.E.; Menzel, W.P.; Setzer, A.W. Potential global fire monitoring from EOS-MODIS. *J. Geophys. Res. Atmos.* **1998**, *103*, 32215–32238. [CrossRef]

64. Justice, C.O.; Giglio, L.; Korontzi, S.; Owens, J.; Morisette, J.T.; Roy, D.; Descloitres, J.; Alleaume, S.; Petitcolin, F.; Kaufman, Y. The MODIS fire products. *Remote Sens. Environ.* **2002**, *83*, 244–262. [CrossRef]

65. Hantson, S.; Padilla, M.; Corti, D.; Chuvieco, E. Strengths and weaknesses of MODIS hotspots to characterize global fire occurrence. *Remote Sens. Environ.* **2013**, *131*, 152–159. [CrossRef]

66. Silva, C.A.; Santilli, G.; Sano, E.E.; Rodrigues, S.W.P. Análise qualitativa do desmatamento na Floresta Amazônica a partir de sensores SAR, óptico e termal. *Anu. Inst. Geociênc.* **2019**, *42*, 18–29. [CrossRef]

67. Santana, N.C.; Carvalho Júnior, O.A.; Gomes, R.A.T.; Guimarães, R.F. Burned-area detection in Amazonian environments using standardized time series per pixel in MODIS data. *Remote Sens.* **2018**, *10*, 1904. [CrossRef]

68. Soares-Filho, B.; Rajão, R.; Macedo, M.; Carneiro, A.; Costa, W.; Coe, M.; Rodrigues, H.; Alencar, A. Cracking Brazil's forest code. *Science* **2014**, *344*, 363–364. [CrossRef] [PubMed]

69. Silva, S.S.; Fearnside, P.M.; Graça, P.M.L.A.; Brown, I.F.; Alencar, A.; Melo, A.W.F. Dynamics of forest fires in the southwestern Amazon. *For. Ecol. Manag.* **2018**, *424*, 312–322. [CrossRef]

70. Matricardi, E.A.T.; Skole, D.L.; Costa, O.B.; Pedlowski, M.A.; Samek, J.H.; Miguel, E.P. Long-term forest degradation surpasses deforestation in the Brazilian Amazon. *Science* **2020**, *369*, 1378–1382. [CrossRef] [PubMed]

71. Pulselli, R.M.; Romano, P.; Marchi, M.; Bastianoni, S. Carbon emission intensity and areal empower density: Combining two systemic indicators to inform the design and planning of sustainable energy landscapes. Chapter 19. In *Sustainable Energy Landscapes: Designing, Planning, and Development*; Stremke, S., van den Dobbelsteen, A., Eds.; CRC Press: Boca Raton, FL, USA, 2013; pp. 385–406.

72. Smith, C.C.; Espírito-Santo, F.D.B.; Healey, J.R.; Young, P.J.; Lennox, G.D.; Ferreira, J.; Barlow, J. Secondary forests offset less than 10% of deforestation-mediated carbon emissions in the Brazilian Amazon. *Glob. Chang. Biol.* **2020**, *26*, 7006–7020. [CrossRef] [PubMed]

73. SEEG—Sistema de Estimativa de Emissão de Gases do Efeito Estufa. Available online: http://seeg.eco.br (accessed on 4 January 2021).

74. Laneve, G.; Cadau, E.G.; Santilli, G. Estimation of the burned biomass based on the quasi-continuous MSG/SEVIRI Earth observation system. In Proceedings of the IEEE International Geoscience and Remote Sensing Symposium (IGARSS 2009), Cape Town, South Africa, 12–19 July 2009.

Taylor & Francis
Taylor & Francis Group

Near-real time deforestation detection in the Brazilian Amazon with Sentinel-1 and neural networks

Claudia Arantes Silva[a], Giorgia Guerrisi[b], Fabio Del Frate[b] and Edson Eyji Sano[c]

[a]Institute of Geosciences, Applied Geosciences and Geodynamics Program, Universidade de Brasília, Brasília, Brazil; [b]EMBRAPA (Brazilian Agricultural Research Corporation),Brasilla, Brazil; [c]Civil Engineering and Computer Science Engineering Department, University of Rome "Tor Vergata", Rome, Italy

ABSTRACT

Optical-based near-real time deforestation alert systems in the Brazilian Amazon are ineffective in the rainy season. This study identify clear-cut deforested areas through Neural Network (NN) algorithm based on C-band, VV- and VH-polarized, Sentinel-1 images. Statistical parameters of backscatter coefficients (mean, standard deviation, and the difference between maximum and minimum values – MMD) were computed from 30 Sentinel-1 images, from 2019, used as input parameters of the NN classifier. The samples were manually selected, including forested and deforested areas. After deforestation, mean backscatter signals decreased on the average of 2 dB for VV and 2.3 dB for VH from May to September–October. A Multi-Layer Perceptron (MLP) network was used for detecting near-real time forest disturbances larger than 2 ha. Case studies were performed for both polarizations considered the following input sets to the MLP: mean; mean and standard deviation; mean and MMD; and mean, standard deviation, and MMD. For the 2019 dataset, the latter showed the best performance of the NN algorithm with accuracy and F1 score of 99%. Automatic extraction using 2018 Sentinel-1 images reached accuracy and F1 score of 89% with the MapBiomas reference data and accuracy of 81% and F1 score of 79% with the PRODES reference data.

Introduction

The Brazilian Amazon covers an area of approximately 5.2 million km², about 60% of the Brazilian territory, encompassing the following states: Acre (AC), Amapá (AP), Amazonas (AM), Mato Grosso (MT), Pará (PA), Rondônia (RO), Roraima (RR), Tocantins (TO), and part of Maranhão (MA; Figure 1). Satellite-based monitoring of such a large territory is a complex task because of its continental size and long rainy seasons. Forest disturbance in the Brazilian Amazon by human occupation is mostly concentrated in a large region named deforestation arch. The arch has about 1.7 million km² (33% of the Brazilian Amazon), extends from northeast of Maranhão State to southeast of Acre State, and concentrates most of the monitoring efforts conducted by the Brazilian environmental organizations (Cochrane, 2003; Davidson et al., 2012; Farias et al., 2018; D. Nepstad et al., 2001; Souza et al., 2020; Yanai et al., 2017).

Clear-cut deforestation larger than 200 hectares was commonly observed in the region between 2000 and 2018 (Davis et al., 2020). In the last five years (2016–2020), the Brazilian Amazon has lost about 43,300 km² of forest cover. Deforestation, which is frequently associated with fire occurrences and illegal selective logging (Silva Júnior et al., 2018; Van Marle et al., 2017), exceeded 10,000 km² in 2019 and 10,800 km² in 2020. The Brazilian Amazon has also been degraded by intensive selective logging

activities, causing a significant loss of forest diversity (Bezerra et al., 2021; Matricardi et al., 2020). Silva et al. (2021) recently addressed the dynamics of occupation and greenhouse gas emissions in this region. Pará is the state presenting the highest levels of deforestation since 2006, mostly driven by the rural settlement, beef production, crop plantation, and large reservoirs of hydropower plants (D. C. Nepstad et al., 1999; Farias et al., 2018; Kastens et al., 2017; Yanai et al., 2020).

The National Institute for Space Research (INPE) is the Brazilian institution responsible for monitoring annual deforestation in the Brazilian Amazon through the Project of the Deforestation Monitoring by Satellite (PRODES). The program relies on optical sensors onboard the Landsat 8, Sentinel-2, and China–Brazil Earth Resources Satellite (CBERS-4 and CBERS-4A) satellites. In this project, deforestation is defined as the conversion of primary forest into clear-cut areas (Diniz et al., 2015; Terrabrasilis – Geographic Data Platform, n. d.). Reports and deforestation data about the Brazilian Amazon can also be obtained from the Brazilian Annual Land Use and Land Cover Mapping Project (MapBiomas initiative). It is a non-governmental organization that generates annual land use and land cover (LULC) time series of the entire country through the Landsat satellite data processing and analysis in the Google Earth Engine platform (Davis et al., 2020; Mapbiomas Brasil, n.d.).

CONTACT Claudia Arantes Silva ✉ silvaclaudia.geo@gmail.com ⦿ Instituto de Geociências (Ig), Universidade de Brasília, Brasília, Brazil
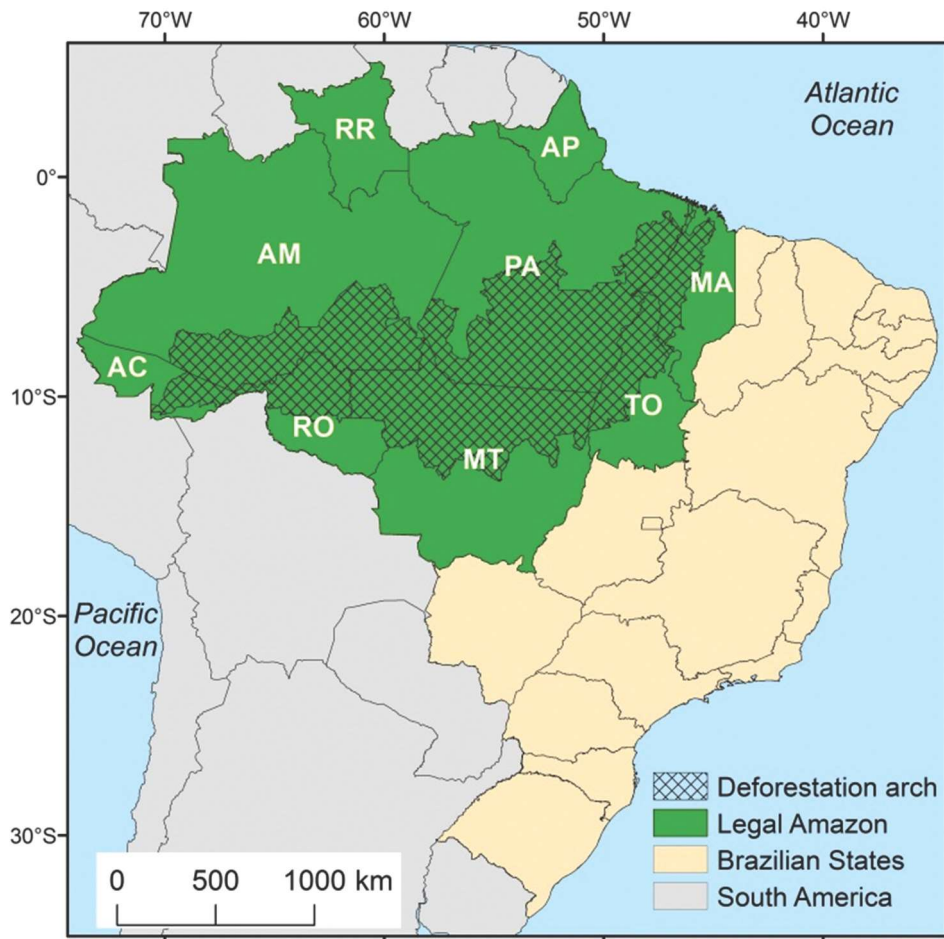
Figure 1. Location of the Brazilian Legal Amazon and the deforestation arch in Brazil. State identification: AC = Acre; AM = Amazonas; AP = Amapá; MA = Maranhão; MT = Mato Grosso; PA = Pará; RO = Rondônia; RR = Roraima; and TO = Tocantins.

During the rainy season, when the forest monitoring based on optical satellites is impaired, the Management and Operational Center for the Amazon Protection System (Censipam), from the Ministry of Defense, is the organization responsible for processing the X-band, synthetic aperture radar (SAR) images over critical areas. Regrettably, the reports issued by the institution are used basically for environmental law enforcement procedures. Figure 2 shows the deforestation process and weather conditions throughout the year in the Brazilian Amazon.

Currently, in terms of Brazilian satellites, the Brazilian Amazon is imaged by the joint Brazil–China, CBERS-4A optical satellite along with the Amazonia-1 satellite. The latter carries a wide-view optical imager with three visible (VIS) bands and one near-infrared (NIR) band with a swath of 850 km and 60 m of spatial resolution. The Ministry of Defense and INPE are currently conducting the zero-phase analysis of the national SAR mission. The integration of optical and SAR imageries can improve forest monitoring in tropical regions. Reiche et al. (2015) fused Landsat normalized difference vegetation index (NDVI) and L-band ALOS PALSAR backscatter time

series in the Viti Levu Island, Fiji. They found a strong correlation between the backscatter multi-temporal HV/HH ratio and NDVI, while the accuracy using only NDVI decreased significantly.

Monitoring the Brazilian rainforest through remote sensing claims for some level of automation because of its large territorial extent. Neural networks (NNs) are one of the most advanced technological frontiers to increase the automation level in satellite image processing. A NN is a massively parallel distributed processor made up of simple processing units using cumulative empirical knowledge (Haykin, 2009). It has been successfully applied in different cases. Del Frate and Wang (2001) analysed the C- and L-band backscatter coefficients for retrieving sunflower biomass using NN algorithm to perform the inversion modelling. NN has been also applied to map the evolution of human settlements and urban land using C-band SAR images (Del Frate et al., 2008), to characterize the seismic source of an earthquake and its geometric parameters (Stramondo et al., 2011), to classify different crops by multi-polarized and multi-temporal backscattering coefficients (Del Frate et al., 2003), to detect land cover changes in urban areas
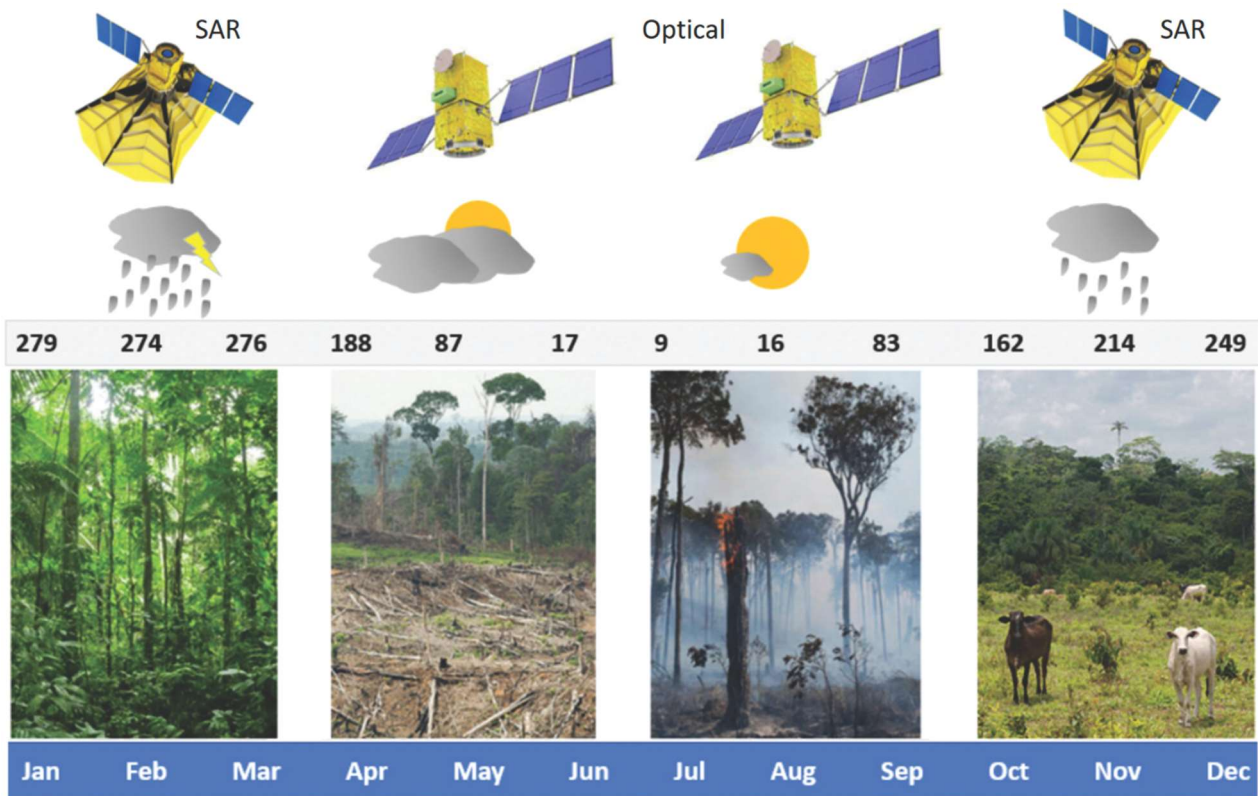
Figure 2. Deforestation process and weather conditions commonly found in the Brazilian Amazon over the year. The numbers above the images correspond to the monthly average precipitation (mm) for the southwest of Pará State from the period 1999–2020.

using X-band SAR images (Pratola et al., 2013), and to detect vegetation burnt areas to monitor regrowth of maquis vegetation with X-band data (Laurin et al., 2018).

Del Frate and Solimini (2004) proposed a NN algorithm to estimate soil moisture, leaf area index (LAI), and biomass in wheat fields. The algorithm was tested with experimental data collected at X-, C-, and S-bands. The model was based on the radiative transfer theory and a combination of scattering contributions. These authors obtained good results of moisture retrieval over bare soil and moderate results under vegetation cover. Even though the saturation effects reduced the absolute accuracy, the algorithm could reproduce the biomass trend with a reasonable agreement. Laurin et al. (2013) used the NN classifier to map areas of tropical forests in West Africa. In this study, the authors applied Landsat, ALOS AVNIR-2, and ALOS PALSAR data. The classification results were evaluated using optical data alone, SAR data alone, Landsat and PALSAR, AVNIR-2 and PALSAR, and a combination of three sensors. The integration of the three sensors reached the best results.

Few works have been conducted using machine learning algorithms or SAR images to detect deforestation in the Amazon rainforest. Bem et al. (2020) proposed a method based on convolutional neural networks (CNNs) applied to Landsat optical images from the Brazilian Amazon. They investigated different CNN architectures to predict annual changes in vegetation cover, comparing the results with two other machine learning algorithms, the Random Forest and the Multi-Layer Perceptron (MLP). They obtained good results employing CNNs, with the F1 score of 94–95%. However, CNNs are not widely accessible since they require a large number of samples and specific hardware for training, unlike other machine learning algorithms.

Doblas et al. (2020) suggested a procedure based on Sentinel-1 data, maximum likelihood classification (MLC), and adaptive thresholding (AT) for deforestation detection. They used SAR images acquired over 4 years (from November 2016 to December 2019) and studied the time series of the backscatter coefficients to identify deforested areas in the Brazilian Amazon. They obtained 94% of accuracy with MLC and 96% with AT. However, a comprehensive performance analysis comparing training and validation data was not addressed in that procedure. In our approach, the aim is to assess the classification capability of the NN algorithm to detect deforested areas based on different spatial statistical characteristics of the backscatter coefficient trend. In addition, machine learning algorithms have been proved more appropriate than traditional statistical algorithms for the classification of

remote sensing data (Benediktsson et al., 1990). This work, therefore, presents a method to discriminate deforested areas over the Brazilian Amazon based on NN and Sentinel-1 SAR images. To our best knowledge, the scientific community has not explored this approach to detect near real-time deforestation over the Brazilian Amazon. This paper is organized as follows: Section 2 provides details of the data set and the chosen NN. Section 3 presents the main results obtained, while the results are discussed in Section 4. The concluding remarks are presented in Section 5.

Material and methods

Study area

The study area encompasses part of the municipalities of Altamira, Itaituba, and Novo Progresso, southwest of Pará State, a region with the highest deforestation rates in this state (Figure 3). This region is considered a hotspot in terms of human occupation and is one of the main frontiers of deforestation in the deforestation arch.

Sentinel-1 data set

For this research, we selected Sentinel-1A, Single Look Complex (SLC) images acquired in the Interferometric Wide (IW) swath mode from the European Copernicus program with a free and open data distribution policy

(Open Access Hub, n.d.; Potin et al., 2019). The Sentinel-1A operates at a C-band (5.3 cm wavelength) and a swath width of 250 km (Torres et al., 2012). We selected one image every 12 days, dual-polarization (VV and VH), descendent mode, from the years 2019 to 2018, i.e. a total of 30 images per year (Table 1). The incidence angle ranged from about 29° to 46° and the resolution was about 5 m in range and 20 m in azimuth (ESA, 2021).

The SAR images were pre-processed by means of Sentinel Application Platform (SNAP), an opensource software developed by the European Space Agency (ESA; SNAP Download, n.d.). The preprocessing operations included orbit file correction, thermal noise removal, radiometric calibration (Sigma0), de-burst, and speckle filtering by the Gamma-Map filter. For terrain correction, we used external data of 30-m spatial resolution, obtained from AW3D digital elevation model (DEM) ("ALOS Global Digital Surface Model 'ALOS World 3D – 30 m' (AW3D30)" n.d.). As a result, we obtained images with an approximate spatial resolution of 14.05 m (WGS84, UTM) converted into backscattering coefficients (σ°, units in dB).

Forested and deforested sampling

Table 2 shows the selected Sentinel-2 overpasses from May to October of 2019 that were used to visually select areas without deforestation (FF) and areas with
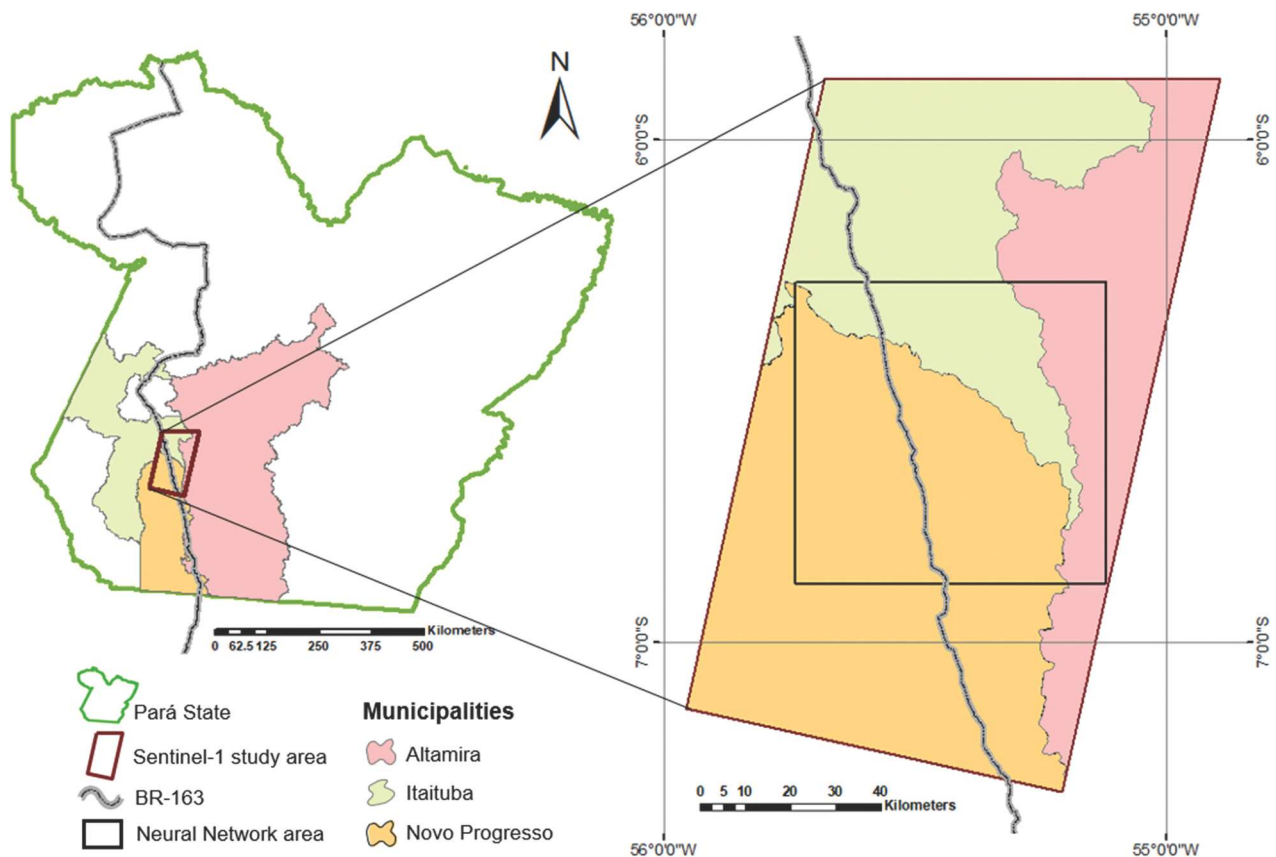

Figure 3. Location of the study area in the Pará State, along the BR-163 highway.

Table 1. Sentinel-1A interferometric wide (IW), single look complex (Level 1) overpasses from 2019 to 2018 considered in this study.

Overspass 2019	Scene Identification 2019	Overspass 2018	Scene Identification 2018
Jan-03	S1A_IW_SLC_1SDV_20190103T092340	Jan-08	S1A_IW_SLC_1SDV_20180108T092333
Jan-15	S1A_IW_SLC_1SDV_20190115T092340	Jan-20	S1A_IW_SLC_1SDV_20180120T092333
Feb-08	S1A_IW_SLC_1SDV_20190208T092339	Feb-01	S1A_IW_SLC_1SDV_20180201T092333
Feb-20	S1A_IW_SLC_1SDV_20190220T092339	Feb-13	S1A_IW_SLC_1SDV_20180213T092332
Mar-04	S1A_IW_SLC_1SDV_20190304T092339	Feb-25	S1A_IW_SLC_1SDV_20180225T092332
Mar −16	S1A_IW_SLC_1SDV_20190316T092339	Mar-09	S1A_IW_SLC_1SDV_20180309T092332
Mar −28	S1A_IW_SLC_1SDV_20190328T092339	Mar-21	S1A_IW_SLC_1SDV_20180321T092332
Apr-09	S1A_IW_SLC_1SDV_20190409T092339	Apr-02	S1A_IW_SLC_1SDV_20180402T092333
Apr-21	S1A_IW_SLC_1SDV_20190421T092340	Apr-14	S1A_IW_SLC_1SDV_20180414T092333
May-03	S1A_IW_SLC_1SDV_20190503T092340	Apr-26	S1A_IW_SLC_1SDV_20180426T092334
May-15	S1A_IW_SLC_1SDV_20190515T092341	May-08	S1A_IW_SLC_1SDV_20180508T092334
May-27	S1A_IW_SLC_1SDV_20190527T092341	May-20	S1A_IW_SLC_1SDV_20180520T092335
Jun-08	S1A_IW_SLC_1SDV_20190608T092342	Jun-01	S1A_IW_SLC_1SDV_20180601T092336
Jun-20	S1A_IW_SLC_1SDV_20190620T092343	Jun-13	S1A_IW_SLC_1SDV_20180613T092337
Jul-02	S1A_IW_SLC_1SDV_20190702T092344	Jun-25	S1A_IW_SLC_1SDV_20180625T092337
Jul-14	S1A_IW_SLC_1SDV_20190714T092344	Jul-07	S1A_IW_SLC_1SDV_20180707T092338
Jul-26	S1A_IW_SLC_1SDV_20190726T092345	Jul-19	S1A_IW_SLC_1SDV_20180719T092339
Aug-07	S1A_IW_SLC_1SDV_20190807T092346	Jul-31	S1A_IW_SLC_1SDV_20180731T092339
Aug-19	S1A_IW_SLC_1SDV_20190819T092347	Aug-12	S1A_IW_SLC_1SDV_20180812T092340
Aug-31	S1A_IW_SLC_1SDV_20190831T092347	Aug-24	S1A_IW_SLC_1SDV_20180824T092341
Sep-12	S1A_IW_SLC_1SDV_20190912T092348	Sep-05	S1A_IW_SLC_1SDV_20180905T092341
Sep-24	S1A_IW_SLC_1SDV_20190924T092348	Sep-17	S1A_IW_SLC_1SDV_20180917T092342
Oct-06	S1A_IW_SLC_1SDV_20191006T092349	Sep-29	S1A_IW_SLC_1SDV_20180929T092342
Oct-18	S1A_IW_SLC_1SDV_20191018T092348	Oct-11	S1A_IW_SLC_1SDV_20181011T092342
Oct-30	S1A_IW_SLC_1SDV_20191030T092349	Oct-23	S1A_IW_SLC_1SDV_20181023T092342
Nov-11	S1A_IW_SLC_1SDV_20191111T092349	Nov-04	S1A_IW_SLC_1SDV_20181104T092342
Nov-23	S1A_IW_SLC_1SDV_20191123T092348	Nov-16	S1A_IW_SLC_1SDV_20181116T092342
Dec-05	S1A_IW_SLC_1SDV_20191205T092348	Nov-28	S1A_IW_SLC_1SDV_20181128T092341
Dec-17	S1A_IW_SLC_1SDV_20191217T092347	Dec-10	S1A_IW_SLC_1SDV_20181210T092341
Dec-29	S1A_IW_SLC_1SDV_20191229T092347	Dec-22	S1A_IW_SLC_1SDV_20181222T092341

deforestation (FD). We collected samples over homogeneous areas (at least 90%) in terms of primary forest and clear-cut deforestation, located in flat topography. The presence of forest was guaranteed by evaluating Sentinel-2 images from 2018 to 2020 (25 August 2018 image and 20 June 2020). The 98 FF samples presented an average size of 95 pixels, while the 199 FD samples presented an average size of 66 pixels (Figure 4).

For each FF and FD sample, the mean, standard deviation, and maximum-minimum difference (MMD), that is the difference between the maximum and minimum value of the backscatter coefficient,

Table 2. Forest–Deforested and Forest–Forest samples (FD) manually collected based on Sentinel-2 images acquired in 2019.

Time interval	Number of samples FD	Number of samples FF
May 7–June 16	58	
Jun 16–Jun 21	1	
Jun 21–Jun 26	8	
Jun 26–Jul 16	35	
Jul 16–Jul 21	15	
Jul 21–Jul 31	21	
Jul 31–Aug l0	16	
Aug 10–Aug 20	10	
Aug 20–Aug 30	14	
Aug 30–Sep 9	8	
Sep 9–Sep 19	13	
Sep 19–Oct 9	1	
Total	199	99

were calculated for both VH and VV polarizations. The metrics were computed over the polygons for each acquisition in the year 2019. Figure 5 shows an example of each statistical parameter for FF and FD areas in the VH and VV polarizations. For every acquisition, shown on the horizontal axis, the related statistical value is reported on the y-axis. In this way, the variation of the statistical parameter throughout the year can be obtained and used to discriminate the forested area from the deforested area.

Multi-layer perceptron (MLP)

An artificial NN may be viewed as an adaptive model of nonlinear parallel processing units massively interconnected. The NNs are capable of acquiring knowledge from the surrounding environment through a process of learning which modifies the interconnection weights between the units. Therefore, NNs can learn from the training examples by constructing input-output mappings. This learning ability allows NNs to generalize, i.e. to produce good approximations of outputs from inputs not found during the learning phase (Haykin, 2009). The processing unit is the elementary block of the NNs, which is mainly characterized by its activation function. The latter is essential in NNs because it adds the non-linearity that makes them capable of learning complex patterns (Sharma et al., 2020).
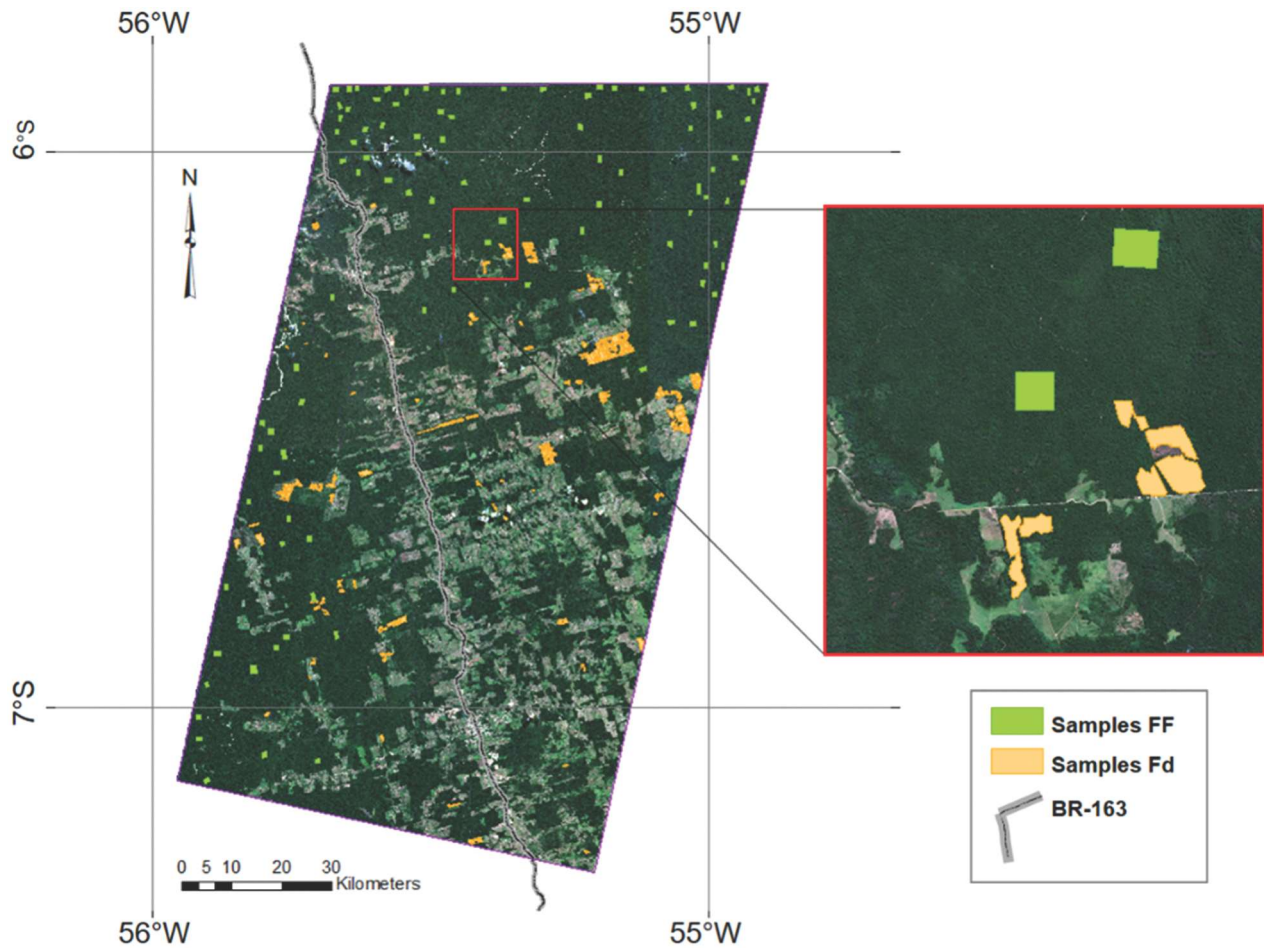
Figure 4. Example of Forested–Forested (FF) and Forested–Deforested (FD) samples manually collected in different overpasses of Sentinel-2 satellite, overlaid on the RGB color composite of bands 4, 3, and 2 of Sentinel-2 satellite image obtained in 1 July 2019.

NNs can be distinguished by their architectures or structures. In this study, we considered the MLP. MLP is a feedforward NN, i.e. the input is projected unidirectionally to the output, which is distinguished by the presence of one or more hidden layers between the input and output layers. MLPs are applied in classification and regression problems in many fields, including remote sensing (Ramchoun et al., 2016). Since we implemented a binary classifier, a sigmoid activation function was used for the final layer. It outputs a value between 0 and 1 that can be treated as a probability that the given input belongs to a particular class (Sharma et al., 2020).

The number of hidden layers and units depends on the specific problem and cannot be determined a priori (Ramchoun et al., 2016). In this study, we applied two hidden layers of units between the input vector with the measured features and the output vector with the classification response (Del Frate & Solimini, 2004). The initial number of units was estimated following the study conducted by Del Frate and collaborators and was defined for each specific case. The MLP topology consists of four layers (Figure 6). As discussed in detail in Section 2.5, four case studies with different input configurations were analysed. Therefore, we designed four MLP topologies with the number of input and hidden units varying depending on the case study.

Data set preparation

The statistical features extracted from the FD and FF sample areas were inputs to the NN, trained to automatically detect the probability that an area was deforested. Different case studies were considered to form the input vectors. First, the statistical parameters were involved individually, and then a combination of them was considered. Specifically, four different sets of inputs were chosen:

(1) mean $\sigma°$ values of both VV and VH polarizations;
(2) mean $\sigma°$ values and corresponding standard deviation of both VV and VH polarizations;
(3) mean $\sigma°$ values and corresponding MMD values of both VV and VH polarizations; and
(4) mean $\sigma°$ values and corresponding standard deviation and MMD of both VV and VH polarizations.
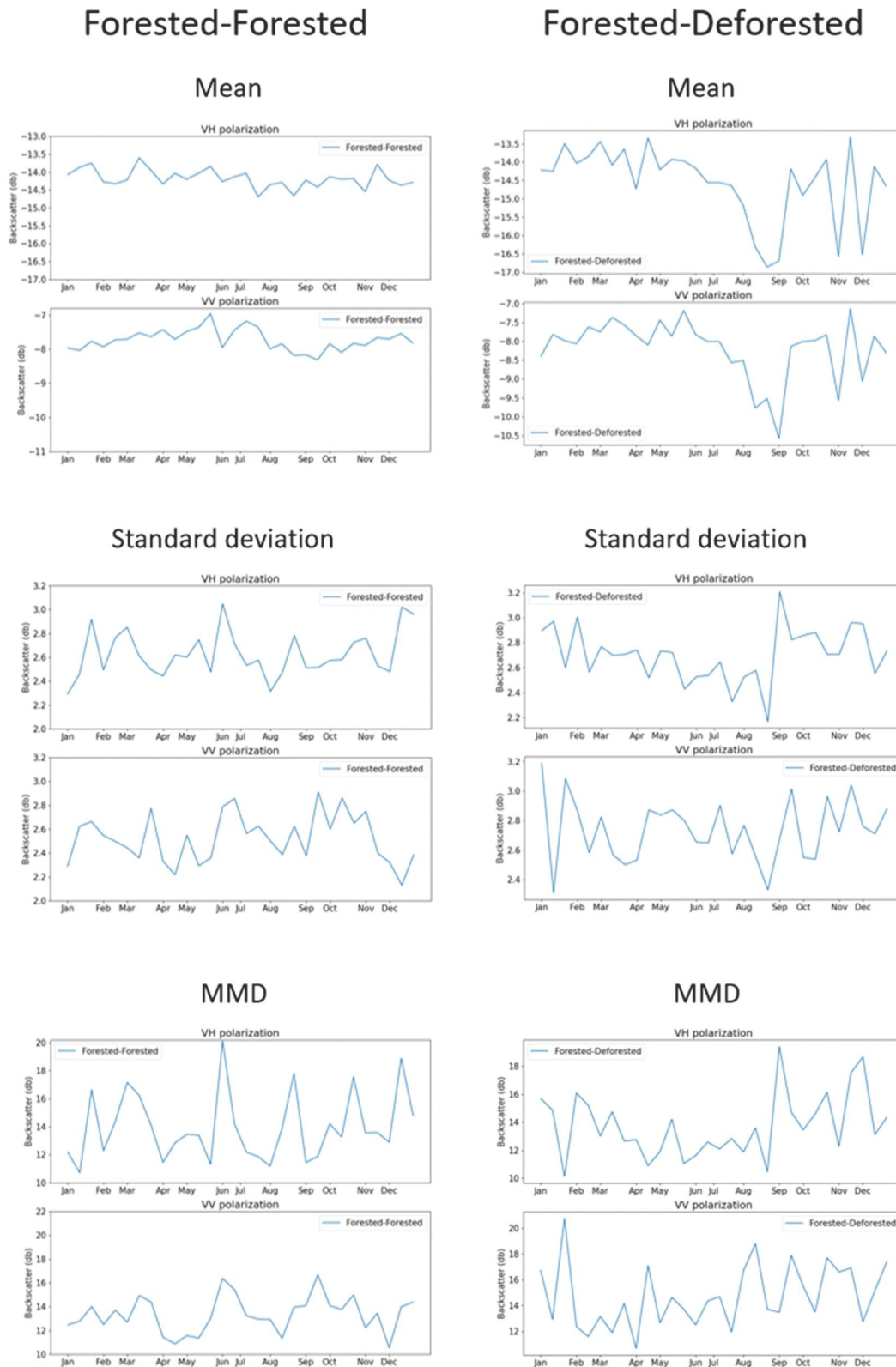
Figure 5. Mean, standard deviation, and MMD (maximum-minimum difference) example of the backscatter coefficient in VH and VV polarizations.

Standard deviation and MMD were not considered individually as they did not exhibit good performances. Similarly, preliminary results obtained with single polarization configurations suggested disregarding such an option. Figure 7 shows the processing procedure, which is the same for the four case studies.

As a first step in the data set construction, the number of samples related to the FF condition was equalized to the FD ones by increasing the former through a data augmentation process. More specifically, synthetic data (noisy data) was generated from the original data (seeds) by adding slightly modified copies of them.
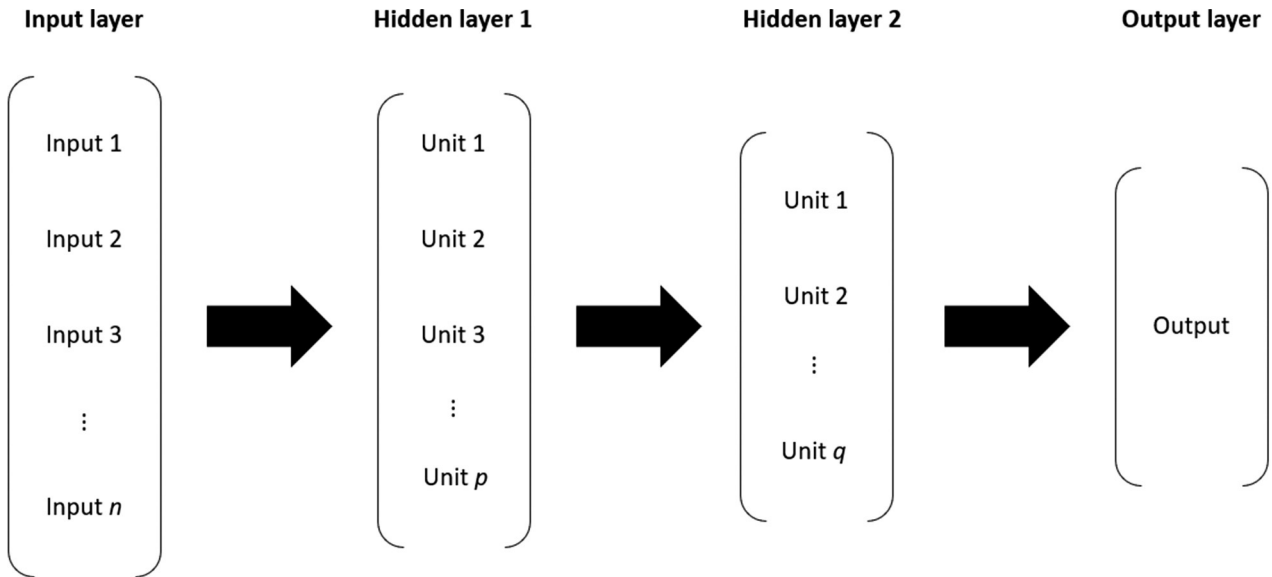
Figure 6. Multi-Layer Perceptron topology, n, p, and q represent the total number of units in the input and hidden layers that change accordingly in the considered case study.
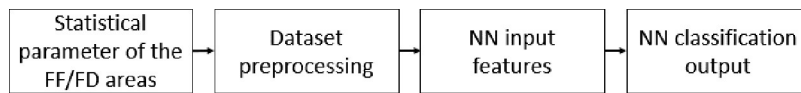

Figure 7. Block diagram showing the processing procedure.

Random noise vectors of the same size as the seeds vectors were created according to a Gaussian distribution with specific mean and variance. These two parameters were chosen due to the required similarity between the noisy vector and the original one. For the first case study, where only the mean $\sigma°$ values are considered, an example of a noise vector is shown in Figure 8(a). It consists of 30 elements, as the number of features in case study (1) in the VH polarization only. The noise values range approximately from −0.3 to 0.3.

The sum of the noise vector and the original seed vector is shown in Figure 8(b) for the average value of the backscatter. The original vector is shown in orange, while the noisy one in blue.

To have a data set of sufficient size to train the NN, the whole number of input samples (both FD and FF samples) was increased in a similar way. The data set generation results for the case study (1) (average value of the backscatter coefficient) are shown in Table 3. In this case, the data set was enlarged five-fold to obtain
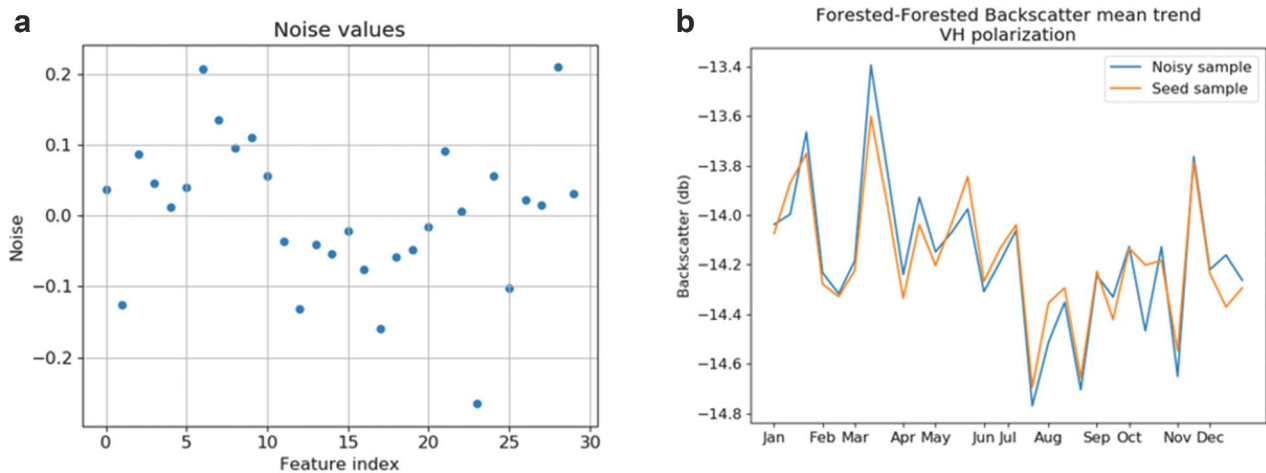

Figure 8. Random noise values generated (a) and the "seed" (shown in Orange) and noisy (shown in blue) samples for VH polarization (b).

Table 3. Training data set description after augmentation (case study 1: mean σ° values).

Parameters	Forested–Deforested (FD)	Forested–Forested (FF)
Number of acquisitions per year	30	30
Polarizations	VH and VV	VH and VV
Number of areas (for each acquisition)	199	98 x 3 = 294 (199 selected)
Augmented number of areas	199 x 5 = 995	199 x 5 = 995
Number of samples	199 + 995 = 1194	199 + 995 = 1194

Table 4. Description and number of the case study features. MMD = maximum-minimum difference.

Case study	Features	Total number of features
1	30 mean VH + 30 mean VV	60
2	30 mean VH + 30 SD VH + 30 mean VV + 30 standard deviation VV	120
3	30 mean VH + 30 MMD VH + 30 mean VV + 30 MMD VV	120
4	30 mean VH + 30 standard deviation VH + 30 MMD VH + 30 mean VV + 30 standard deviation VV + 30 MMD VV	180

Table 5. Train, validation, and test set distribution for the case study (1).

Sampling sets	Forested–Deforested	Forested–Forested	Total
Train set	895	895	1790
Validation set	179	179	358
Test set	120	120	240
Total	1194	1194	2388

a total number of samples equal to 1194 + 1194 = 2388. Since the statistical features differ significantly, each sample was normalized between 0 and 1 before being input to the NN.

Each sample in the data set is described by features related to the backscatter coefficient in the VH and VV polarizations. The number of features for each sample depends on the case study: for the case study (1), the features are 60 (30 VH + 30 VV features); for the case studies (2) and (3), they are 120 (60 VH + 60 VV features); and for the case study (4), they are 180 (90 VH + 90 VV features). Table 4 provides a summary of this split. Thus, the input of the NN is a vector with the number of entries that is equal to the number of features. Since the features differ significantly, each sample was normalized between 0 and 1.

Training phase (2019 data set)

Generally, in machine learning models, the data set is divided into three distinct parts: training, validation, and test data sets split into the proportion of 75%, 15%, and 10%, respectively. These proportions are a typical choice in machine learning data separation (Haykin, 2009). The training and validation sets are used during the training process, while the test set is used to evaluate the performance achieved. Indeed, the test set is used separately from the previous ones and is not involved in the learning procedure. In this paper, these proportions were considered for all case studies. The sample division for the first case study is reported in Table 5.

During the supervised learning process, the connection weights are optimized to minimize the error, namely the difference between the desired response and the actual response, according to a loss function. This error is evaluated both on the training and validation sets, which consists of examples not belonging to the training one. To avoid overfitting problems, i.e. to make the NN able to generalize over new patterns, the training of the network is stopped when the error on the validation data set reaches its minimum, according to the early stopping algorithm (Prechelt, 1998).

The number of units in the hidden layer was optimized for each input configuration, in terms of classification accuracy and generalization capability. Several attempts were made to select the proper number of units in the hidden layers which finally led to the topologies summarized in Table 6.

Evaluation of the 2018 data set

The NN capability achieved during the training phase is applied to novel input data. The trained model is used for the automatic recognition of areas deforested during the year 2018. The properties of the data set used in this phase are similar to those of the training data set: it was composed of 30 pre-processed Sentinel-1 images acquired over the same area with the same spatial resolution, which shows the σ° values for the VH and VV polarizations.

Each image of the time series was automatically divided into sub-images with a size of 10 × 10 pixels, resulting in 223,725 patches for each acquisition. Considering the pixel resolution of the S1 images of 14.05 m, 10 pixels × 10 pixels makes an area of approximately 2 ha. Table 7 shows an overview of the data set dimension. The statistical parameters were calculated for each patch for both polarizations, as described in Section 2.5, and the same four case studies were considered. Therefore, the input of the trained NN is a vector with a number of entries depending on the examined case study.

Table 6. MLP topology for each case study.

Case study	Number of units in the input layer	Number of units in the first hidden layer	Number of units in the second hidden layer	Number of units in the output layer
1	60	20	5	1
2	120	30	5	1
3	120	30	5	1
4	180	40	10	1

Table 7. Data set description of selected Sentinel-1 images from 2018.

Parameter	Specification
Number of acquisitions per year	30
Number of patches (for each acquisition)	223,725
Polarizations	VH and VV

Results evaluation

The sigmoid activation function in the NN output layer returns a class probability in the interval $[0, 1]$. A predicted value equal to or close to 0 means that the model identifies an area as forested (FF); conversely, a prediction equal to or close to 1 indicates a deforested area (FD). To evaluate the results, the confusion matrix was computed, and accuracy, precision, recall, and F1 score were derived. They are defined as (Equations 1–4):

$$Accuracy = \frac{TP + TN}{TP + FP + TN + FN} \qquad (1)$$

$$Precision = \frac{TP}{TP + FP} \qquad (2)$$

$$Recall = \frac{TP}{TP + FN} \qquad (3)$$

$$F1 = 2 \times \frac{Precision \times Recall}{Precsion + Recall} \qquad (4)$$

Where:

TP = True positives, i.e. the number of deforested areas classified as deforested.

TN = True negatives, i.e. the number of forested areas classified as forested.

FP = False positives, i.e. the number of forested areas classified as deforested.

FN = False negatives, i.e. the number of deforested areas classified as forested.

Results

Figure 9 shows an example of the multitemporal backscattering coefficients from an area that faced clear-cut deforestation between 7 May 2019 (a) and 16 June 2019 (c) for both VH (b) and VV (d) polarizations. The backscatter signal of deforestation presents a short increase followed by a sharply decreased in both polarizations until approximately 3 months (roughly, 31 August 2019). Then, the signals tended to increase after September.

From all FD samples collected in 2019, an average decrease of the mean backscatter coefficients of approximately 2 dB for VV polarization and 2.3 dB for VH polarization can be observed after deforestation. This decrease in the backscatter signal remains evident for the next 3–4 months approximately. After this period, we observed an irregular increase in both polarizations.

2019 data set

Table 8 reports the results achieved for the four case studies for the data sets obtained in 2019. The mean, standard deviation, and MMD input set showed accuracy and F1 score of 99%. The other case studies also achieved promising results: the accuracy obtained using mean and MMD slightly decreased to 98%. Lastly, mean and standard deviation, as well as mean, only showed an accuracy of 97%. False positives and false negatives were also very low. They were evaluated through the F1 metric, which is the harmonic mean of precision and recall. This means that the algorithm avoids, to a great extent, false alarms and, in most cases, does not miss the deforested areas.

2018 data set

To assess the NN performance, the 2018 results were validated using two ground truth images provided by the MapBiomas and PRODES projects. MapBiomas produces annual LULC maps by applying Random Forest classification overall Landsat scenes acquired in a specific year. The LULC maps are pixel-based, with a minimum mapping area of 1 ha. PRODES provides the annual rates of clear-cut deforestation with a minimum mapping area of 6.25 ha. PRODES makes use of moderate spatial resolution from Landsat-8, CBERS-4, and Sentinel-2 with 30 m, 20 m, and 10 m of spatial resolutions, respectively.

The data from MapBiomas and PRODES considered only deforested areas from 2018 found in the same region of the Sentinel-1 data set. The ground truth images were clipped into patches with the size of 10 pixels × 10 pixels, following the image division used for the SAR data set obtained in 2018. Each patch in the ground truth image is geographically related to the patch in the Sentinel-1 imagery in the data set. Out of the total, the ground truth patches reporting areas deforested in 2018 represent approximately 0.3% in MapBiomas while in PRODES they represent 0.6%.

The predictions related to 2018 deforested patches were collected, and the same number of predictions related to forested patches is selected randomly from the total to create a well-balanced data set. Table 9 shows the results achieved for the 2018 images for the four case studies.

Compared with the results obtained in 2019, all evaluation parameters decreased for the data sets obtained in 2018, especially for the recall, due to the relatively high number of false negatives. The recall decreased for the PRODES data. For both reference
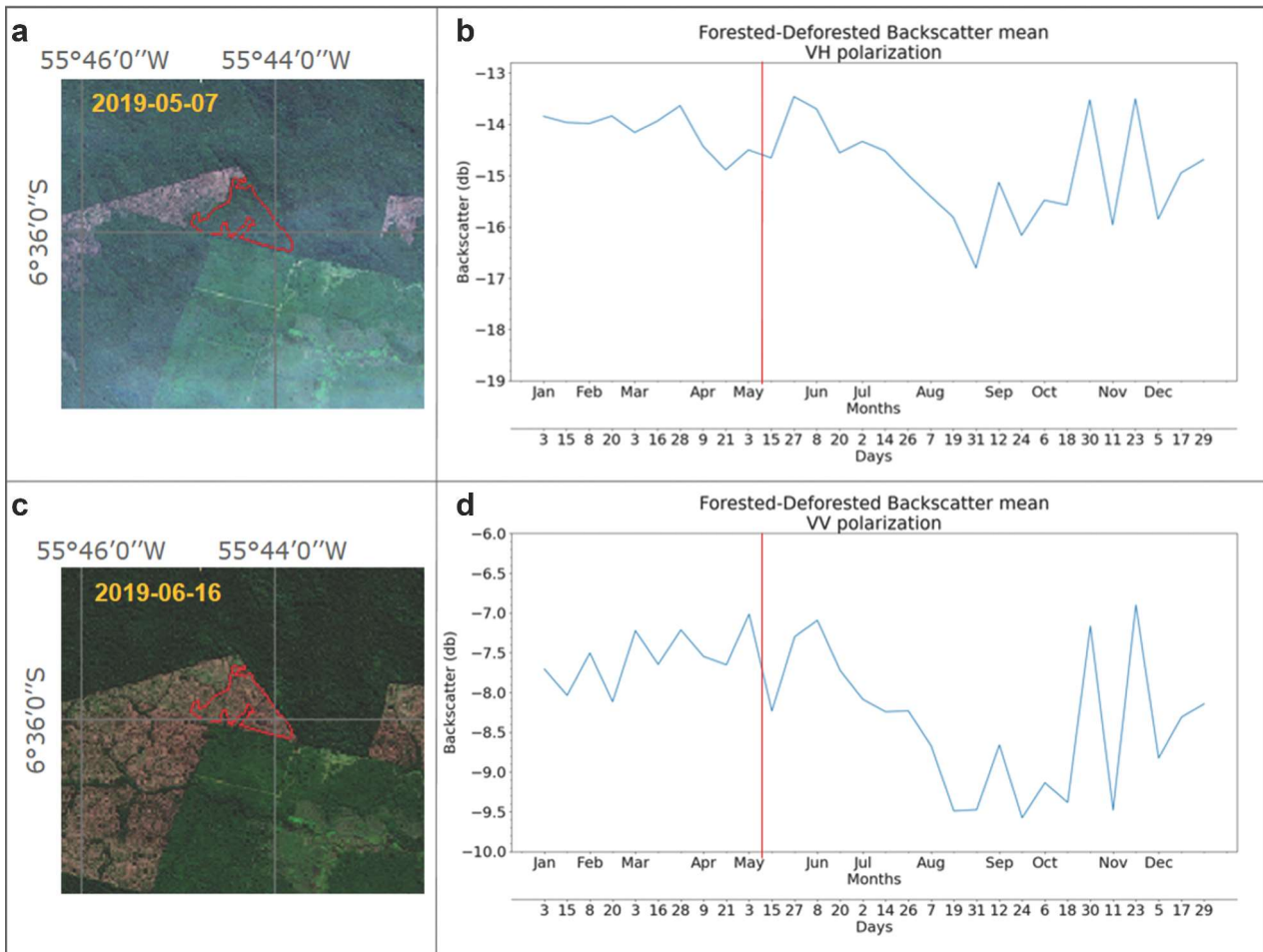
Figure 9. Left: Example of a deforested area in the study area shown by the Sentinel-2, RGB color composites of bands 4, 3, and 2 acquired on 7 May 2019, and 16 June 2019. Right: Sentinel-1 mean backscatter coefficients along the year 2019 in the VH and VV polarizations. The red line highlights the backscatter position coincident with the first data of the optical image before deforestation.

Table 8. Statistical results for the data sets obtained in 2019. MMD = maximum-minimum difference.

Statistical parameters	Accuracy	Precision	Recall	F1
Mean	0.97	0.98	0.97	0.97
Mean + standard deviation	0.97	0.99	0.94	0.97
Mean + MMD	0.98	0.96	0.99	0.98
Mean + standard deviation + MMD	0.99	0.99	0.98	0.99

data, the best-case scenario corresponded to the case study that considered mean, standard deviation, and MMD as input. In this case, the model achieved accuracy and F1 score of 89%, with a low number of false positives and false negatives, validating with the MapBiomas ground truth image and accuracy and F1 score of 81 and 79%, respectively, with the PRODES ground truth. The second best case was obtained for the mean backscatter coefficient as input parameter. The model performance declined when mean and standard deviation and mean and MMD were considered.

Discussion

In this study, we proposed a method based on NNs that detects deforested areas by analysing the annual trend of specific statistical parameters related to the backscatter coefficients obtained from Sentinel-1 images. Different statistical parameters, i.e. different case studies including mean, standard deviation, and MMD of the backscatter coefficient in VH and VV polarizations were considered. This method analysed 2 years of data sets: 2019 and 2018. Areas deforested in 2019 were manually selected, labelled, and used to train and test the algorithm, while the trained NN automatically identified areas deforested in 2018.

Figures 10, 11, 12, and 13 represent samples extracted from the 2019 data set. Figures 10 and 11 report two FF areas, while Figures 12 and 13 report FD areas. On the left, the figures illustrate the RGB colour composites (a, c) obtained from Sentinel-2 2019 images. The right shows the related mean backscatter trend in both VH (b) and VV (d) polarizations.

Table 9. Statistical results for the ground truth data sets obtained in 2018. SD = standard deviation. MMD = maximum-minimum difference.

Parameter	MapBiomas				PRODES			
	Accuracy	Precision	Recall	F1	Accuracy	Precision	Recall	F1
Mean	0.85	0.88	0.81	0.85	0.79	0.87	0.67	0.76
Mean + SD	0.88	0.96	0.79	0.87	0.78	0.95	0.58	0.72
Mean + MMD	0.85	0.87	0.82	0.85	0.76	0.84	0.64	0.73
Mean + SD + MMD	0.89	0.90	0.89	0.89	0.81	0.88	0.73	0.79

The VV and VH signals from the Forested–Forested samples (depicted in Figures 10 and 11) show regularity of the signal for both polarizations with the mean backscatter signal values from −14.2 dB for VH and −7.7 dB for VV polarizations. When deforestation occurs, the VV and VH backscatter signals are perturbed. After deforestation, it was observed a short increase of the backscatter signal before a more pronounced decrease. From all samples collected, we observed an average decrease of 2.3 dB for VH and 2 dB for VV polarizations. The decrease was evident and lasted from about 3 to 4 months. Some authors have observed the increase and decrease of the backscatter signal after deforestation (Bouvet et al., 2018; Doblas et al., 2020; Hoekman et al., 2020; Joshi et al., 2015; Kellndorfer, 2019; Reiche et al., 2018a, 2018b).

Reiche et al. (2018a) found a decrease of 2.0 dB in VH after deforestation in the province of Riau, Indonesia, through Sentinel-1 C-band SAR data time-series. Reiche et al. (2018b) observed a decrease of 2.5 dB, using VV time-series of Sentinel-1, from deforestation studies in the province of Santa Cruz, Bolivia.

Bouvet et al. (2018) stated that the C-band SAR backscatter signal over cleared or burned areas presents a lower backscatter signal of ~2.5 dB in the Amazon rainforest in Peru. Decrease backscattering was also observed for the majority of our deforested areas collected in 2019.

Hoekman et al. (2020) reported that, in general, undisturbed forests have a relatively high and stable backscatter level; therefore, a significant decrease in backscatter level would indicate deforestation. The backscatter of clear-cut areas, in both polarizations, is
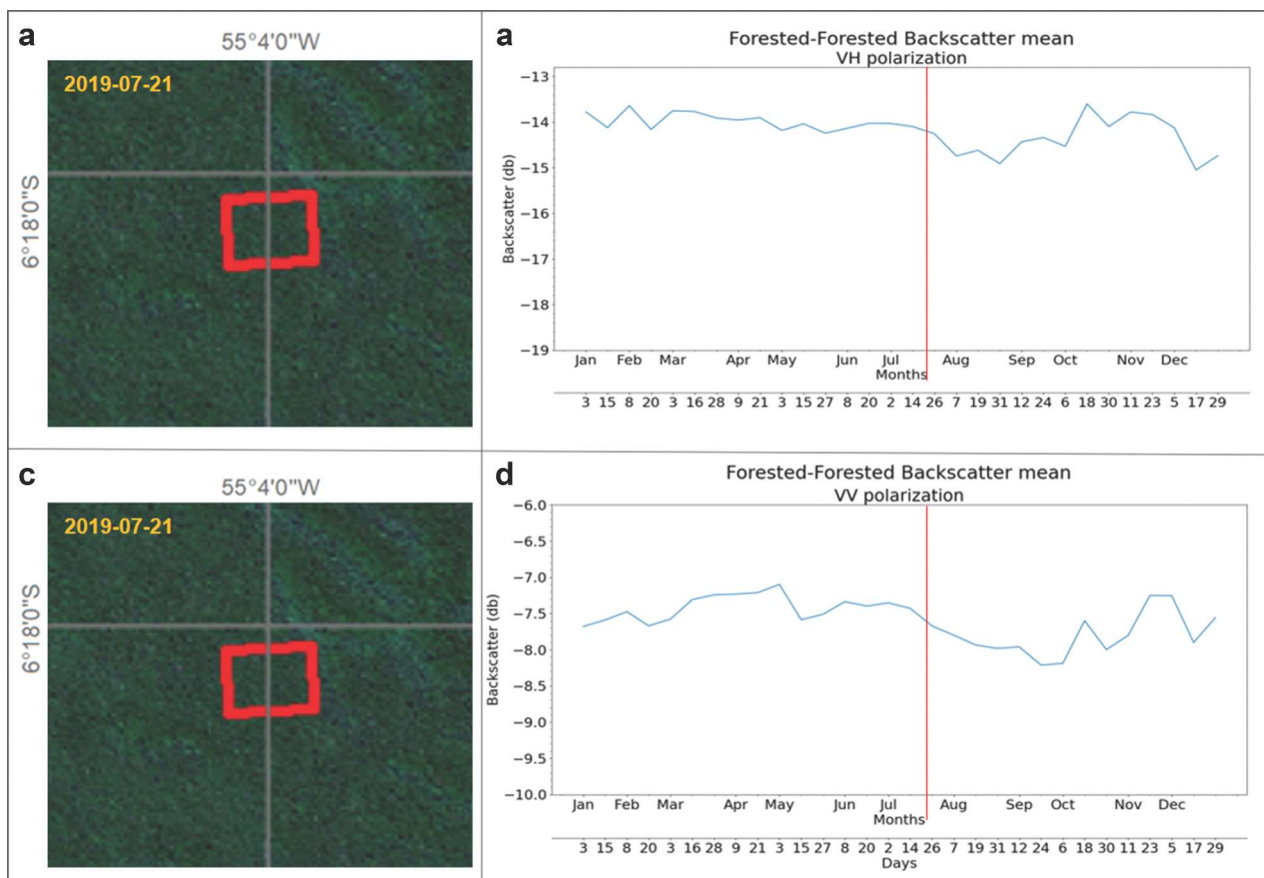
Figure 10. Sentinel-2 RGB colour composite (a, c) acquired on 21 July 2019 of a Forested–Forested sample (highlighted in red), and backscatter mean trend in VH (b) and VV (d) polarizations. The red line highlights the backscatter position coincident with the data of the optical image.
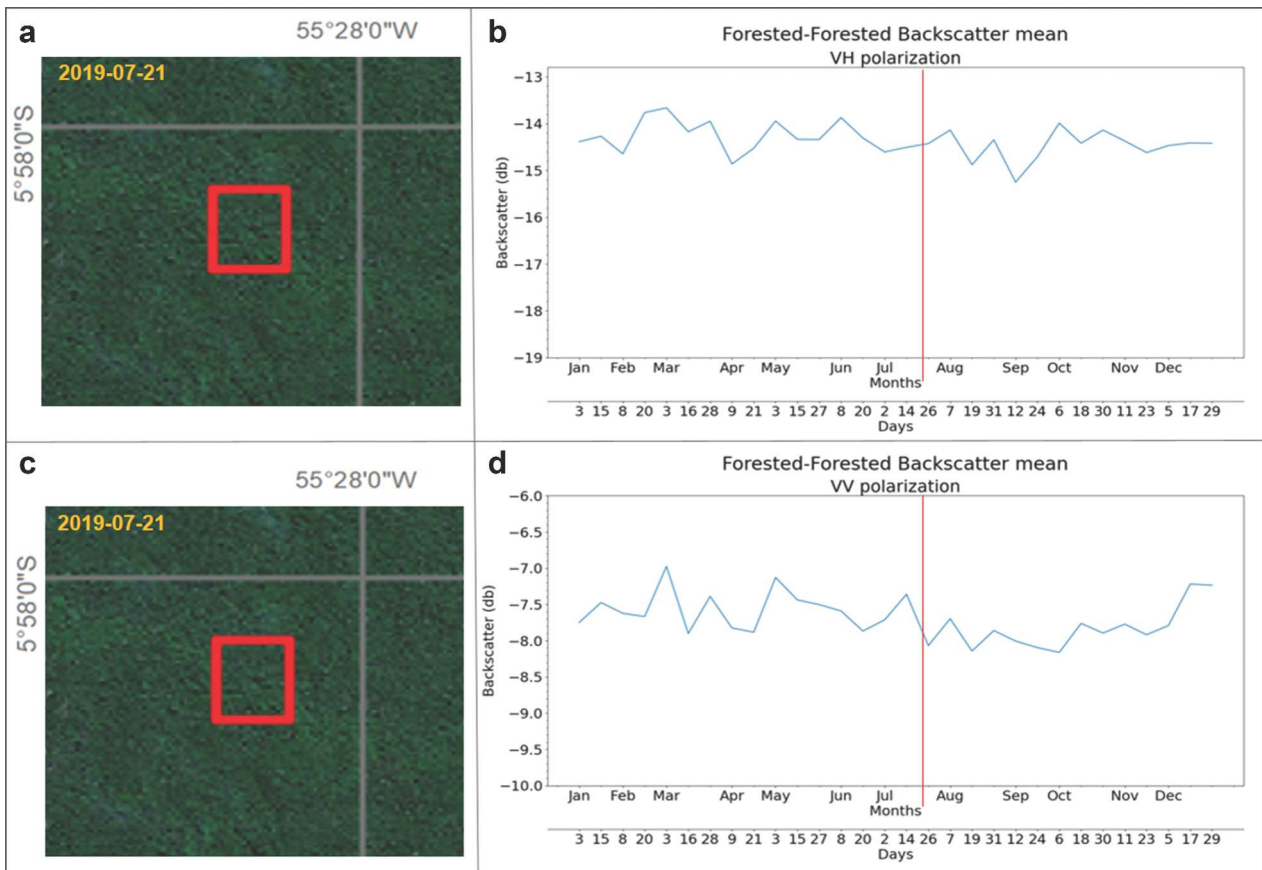
Figure 11. Sentinel-2 RGB colour composite (a, c) acquired on 21 July 2019 of a Forested–Forested sample (highlighted in red), and backscatter mean trend in VH (b) and VV (d) polarizations. The red line highlights the backscatter position coincident with the data of the optical image.

usually 2.0 dB lower than the original forest cover. However, remaining debris and undergrowth, terrain slopes, soil roughness, and soil moisture may intensify the decrease. The rainforest site in the Indonesian province of Central Kalimantan and in the Pará State, Brazil, Hoekman et al. (2020) observed that VH and VV signals go up and down, and deforestation was characterized at the first moment the signal goes down.

Joshi et al. (2015) revealed an L-band backscatter decrease of 1.1 dB in VH after clearing full forest cover events in the region of Madre de Dios in Peru.

Doblas et al. (2020), in a study in the Amazon rainforest, determined the mean backscattering values of the forest as −12.4 and −6.25 dB for VH and VV polarizations, respectively, while the mean backscattering values of the deforested series are consistently lower, reaching −13.1 and −7.6 dB for VH and VV polarizations.

For the 2019 test data set, the NN model achieved high performance in all case studies. This was due to the manual selection and labelling of the test areas employing the RGB composition of Sentinel-2 images. For the 2018 data set, the performance decreased, as shown in Figure 14 that reports the trend of the F1 metric for the four case studies from 2019 to 2018 images.

To investigate the 2018 results, three deforested areas among the largest ones in the ground truth images were analysed. Figures 15, 16, and 17 show the three areas. Each RGB color composition shows the areas captured by the Sentinel-2 satellite from April to July of 2018. These figures highlight the differences in land cover changes due to the clear-cutting process. At the bottom, the figures represent the ground truth images and the classification made by the MLP for the MapBiomas (b), (c), and PRODES (d), (e) ground truths. In the ground truth images (b) and (d), the areas deforested in 2018 are shown in white, areas forested are shown in black, and areas deforested before 2018 are in grey. The classification images (c) and (e) show the patches as they were classified overlapped to the ground truth image.

The F1 score differences between the PRODES and MapBiomas ground truth images may be related to the resolution employed by the two projects. The coarser PRODES resolution does not capture small deforested areas that are considered in the MapBiomas ground truth. Indeed, PRODES does not capture small forested areas inside a deforested polygon. This can explain the difference in Recall, due to the number of false negatives

between the two ground truth images. A large number of false negatives are localized in the small areas detected by the MapBiomas. Moreover, the misclassification may be caused by the deforestation method. After clear-cutting, the trees are left on the ground for drying before being burned. Since the amount of biomass remains the same, the result is somehow similar in backscatter values compared with intact forest areas. Bouvet et al. (2018), Kellndorfer (2019), and Hoekman et al. (2020) observed these trends.

Bouvet et al. (2018) reported that large branches remaining in the ground can cause a double-bounce scattering mechanism and mask the decrease of the backscatter signal. The authors also stated that, after rainfall events, the backscatter signals can exhibit the same values as intact forests.

Kellndorfer (2019) stated that if deforestation results in rough soil conditions (e.g. slash) backscatter can be significantly enhanced until logs are removed. The authors declared yet that, after deforestation, there is a dominant change from volumetric scattering to surface scattering, with an expected decrease in the cross-polarized (VH, HV) signal.

Hoekman et al. (2020) reported that deforestation in Brazil often is the slash-and-burn type of small scale, and in most instances, the deforestation is preceded by severe degradation.

Figure 18 shows examples of test sites from the Amazon forest, with slashed trees after 3 months of drying (A). As it can be seen, the site conserves all the previously standing biomass but with dried leaves and trunks. The green leaves are from liana vines that grew along with the slashed biomass (Soares Neto et al., 2009). Figure 18 also shows how a clear-cut site appears after the cleaning fire (B). Small branches and leaves are combusted to completion, while large trunks are only partially consumed (Christian et al., 2007). Long ash trails indicate trunks, mostly palm trees that were completely consumed through smouldering. However, misclassification may be associated with the deforestation method.

In this study, we implemented a new methodological flow based on Sentinel-1 data and MLP classifier capable of detecting deforestation automatically in the Amazon rainforest. The accuracy was in the range of 81% to 89%, depending on the considered
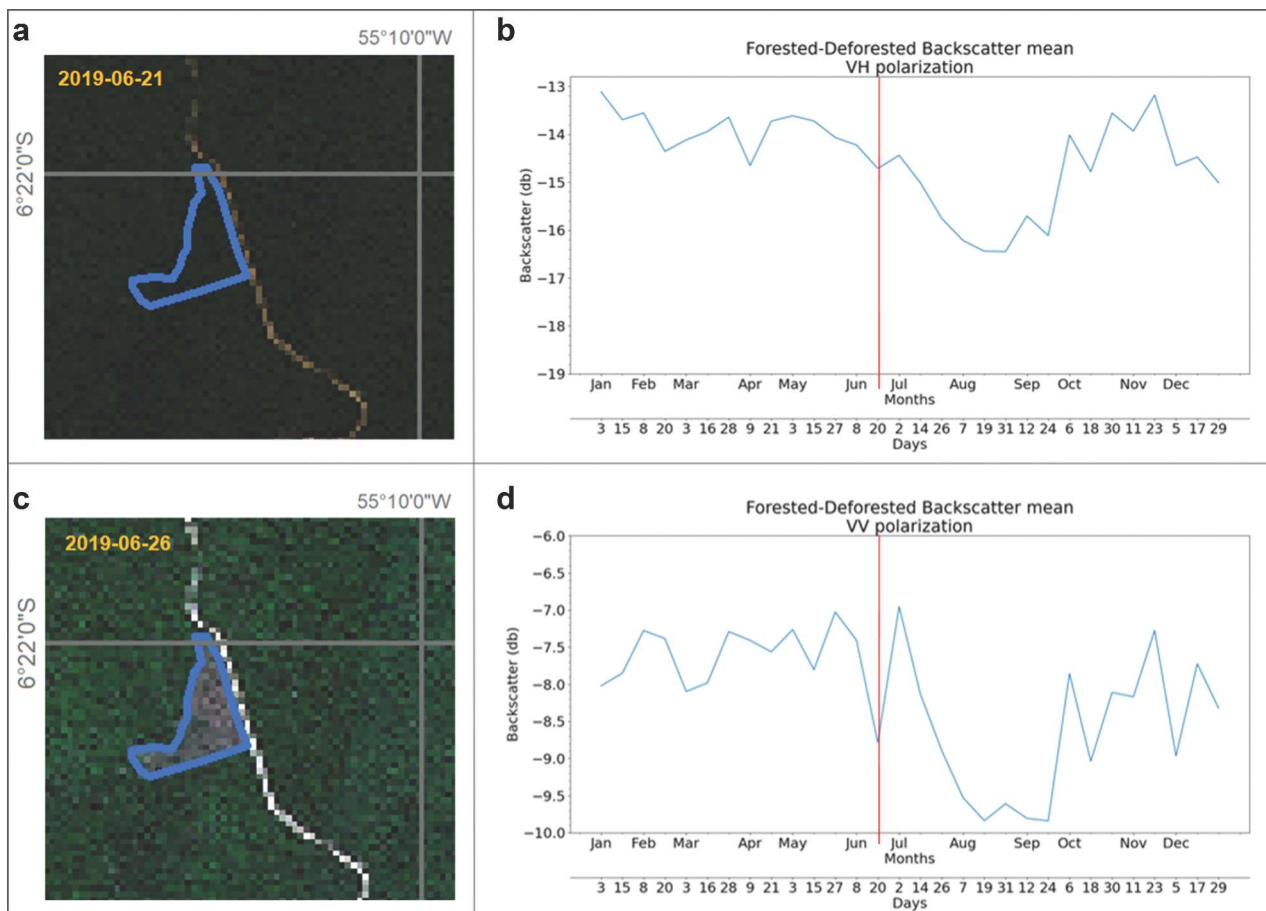

Figure 12. Sentinel-2 RGB colour composite acquired on 21 June 2019 (a) and 26 June 2019 (c) of a Forested–Deforested sample (highlighted in blue), and backscatter mean trend in VH (b) and VV (d) polarizations. The red line highlights the backscatter position coincident with the first data of the optical image before deforestation.
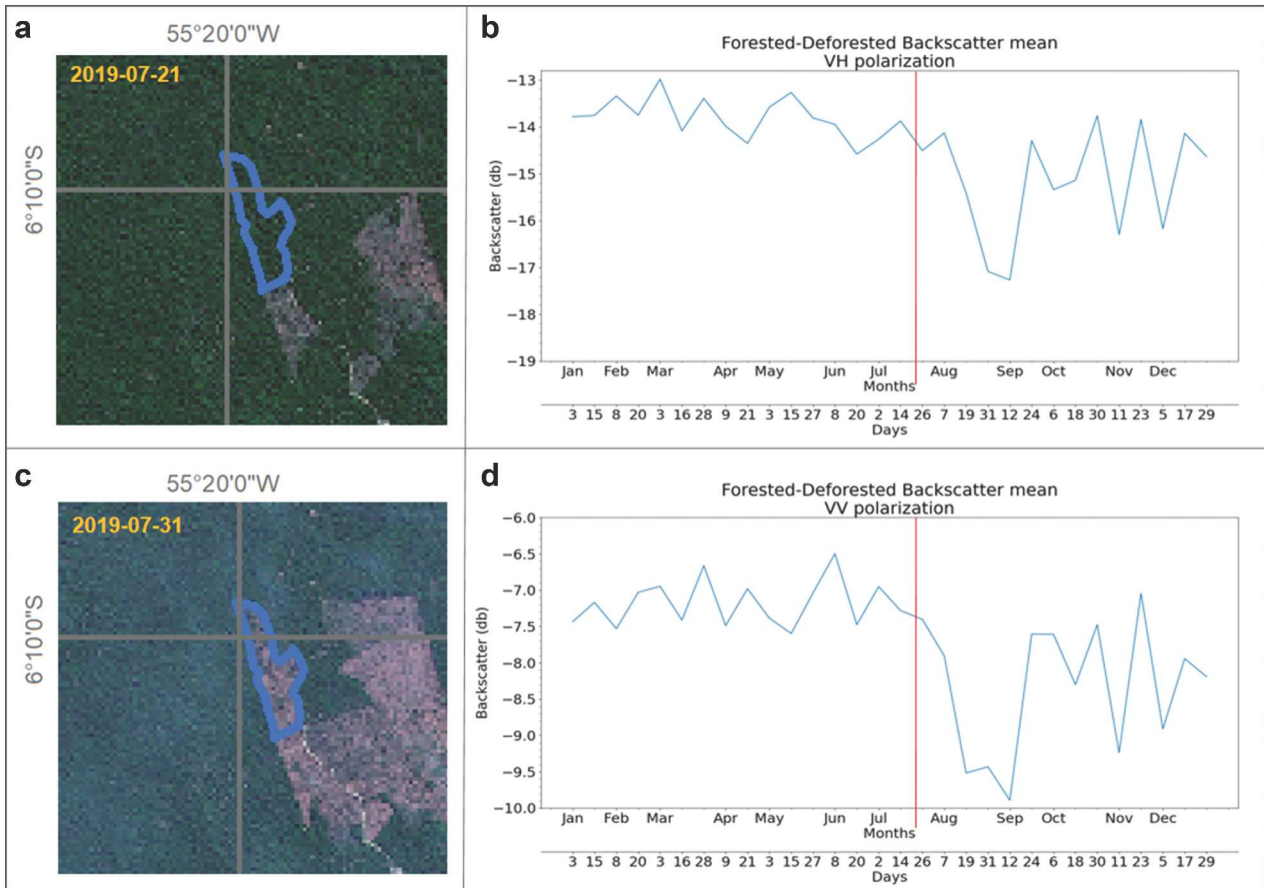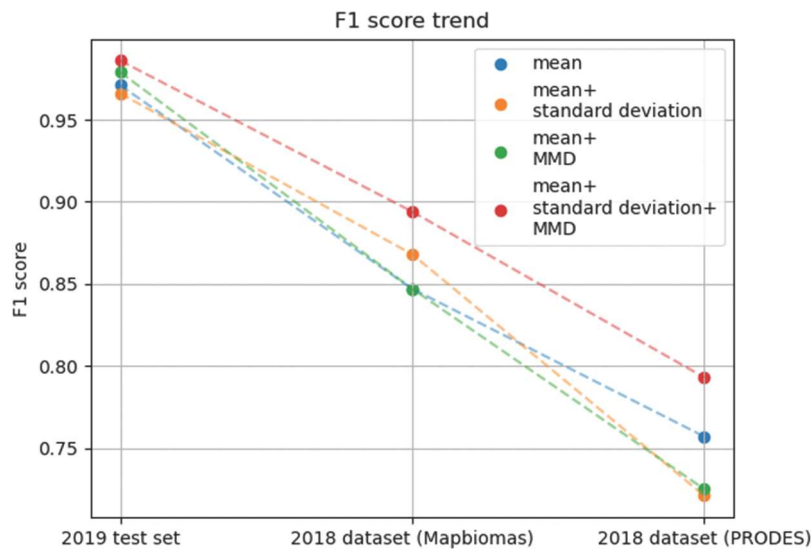
Figure 13. Sentinel-2 RGB colour composite acquired on 21 July 2019 (a) and 31 July 2019 (c) of a Forested–Deforested sample (highlighted in blue), and backscatter mean trend in VH (b) and VV (d) polarizations. The red line highlights the backscatter position coincident with the first data of the optical image before deforestation.

Figure 14. F1 variation for the 2019 test set and 2018 data set for both ground truth images.

reference image. In hand-picked areas used for training the NN, the accuracy reached 99%, comparable to those achieved by Bem et al. (2020), whose accuracy reached 94%. Bem et al. (2020) combined optical images and NN for detecting deforestation. The method, however, could only be applied in the

dry season of the Amazon rainforest, which lasts for about 6 months. Methods based on radar data can be used throughout the year.

Doblas et al. (2020), which research is based on radar data, reached maximum accuracy of 96% in detecting deforestation. Our results are 2% higher
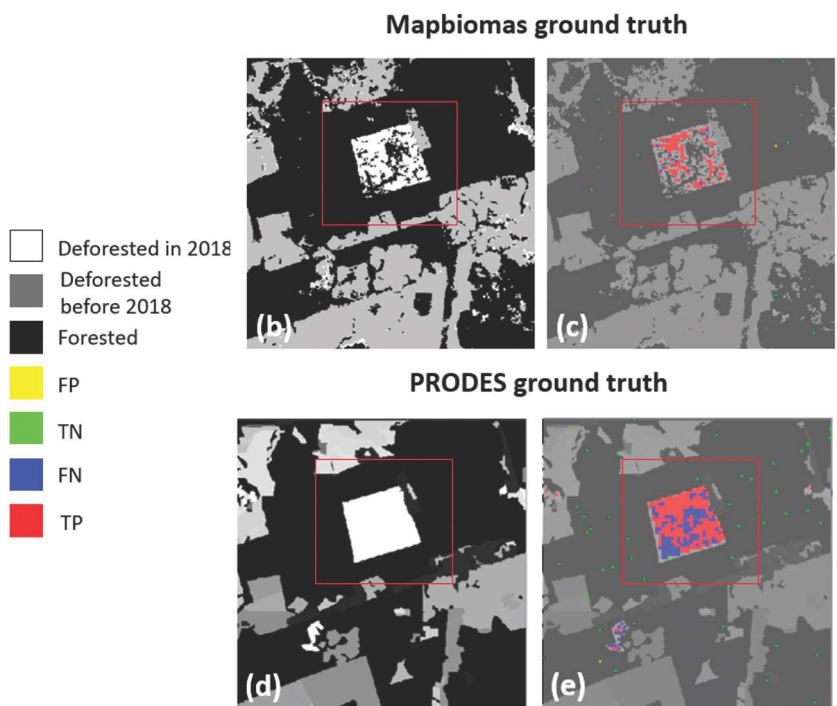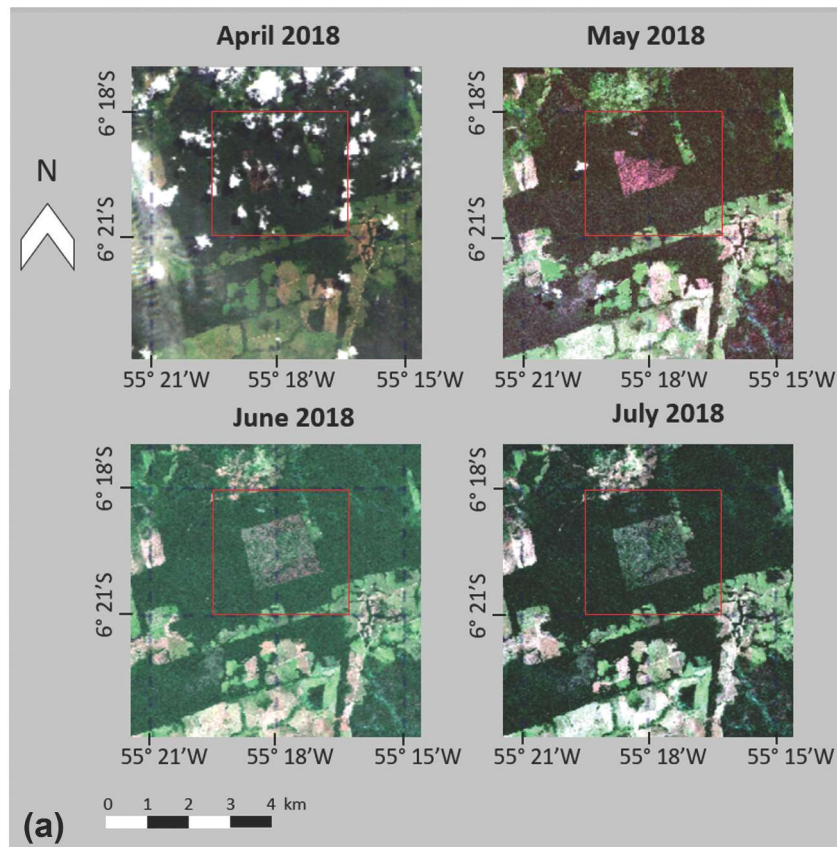
Figure 15. First example of an area with deforestation (highlighted in red), shown by the Sentinel-2 RGB color composites acquired in April, May, June, and July 2018 (a). MaBiomas ground truth (b), classification output with MapBiomas ground truth (c), PRODES ground truth (d), and classification output with PRODES ground truth (e). FP = False positives (number of forested areas classified as deforested), TN = True negatives (number of forested areas classified as forested), FN = False negatives (number of deforested areas classified as forested), and TP =True positives (number of deforested areas classified as deforested).

than the data set of 2019 and 7% lower for the 2018 images, which were obtained automatically by the algorithm.

The MLP does not require high computer processing capability compared with other NN algorithms, such as the CNNs (Bouguettaya et al., 2019). The algorithm
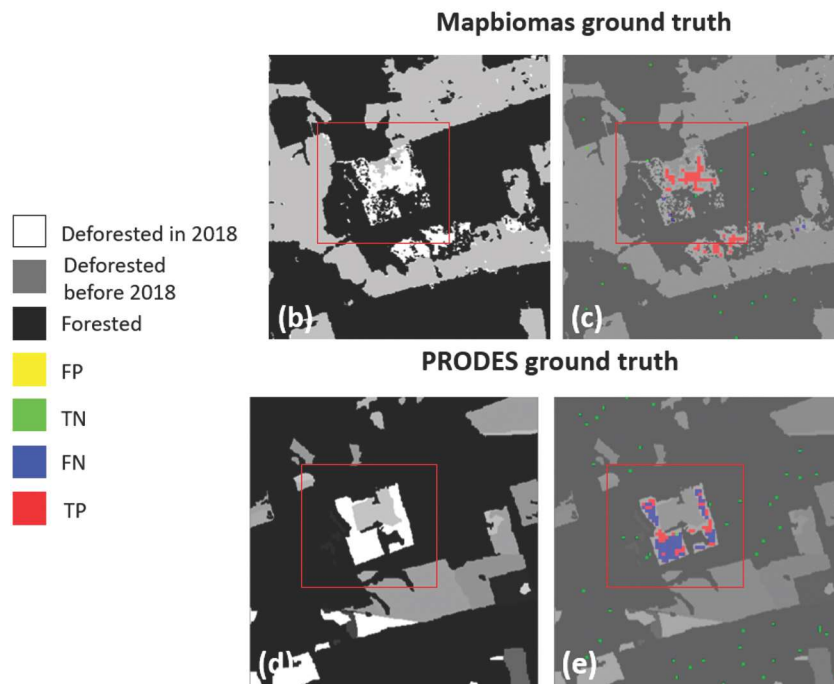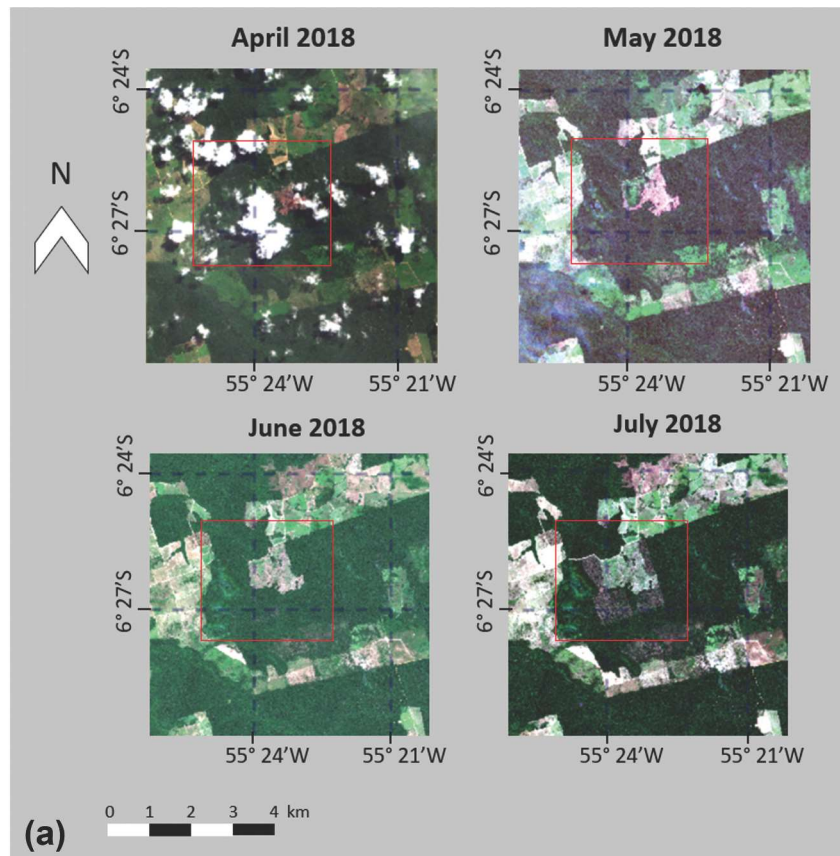
Figure 16. Second example of an area with deforestation (highlighted in red), shown by the Sentinel-2 RGB color composites acquired in April, May, June, and July 2018 (a). MapBiomas ground truth (b), classification output with MapBiomas ground truth (c), PRODES ground truth (d), and classification output with PRODES ground truth (e). FP = False positives (number of forested areas classified as deforested), TN = True negatives (number of forested areas classified as forested), FN = False negatives (number of deforested areas classified as forested), and TP =True positives (number of deforested areas classified as deforested).

used in this work was performed on a personal computer with the following configuration: NVIDIA™ GeForce™ GTX 1650 Max Q GPU with 4GB RAM. Once the network is trained, the time required to make predictions is quite short. During the test phase with the data from 2018, the time necessary to open the images and complete the whole processing was around 1 minute (Table 10).
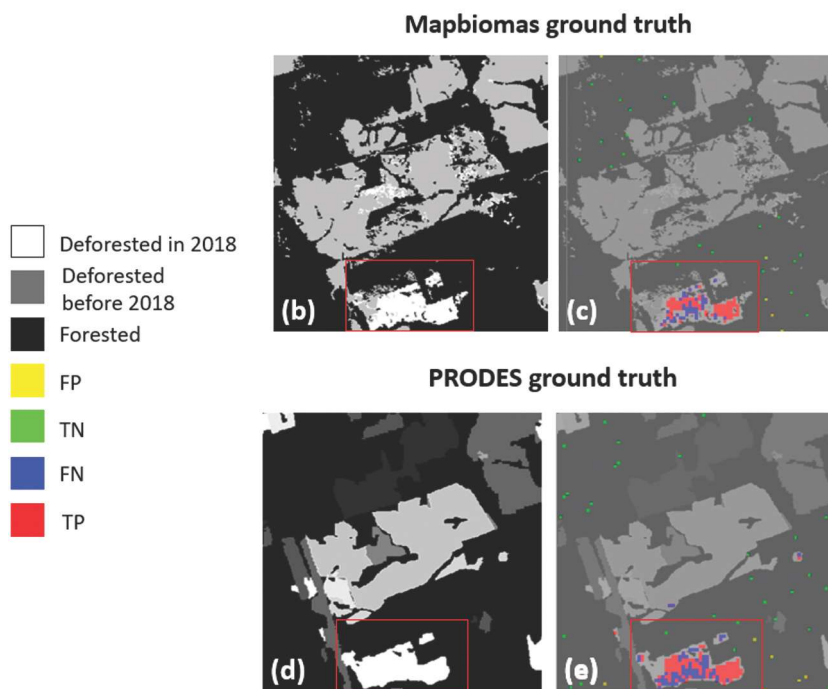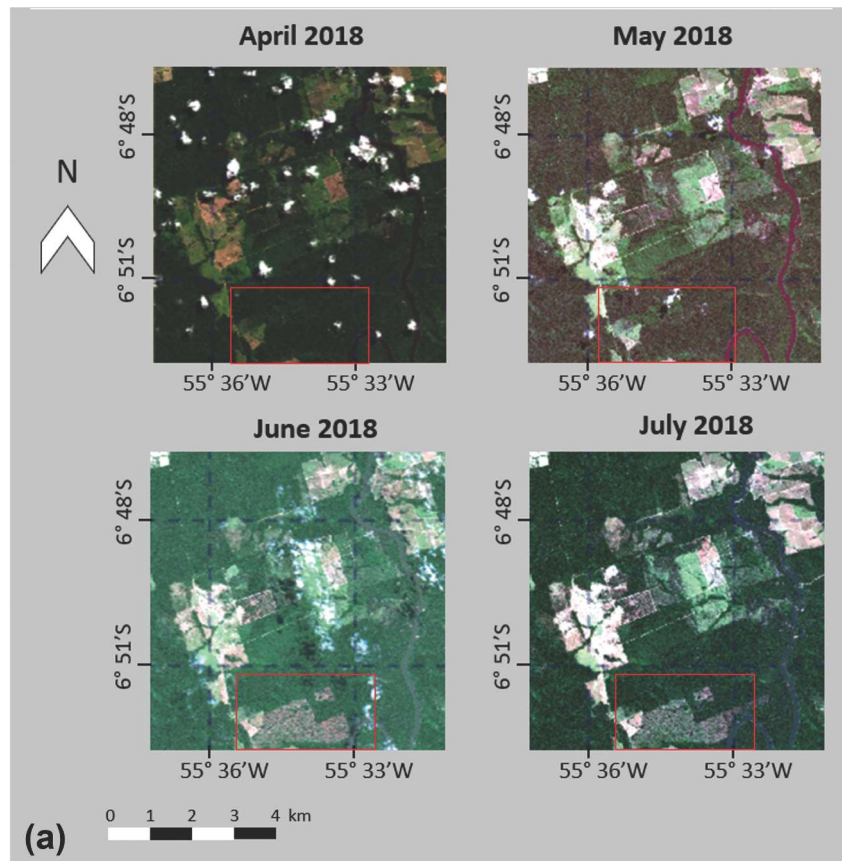
Figure 17. Third example of an area with deforestation (highlighted in red), shown by the Sentinel-2 RGB color composite acquired on April, May, June, and July 2018 (a). MapBiomas ground truth (b), classification output with MapBiomas ground truth (c), PRODES ground truth (d), and classification output with PRODES ground truth (e). FP = False positives (number of forested areas classified as deforested), TN = True negatives (number of forested areas classified as forested), FN = False negatives (number of deforested areas classified as forested), and TP =True positives (number of deforested areas classified as deforested).

Further research should involve strategies to detect deforested areas smaller than 2 ha and use the algorithm as an alert system essential for defor-estations related to illegal mining activities in the Brazilian Amazon. In addition, the algorithm could be refined to detect recently deforested areas (slashed areas) and to disregard areas under vege-tation regrowth. In this latter case, vegetation
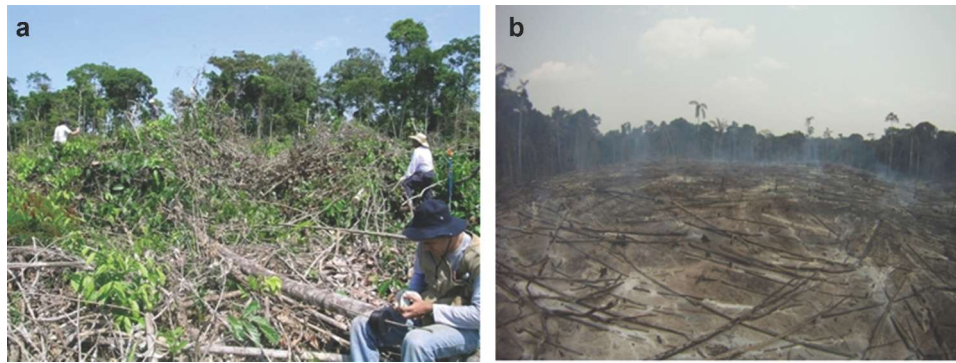
Figure 18. Illustration of a Brazilian Amazon characteristic slashed area (a; Soares Neto et al., 2009) and torched biomass after a fire (b; Christian et al., 2007) found in the Brazilian Amazon.

Table 10. Processing time required during the test phase (2018 data set).

Case study	Processing time (seconds)
1	46.3
2	55.0
3	44.0
4	65.2

indices proposed in literature such as the Normalized Difference Vegetation Index (NDVI), Enhanced Vegetation Index (EVI), or Normalized Difference Water Index (NDWI) can be used to identify the plant growth status and correlate it with forest regrowth (Silva et al., 2019). The method proposed in this study could also be integrated with textural analysis, which exploits correlation among neighbouring pixels, such as those based on the computation of the Gray-Level Co-Occurrence Matrix (GLCM; Del Frate et al., 2008) or geostatistical measures of spatial variability, as suggested by Zawadzki et al. (2005).

Conclusions

In this work, we investigate deforestation in the Amazon rainforest using Sentinel-1 data, and three statistical parameters related to the backscatter coefficient were analysed (mean, standard deviation, and MMD (maximum-minimum difference)). It was observed a backscatter decrease in the average signal of C-band SAR images, approximately 2 dB for VV polarization and 2.3 dB for VH polarization, immediately after deforestation. The decrease is evident for approximately 3–4 months after the deforestation.

The MLP (Multi-Layer Perceptron) was used to detect near real-time forest disturbances larger than 2 hectares. The algorithm analysed SAR images from 2019 for training and 2018 to identify deforest areas automatically. A set of data from 2019 were used to test the performance of the NN (Neural networks) algorithm. Considering the mean, standard deviation, and MMD of the backscatter coefficient as input parameters, the NN was able to classify forested and deforested areas

with accuracy and F1 score of 99% for the 2019 data set. For the 2018 data set, the results showed accuracy and F1 score of 89% with MapBiomas ground truth and accuracy and F1 score of 81% and 79%, respectively, with the PRODES ground truth.

The proposed method may be suitable for monitoring forest events in the Amazon at low cost and short processing times and for assisting Brazilian environmental law enforcement agencies in combating illegal deforestation.

Disclosure statement

No potential conflict of interest was reported by the author(s).

Funding

Data availability statement

These data were derived from the following resources available in the public domain: [Copernicus at https://scihub.copernicus.eu/]; [MapBiomas Brasil at https://mapbiomas.org/en]; [Terrabrasilis at http://terrabrasilis.dpi.inpe.br/en/home-page/]

References

ALOS Global Digital Surface Model 'ALOS World 3D - 30m' (AW3D30).' n.d. Jaxa.Jp. https://www.eorc.jaxa.jp/ALOS/en/aw3d30/index.htm. Accessed July 7, 2021

Bem, P., Carvalho Júnior, O., Guimarães, R. F., & Gomes, R. T. (2020). Change detection of deforestation in the Brazilian amazon using Landsat data and convolutional neural networks. *Remote Sensing*, *12*(6), 901. https://doi.org/10.3390/rs12060901

Benediktsson, J. A., Swain, P. H., & Ersoy, O. K. (1990). Neural Network Approaches versus Statistical Methods in Classification of Multisource Remote

Sensing Data. *IEEE Transactions on Geoscience and Remote Sensing*, 28(4), 540–552. https://doi.org/10.1109/TGRS.1990.572944

Bezerra, T. G., Ruschel, A. R., Emmert, F., & Nascimento, R. G. M. (2021). Changes caused by forest logging in structure and floristic diversity of natural regeneration: Relationship between climate variables and forest dynamics in the Eastern Amazon. *Forest Ecology and Management*, 482, 118862. https://doi.org/10.1016/j.foreco.2020.118862

Bouguettaya, A., Kechida, A., & Taberkıt, A. M. (2019). A survey on lightweight CNN-based object detection algorithms for platforms with limited computational resources. *International Journal of Informatics and Applied Mathematics*, 2(2), 28–44. https://dergipark.org.tr/en/pub/ijiam/issue/52418/654318

Bouvet, A., Mermoz, S., Ballère, M., Koleck, T., & Le Toan, T. (2018). Use of the SAR shadowing effect for deforestation detection with sentinel-1 time series. *Remote Sensing*, 10(8), 1250. https://doi.org/10.3390/rs10081250

Christian, T. J., Yokelson, R. J., Carvalho Jr, J. A., Griffith, D. W. T., Alvarado, E. C., Santos, J. C., Soares Neto, T. G., Veras, C. A. G., & Hao, W. M. (2007). the tropical forest and fire emissions experiment: Trace gases emitted by smoldering logs and dung from deforestation and pasture fires in Brazil. *Journal of Geophysical Research*, 112(D18), D18308. https://doi.org/10.1029/2006JD008147

Cochrane, M. A. (2003). Fire science for rainforests. *Nature*, 421(6926), 913–919. https://doi.org/10.1038/nature01437

Davidson, E. A., Araújo, A. C., Artaxo, P., Balch, J. K., Brown, I. F., Bustamante, M. M. C., Coe, M. T., DeFries, R. S., Keller, M., Longo, M., Munger, J. W., Schroeder, W., Soares-Filho, B. S., Souza, C. M., & Wofsy, S. C. (2012). The Amazon Basin in Transition. *Nature*, 481(7381), 321–328. https://doi.org/10.1038/nature10717

Davis, K. F., Koo, H. I., Dell'Angelo, J., D'Odorico, P., Estes, L., Kehoe, L. J., Kharratzadeh, M., Kuemmerle, T., Machava, D., Pais, A. D. J. R., Ribeiro, N., Rulli, M. C., & Tatlhego, M. (2020). Tropical forest loss enhanced by large-scale land acquisitions. *Nature Geoscience*, 13(7), 482–488. https://doi.org/10.1038/s41561-020-0592-3

Del Frate, F., Pacifici, F., & Solimini, D. (2008). Monitoring urban land cover in Rome, Italy, and its changes by single-polarization multitemporal SAR images. *IEEE Journal of Selected Topics in Applied Earth Observations and Remote Sensing*, 1(2), 87–97. https://doi.org/10.1109/JSTARS.2008.2002221

Del Frate, F., Schiavon, G., Solimini, D., Borgeaud, M., Hoekman, D. H., & Vissers, M. A. M. (2003). Crop classification using multiconfiguration C-Band SAR Data. *IEEE Transactions on Geoscience and Remote Sensing*, 41(7), 1611–1619. https://doi.org/10.1109/TGRS.2003.813530

Del Frate, F., & Solimini, D. (2004). On neural network algorithms for retrieving forest biomass from SAR data. *IEEE Transactions on Geoscience and Remote Sensing*, 42(1), 24–34. https://doi.org/10.1109/TGRS.2003.817220

Del Frate, F., & Wang, L.-F. (2001). Sunflower biomass estimation using a scattering model and a neural network algorithm. *International Journal of Remote Sensing*, 22(7), 1235–1244. https://doi.org/10.1080/01431160151144323

Diniz, C. G., Souza, A. A. A., Santos, D. C., Dias, M. C., Luz, N. C., Moraes, D. R. V., Maia, J. S., Gomes, A. R., Narvaes, I. D. S., Valeriano, D. M., Maurano, L. E. P., &

Adami, M. (2015). DETER-B: The new amazon near real-time deforestation detection system. *IEEE Journal of Selected Topics in Applied Earth Observations and Remote Sensing*, 8(7), 3619–3628. https://doi.org/10.1109/JSTARS.2015.2437075

Doblas, J., Shimabukuro, Y., Sant'Anna, S., Carneiro, A., Aragão, L., & Almeida, C. (2020). Optimizing near real-time detection of deforestation on tropical rainforests using sentinel-1 data. *Remote Sensing*, 12(23), 3922. https://doi.org/10.3390/rs12233922

Farias, M. H. C. S., Beltrão, N. E. S., Cordeiro, Y. E. M., & Santos, C. A. (2018). Impact of rural settlements on the deforestation of the amazon. *Mercator*, 17(5), 1–20. https://doi.org/10.4215/rm2018.e17009

Haykin, S. (2009). *Neural Networks and Learning Machines*. Prentice Hall.

Hoekman, D., Kooij, B., Quiñones, M., Vellekoop, S., Carolita, I., Budhiman, S., Arief, R., & Roswintiarti, O. (2020). Wide-area near-real-time monitoring of tropical forest degradation and deforestation using Sentinel-1. *Remote Sensing*, 12(19), 3263. https://doi.org/10.3390/rs12193263

Joshi, N., Mitchard, E. T. A., Woo, N., Torres, J., Moll-Rocek, J., Ehammer, A., Collins, M., Jepsen, M. R., & Fensholt, R. (2015). Mapping Dynamics of Deforestation and Forest Degradation in Tropical Forests Using Radar Satellite Data. *Environmental Research Letters*, 10(3), 034014. https://doi.org/10.1088/1748-9326/10/3/034014

Kastens, J. H., Brown, J. C., Coutinho, A. C., Bishop, C. R., Esquerdo, J. C. D. M., & Vadrevu, K. P. (2017). Soy moratorium impacts on soybean and deforestation dynamics in Mato Grosso, Brazil. *PloS One*, 12(4), e0176168. https://doi.org/10.1371/journal.pone.0176168

Kellndorfer, J. (2019). Using SAR data for mapping deforestation and forest degradation. In A.I. Flores-Anderson, K.E. Herndon, R.B. Thapa, & E. Cherrington (Eds.), *The Synthetic Aperture Radar (SAR) Handbook: Comprehensive Methodologies for Forest Monitoring and Biomass Estimation* (pp. 65–79). SERVIR Global Science Coordination Office, National Space Science and Technology Center.

Laurin, G. V., Avezzano, R., Bacciu, V., Del Frate, F., Papale, D., & Virelli, M. (2018). COSMO-skymed potential to detect and monitor Mediterranean maquis fires and regrowth: A pilot study in capo Figari, Sardinia, Italy. *IForest: Biogeosciences and Forestry*, 11(3), 389–395. https://doi.org/10.3832/ifor2623-011

Laurin, G. V., Liesenberg, V., Chen, Q., Guerriero, L., Del Frate, F., Bartolini, A., Coomes, D., Wilebore, B., Lindsell, J., & Valentini, R. (2013). Optical and SAR sensor synergies for forest and land cover mapping in a tropical Site in West Africa. *ITC Journal*, 21, 7–16. http://dx.doi.org/10.1016/j.jag.2012.08.002

"Mapbiomas Brasil." n.d. *Mapbiomas.Org*. https://mapbiomas.org/en. Accessed July 7, 2021.

Matricardi, E. A. T., Skole, D. L., Costa, O. B., Pedlowski, M. A., Samek, J. H., & Miguel, E. P. (2020). Long-term forest degradation surpasses deforestation in the Brazilian Amazon. *Science*, 369(6509), 1378–1382. https://doi.org/10.1126/science.abb3021

Nepstad, D., Carvalho, G., Barros, A. C., Alencar, A., Capobianco, J. P., Bishop, J., Moutinho, P., Lefebvre, P., Silva, U. L., Jr., & Prins, E. (2001). Road paving, fire regime feedbacks, and the future of amazon forests. *Forest Ecology and Management*, 154(3), 395–407. https://doi.org/10.1016/S0378-1127(01)00511-4

Nepstad, D. C., Verssimo, A., Alencar, A., Nobre, C., Lima, E., Lefebvre, P., Schlesinger, P., Potter, C., Moutinho, P., Mendoza, E., Cochrane, M., & Brooks, V. (1999). Large-scale impoverishment of Amazonian forests by logging and fire. *Nature*, 398(6727), 505–508. https://doi.org/10.1038/19066

Open Access Hub. n.d. *Copernicus.Eu.* Accessed July 7, 2021. https://scihub.copernicus.eu/

Potin, P., Rosich, B., Miranda, N., Grimont, P., Shurmer, I., O'Connell, A., Krassenburg, M., & Gratadour, J.-B. 2019. "Copernicus Sentinel-1 constellation mission operations status." In *Proceedings of the 2019 IEEE International Geoscience and Remote Sensing Symposium (IGARSS 2019)*, Yokohama, Japan. http://dx.doi.org/10.1109/igarss.2019.8898949

Pratola, C., Del Frate, F., Schiavon, G., & Solimini, D. (2013). Toward fully automatic detection of changes in suburban areas from VHR SAR images by combining multiple neural-network models. *IEEE Transactions on Geoscience and Remote Sensing*, 51(4), 2055–2066. https://doi.org/10.1109/TGRS.2012.2236846

Prechelt, L. (1998). Early stopping - but when? In *Lecture Notes in Computer Science* (pp. 55–69). Springer, Berlin, Heidelberg. http://dx.doi.org/10.1007/3-540-49430-8_3

Ramchoun, H., Amine, M., Idrissi, J., Ghanou, Y., & Ettaouil, M. (2016). Multilayer perceptron: Architecture optimization and training. *International Journal of Interactive Multimedia and Artificial Intelligence*, 4(1), 26–30. https://doi.org/10.9781/ijimai.2016.415

Reiche, J., Hamunyela, E., Verbesselt, J., Hoekman, D., & Herold, M. (2018a). Improving near-real time deforestation monitoring in tropical dry forests by combining dense sentinel-1 time series with Landsat and ALOS-2 PALSAR-2. *Remote Sensing of Environment*, 204, 147–161. https://doi.org/10.1016/j.rse.2017.10.034

Reiche, J., Verbesselt, J., Hoekman, D., & Herold, M. (2015). Fusing Landsat and SAR time series to detect deforestation in the tropics. *Remote Sensing of Environment*, 156, 276–293. https://doi.org/10.1016/j.rse.2014.10.001

Reiche, J., Verhoeven, R., Verbesselt, J., Hamunyela, E., Wielaard, N., & Herold, M. (2018b). Characterizing tropical forest cover loss using dense sentinel-1 data and active fire alerts. *Remote Sensing*, 10(5), 777. https://doi.org/10.3390/rs10050777

Sharma, S., Sharma, S., & Athaiya, A. (2020). Activation functions in neural networks. *International Journal of Engineering Applied Sciences and Technology*, 4(12), 310–316. https://doi.org/10.33564/IJEAST.2020.v04i12.054

Silva, C. A., Santilli, G., Sano, E. E., & Laneve, G. (2021). Fire occurrences and greenhouse gas emissions from deforestation in the Brazilian Amazon. *Remote Sensing*, 13(3), 376. https://doi.org/10.3390/rs13030376

Silva, C. A., Santilli, G., Sano, E. E., & Rodrigues, S. W. P. (2019). Análise qualitativa do desmatamento na Floresta Amazônica a partir de sensores SAR, óptico e termal. *Anuário Do Instituto de Geociências*, 42(4), 18–29. https://doi.org/10.11137/2019_4_18_29

Silva Júnior, C., Aragão, L., Fonseca, M., Almeida, C., Vedovato, L., & Anderson, L. (2018). Deforestation-induced fragmentation increases forest fire occurrence in central Brazilian Amazonia. *Forests*, 9(6), 305. https://doi.org/10.3390/f9060305

SNAP Download. n.d. *Esa.Int.* https://step.esa.int/main/download/snap-download/. Accessed July 7, 2021

Soares Neto, T. G., Carvalho Jr, J. A., Veras, C. A. G., Alvarado, E. C., Gielow, R., Lincoln, E. N., Christian, T. J., Yokelson, R. J., & Santos, J. C. (2009). Biomass Consumption and CO_2, CO and main hydro-carbon gas emissions in an Amazonian forest clearing fire. *Atmospheric Environment*, 43(2), 438–446. https://doi.org/10.1016/j.atmosenv.2008.07.063

Souza, C. M., Jr., Shimbo, J. Z., Rosa, M. R., Parente, L. L., Alencar, A. A., Rudorff, B. F. T., Hasenack, H., Matsumoto, M., G. Ferreira, L., Souza-Filho, P. W. M., de Oliveira, S. W., Rocha, W. F., Fonseca, A. V., Marques, C. B., Diniz, C. G., Costa, D., Monteiro, D., Rosa, E. R., Vélez-Martin, E., . . . Azevedo, T. (2020). Reconstructing three decades of land use and land cover changes in Brazilian biomes with Landsat archive and earth engine. *Remote Sensing*, 12(17), 2735. https://doi.org/10.3390/rs12172735

Stramondo, S., Del Frate, F., Picchiani, M., & Schiavon, G. (2011). Seismic source quantitative parameters retrieval from insar data and neural networks. *IEEE Transactions on Geoscience and Remote Sensing*, 49(1), 96–104. https://doi.org/10.1109/TGRS.2010.2050776

"Terrabrasilis – Geographic Data Platform." n.d. *Inpe.Br.* http://terrabrasilis.dpi.inpe.br/en/home-page/. Accessed July 7, 2021

Torres, R., Snoeij, P., Geudtner, D., Bibby, D., Davidson, M., Attema, E., Potin, P., Rommen, B., Floury, N., Brown, M., Traver, I. N., Deghaye, P., Duesmann, B., Rosich, B., Miranda, N., Bruno, C., L'Abbate, M., Croci, R., Pietropaolo, A., . . . Rostan, F. (2012). GMES Sentinel-1 Mission. *Remote Sensing of Environment*, 120, 9–24. https://doi.org/10.1016/j.rse.2011.05.028

van Marle, M. J. E., Field, R. D., van der Werf, G. R., Wagt, I. A. E., Houghton, R. A., Rizzo, L. V., Artaxo, P., & Tsigaridis, K. (2017). Fire and deforestation dynamics in Amazonia (1973–2014). *Global Biogeochemical Cycles*, 31(1), 24–38. https://doi.org/10.1002/2016GB005445

Yanai, A. M., Graça, P. M. L. A., Escada, M. I. S., Ziccardi, L. G., & Fearnside, P. M. (2020). Deforestation dynamics in Brazil's Amazonian Settlements: Effects of land-tenure concentration. *Journal of Environmental Management*, 268(110555), 110555. https://doi.org/10.1016/j.jenvman.2020.110555

Yanai, A. M., Nogueira, E. M., Graça, P. M. L. A., & Fearnside, P. M. (2017). Deforestation and carbon stock loss in Brazil's Amazonian settlements. *Environmental Management*, 59(3), 393–409. https://doi.org/10.1007/s00267-016-0783-2

Zawadzki, J., Cieszewski, C. J., Zasada, M., & Lowe, R. C. (2005). Applying geostatistics for investigations of forest ecosystems using remote sensing imagery. *Silva Fennica*, 39(4), 599–617. https://doi.org/10.14214/sf.369

Copernicus Sentinel data (2021), processed by ESA. https://scihub.copernicus.eu/

6. Conclusions

The main conclusions from this research are summarized as follow:

1) The X-band SAR technology proved to be useful in identifying deforested areas during the rainy season in the Brazilian Amazon;

2) The C-band Sentinel-1 data were not able to unequivocally map areas of deforestation using single images. In this case, it is recommended to consider time series and Sentinel-1 data to improve the feasibility of deforestation detection;

3) The NDVI and the NDMI were able to differentiate moderate to dense vegetation with high moisture from sparse vegetation with low moisture;

4) The LST from forested and deforested areas was able to differentiate regrowth from dense vegetation;

5) In the municipality of Novo Progresso, we observed a positive correlation (R^2 = 0.72) between fire occurrences and the newly deforested areas following the slash-and burn practices. The same trends were also observed for the Pará State (R^2 = 0.66), suggesting a common practice along with the arch of deforestation;

6) The clear-cutting deforestation process may extend for about two to five years until the remaining logs that were stockpiled had been combusted to completion;

7) The occurrences of fire hotspots in the primary forest are from 5% to 20% of newly deforested areas. This is a strong indication of the primary cause of forest degradation due to slash-and-burn practices;

8) The steady increase in deforestation after the PY2011–2012 is probably linked to the Federal Law n. 12.727/2012 that relaxed the forest conservation;

9) In the PY2018–2019, the CO_2 released to the atmosphere after the deforestation practices in the Pará State and in the Brazilian Amazon accounted for 132.1 Mton and 328.7 Mton, respectively;

10) The net CO_2 emissions from fires in 2019 was 295 Mton in the Brazilian Amazon, which is 16% of the whole emissions from Brazil, that consumes about 50% of the recently slashed biomass;

11) The statistical parameters related to the time series of C-band Sentinel-1 backscatter coefficients was able to detect deforestation in the first 3-4 months of deforestation occurrence;

12) Immediately after deforestation, the mean C-band backscatter signals decreased approximately 2.0 dB for VV polarization and 2.3 dB for VH polarization;

13) The neural network methodology was able to map deforestation areas of about 2 ha or higher automatically;

14) The MLP network was able to identify deforestation within a short time frame with a low computer processing and time demand;

15) The mean backscattering coefficients and their corresponding standard deviation and maximum-minimum differences used as input parameters in the neural network image processing were able to classify forested and deforested areas with accuracy and F1 score of 99%;

16) Automatic detection of deforestation based on SAR images from 2018 reached accuracy and F1 score of 89% with the MapBiomas project ground truth and accuracy and F1 score of 81% and 79%, respectively, with the PRODES ground truth;

17) The proposed methods may be suitable for assisting the Brazilian environmental law enforcement agencies in combating illegal deforestation.

References

Aragão, L. E., Poulter, B., Barlow, J. B., Anderson, L. O., Malhi, Y., Saatchi, S., ... & Gloor, E. (2014). Environmental change and the carbon balance of A mazonian forests. *Biological Reviews*, *89*(4), 913-931.

Anjos, L. J., Pereira, N. G. P., Alves, S. T. M., José, R. D. S. A., & de Souza, L. A. (2021). Forest remnants in private lands are critical to the persistence of endangered birds in an Amazonian hotspot. *Journal for Nature Conservation*, *61*, 125984.

Azevedo-Ramos, C.; Moutinho, P. (2018). No man's land in the Brazilian Amazon: Could undesignated public forests slow Amazon deforestation? *Land Use Policy*, *73*, 125–127.

Barsi, J.; Schott, J.R.; Hook, S.J.; Raqueno, N.G.; Markham, B.L. & Radocinski, R.G. (2014). Landsat-8 Thermal Infrared Sensor (TIRS) vicarious radiometric calibration.

Remote Sensing, 6: 11607-11626

Bezerra, T. G., Ruschel, A. R., Emmert, F., & Nascimento, R. G. M. (2021). Changes caused by forest logging in structure and floristic diversity of natural regeneration: relationship between climate variables and forest dynamics in the eastern Amazon. *Forest Ecology and Management*, *482*, 118862.

Bustamante, M. M., Roitman, I., Aide, T. M., Alencar, A., Anderson, L. O., Aragão, L., ... & Vieira, I. C. (2016). Toward an integrated monitoring framework to assess the effects of tropical forest degradation and recovery on carbon stocks and biodiversity. *Global change biology*, *22*(1), 92-109.

Crowson, M., Hagensieker, R., & Waske, B. (2019). Mapping land cover change in northern Brazil with limited training data. *International Journal of Applied Earth Observation and Geoinformation*, *78*, 202-214.

DeVries, B., Pratihast, A. K., Verbesselt, J., Kooistra, L., & Herold, M. (2016). Characterizing forest change using community-based monitoring data and landsat time series. PloS one, 11(3), e0147121

Fearnside, P. M. (2021). The intrinsic value of Amazon biodiversity. *Biodiversity and Conservation*, *30*(4), 1199-1202.

Knight, E.J. & Kvaran, G. 2014. Landsat-8 Operational Land Imager: design, characterization and performance. Remote Sensing, 6: 10286-10305

Kranz, O., Schoepfer, E., Tegtmeyer, R., & Lang, S. (2018). Earth observation based multi-scale assessment of logging activities in the Democratic Republic of the Congo. ISPRS journal of photogrammetry and remote sensing, 144, 254-267.

Meneses, P. R.; Almeida, T. 2012. Introdução Ao Processamento de Imagem de Sensoriamento Remoto. Brasília: CNPq/UnB, 266 p.

Nepstad, D. C.; Veríssimo, A.; Alencar, A.; Nobre, C.; Lima, E.; Lefebvre, P.; Schlesinger, P.; Potter, C.; Moutinho, P.; Mendoza, E.; et al. (1999). Large-scale impoverishment of Amazonian forests by logging and fire. *Nature, 398*, 505–508.

Nóbrega, C. C., Brando, P. M., Silvério, D. V., Maracahipes, L., & de Marco Jr, P. (2019). Effects of experimental fires on the phylogenetic and functional diversity of woody species in a neotropical forest. *Forest Ecology and Management*, *450*, 117497.

Silveira, J. M., Louzada, J., Barlow, J., Andrade, R., Mestre, L., Solar, R., ... & Cochrane, M. A. (2016). A multi-taxa assessment of biodiversity change after single and recurrent wildfires in a Brazilian Amazon forest. *Biotropica*, *48*(2), 170-180.

Soares-Filho, B. S.; Nepstad, D. C.; Curran, L. M.; Cerqueira, G. C.; Garcia, R. A.;

Ramos, C. A.; Voll, E.; McDonald, A.; Lefebvre, P.; Schlesinger, P. (2006). Modelling conservation in the Amazon basin. *Nature, 440*, 520–523.

Souza, C. M., Jr.; Shimbo, J. Z.; Rosa, M. R.; Parente, L. L.; Alencar, A. A.; Rudorff, B. F. T.; Hasenack, H.; Matsumoto, M.; Ferreira, L. G.; Souza-Filho, P. W. M.; et al. (2020). Reconstructing three decades of land use and land cover changes in Brazilian biomes with Landsat archive and Earth Engine. *Remote Sens.*, *12*, 2735.

"Terrabrasilis – Geographic Data Platform." n.d. Inpe.Br. http://terrabrasilis.dpi.inpe.br/en/home-page/. Accessed July 7, 2021.

Torres, R.; Snoeij, P.; Geudtner, D.; Bibby, D.; Davidson, M.; Attema, E.; Potin, P.; Rommen, B.; Floury, N.; Brown, M.; Traver, I.N.; Deghaye, P.; Duesmann, B.; Rosich, B.; Miranda, N.; Bruno, C.; L'Abbate, M.; Croci, R.; Pietropaolo, A.; Huchler, M. & Rostan, F. 2012. GMES Sentinel-1 mission. *Remote Sensing of Environment*, *120*: 9-24.

Wang, Y., Ziv, G., Adami, M., Mitchard, E., Batterman, S. A., Buermann, W., ... & Galbraith, D. (2019). Mapping tropical disturbed forests using multi-decadal 30 m optical satellite imagery. *Remote sensing of environment, 221*, 474-488.

Woodhouse, I. H. 2015. Introduction to Microwave Remote Sensing. Speckled Press.